Published in final edited form as:

*Nano Futures*. 2022 June ; 6(2): . doi:10.1088/2399-1984/ac5cd1.

# Magnetic nanoparticles and magnetic particle spectroscopy-based bioassays: a 15 year recap

**Kai Wu**[1,*], **Jinming Liu**[1], **Vinit Kumar Chugh**[1], **Shuang Liang**[2], **Renata Saha**[1], **Venkatramana D Krishna**[3], **Maxim C-J Cheeran**[3,*], **Jian-Ping Wang**[1,2,*]

[1]Department of Electrical and Computer Engineering, University of Minnesota, Minneapolis, MN 55455, United States of America

[2]Department of Chemical Engineering and Materials Science, University of Minnesota, Minneapolis, MN 55455, United States of America

[3]Department of Veterinary Population Medicine, University of Minnesota, St Paul, MN 55108, United States of America

## Abstract

Magnetic nanoparticles (MNPs) have unique physical and chemical properties, such as high surface area to volume ratio and size-related magnetism, which are completely different from their bulk materials. Benefiting from the facile synthesis and chemical modification strategies, MNPs have been widely studied for applications in nanomedicine. Herein, we firstly summarized the designs of MNPs from the perspectives of materials and physicochemical properties tailored for biomedical applications. Magnetic particle spectroscopy (MPS), first reported in 2006, has flourished as an independent platform for many biological and biomedical applications. It has been extensively reported as a versatile platform for a variety of bioassays along with the artificially designed MNPs, where the MNPs serve as magnetic nanoprobes to specifically probe target analytes from fluid samples. In this review, the mechanisms and theories of different MPS platforms realizing volumetric- and surface-based bioassays are discussed. Some representative works of MPS platforms for applications such as disease diagnosis, food safety and plant pathology monitoring, drug screening, thrombus maturity assessments are reviewed. At the end of this review, we commented on the rapid growth and booming of MPS-based bioassays in its first 15 years. We also prospected opportunities and challenges that portable MPS devices face in the rapidly growing demand for fast, inexpensive, and easy-to-use biometric techniques.

### Keywords

magnetic nanoparticle; magnetic particle spectroscopy; bioassay; point-of-care; disease diagnosis; food safety

[*]Authors to whom any correspondence should be addressed. wuxx0803@umn.edu, cheeran@umn.edu and jpwang@umn.edu.

Conflict of interest

The authors declare no conflict of interest.

## 1. Introduction

The application of MNPs in biological and biomedical context is a fast-growing area. Where MNPs, with proper surface functionalization, are used as contrast agents in MRI and NMR-based biosensors [1, 2], tracers for MPI and MPSF-based biosensors [3, 4], tags for MR-based biosensors [5, 6], labels for cell sorting and separation [7, 8], heating sources for hyperthermia [9, 10], carriers for drug/gene delivery [11, 12], as well as SERS-active substrates for different biochemical assays [13, 14]. As these technologies become more mature and widely used in clinical theragnostics (therapy and diagnostics), the pursuit of higher-sensitivity bioassay platforms, higher-resolution medical imaging technologies, and lower-dose magnetic therapies has led researchers to rethink the basic designs of MNPs (figure 1). For example, IONs ($Fe_3O_4$ and $\gamma$-$Fe_2O_3$) are frequently used for these applications due to high biocompatibility, stability, low cost, and biodegradability. The quest for high magnetic moment MNPs using other magnetic materials such as pure metals (e.g. Fe, Co, Ni), alloys (e.g. FeCo, alnico, permalloy), and oxides (e.g. $MFe_2O_4$ where M = Fe, Co, Mn, Ni, Zn) [15-17] is growing in view of higher magnetic signal and magnetic force for those aforementioned magnetic theragnostic applications. Pure metal MNPs show favorable magnetic properties, such as high saturation magnetization, but they may be toxic like Co MNPs, or oxidative sensitive like Fe MNPs. Thus, proper treatments are needed to make them more suitable for biomedical applications. In addition, some limitations including cytotoxicity and biocompatibility, potential agglomerates [18, 19], the synthesis method (such as whether it can be prepared in large quantities, the accessibility of raw materials and elements) and cost should be taken into consideration when choosing the right MNPs [20-22]. Furthermore, the design of MNPs specially tailored for biological and biomedical applications has been of less attention compared to its wide applications. Herein, we will review and discuss possible options in designing MNPs regarding different choices of magnetic materials, MNP synthesis and characterization techniques, MNP structural designs (i.e. core@shell, single- and multi-core designs), and the surface functionalization strategies. We aim to provide peers with available options for the design, synthesis, functionalization, and characterization of MNPs, which are specifically tailored for different application purposes and scenarios.

MPI, since its first report in 2005, has been developed into a complementary tomographic technique to MRI. It is a tracer imaging technique that differs from the structural imaging techniques (e.g. x-ray, CT, and MRI) that allows quantitative 3D imaging of MNPs with high spatial and temporal resolution [23]. MPS, firstly reported by Nikitin *et al* [24] and Krause *et al* [25] in 2006, it is a technology derived from MPI and thrives as a new research topic in the field of magnetic bioassays [23-26]. The MPS-based bioassay platform is one of the direct beneficiaries of facile preparation and chemical modification of MNPs and has become a rapidly developing research topic in recent years [27, 28]. For both techniques, MNP acts as a tracer and is the only source of magnetic signal from the biological samples. Both MPI and MPS rely on the nonlinear magnetic responses of MNPs and the fact that MNP's magnetization saturates at a specific magnetic field strength. Upon the application of oscillating magnetic fields (magnetic drive field), MNPs are periodically saturated by the fields and exhibit dynamic magnetic responses that contain not only the drive field frequency

but also a series of harmonic frequencies. These higher harmonics are uniquely generated by MNPs and can be easily separated by means of appropriate filtering. Since subtle changes in MNP design may result in significantly different magnetic responses, by fine-tuning the MNP material, size, shape, structure etc, each kind of MNP has its own unique 'fingerprint' (i.e. MPS spectrum), allowing multiplexed bioassays [29-36]. From its first report in 2006 to date (2021), different MPS platforms developed by several research groups have been categorized either by the drive field format (mon- and dual-frequency) or by the bioassay method (surface- and volumetric-based). The mechanisms and schematic drawings of each scenario are provided. Herein, we will recap the 15 year development history of MPS technique (2006–2021), summarize different branches of MPS-based bioassay methods, analyze the different structures of MNPs tailored to different MPS platforms, and propose the future development trend in miniaturized, portable, rapid, accurate, and easy-to-use bioassay kit. It is worth mentioning that the author published a review article on MPS technology in 2019, mainly focusing on theoretical and mathematical models [27]. Another short review article published by the authors focuses on various MPS-based applications, not only in bioassays, but also in target tracking and recognition, as an adjunct to magnetic imaging and hyperthermia [28]. To the best knowledge of the authors, there are no resources to review the 15 year history of MPS development (2006–2021) and the trends in miniaturized, portable, fast, accurate, and easy-to-use bioassay kit over the next 15 years. This review will fill the gap between our current understanding of MPS technology and the path ahead.

## 2. MNPs: properties, synthesis, functionalization and characterization

In this section we reviewed the different magnetic materials for the synthesis of MNPs including pure metals, alloys, and oxides. Generally, top-down and bottom-up approaches are used to synthesis MNPs. For the top-down approach, a ball milling method is reviewed. For the bottom-up approach, which is commonly used for the synthesis of MNPs, a sputtering-based GPC method, co-precipitation method, and thermal decomposition method are summarized. Both the advantages and disadvantages of each method are discussed in table 2, providing various options to obtain MNPs based on different applications. Several characterization techniques are also reviewed in figure 5. The phase information, morphology, sizes and size distributions, compositions, and magnetic properties can be characterized on MNPs to make sure they fulfill the requirements of a specific application. Different surface functionalization strategies for MNPs are reviewed, categorized by organic and inorganic coating methods. The surface functionalization improves the biocompatibility of MNPs, increases the colloidal stability of MNP suspension, protects the magnetic cores from oxidation and corrosion.

### 2.1. Magnetic materials: from bulk to nanoparticles

**2.1.1. Magnetic materials and properties—**As discussed in the previous section, most magnetic bioassay platforms rely on the magnetic signals from MNPs. Thus, the basic magnetic properties of MNPs are critical when choosing MNPs for a specific application, such as the saturation magnetization, magnetic anisotropy, size and size distribution, whether it is superparamagnetic or not, etc. The saturation magnetization, $M_S$, is defined as the

maximum magnetic moment per unit volume for a magnetic material, which is intrinsic and related to the spin–orbit coupling of a magnetic material. $M_s$ is one of the decisive factors of the magnetic moment per MNP ($m$). The other factor is the magnetic core size or magnetic core volume. MNPs with a higher $M_s$ may provide larger magnetic signals compared with MNPs with a lower $M_s$. Magnetic anisotropy, $K$, indicates a preferred direction on the spin for a system and this direction may not align with an external magnetic field. Magnetic anisotropy induces a hysteresis loop of MNPs with non-zero coercivity and remanence. Thus, magnetic dipolar interactions between MNPs may induce agglomerations, which is not preferred for biomedical applications. However, when the size of MNPs is smaller enough, the thermal energy is large enough to overcome the magnetic anisotropy energy and the MNPs become superparamagnetic (the coercivity and remanence become zero). The criteria for MNPs to be superparamagnetic is $KV/k_BT \leqslant 25$, where $V$ is the magnetic core volume of a MNP, $k_B$ is Boltzmann constant, and $T$ is temperature in Kelvin.

It should be pointed out that $M_s$ can change with temperature and the size of MNPs. Generally, $M_s$ decreases with temperature due to thermal fluctuation. There are several sources of magnetic anisotropy, such as magnetocrystalline anisotropy, shape anisotropy, magnetoelastic anisotropy, and exchange anisotropy. Magnetocrystalline anisotropy is an intrinsic property of MNPs, which depends on the crystal structure of MNPs and decreases with temperature. Shape anisotropy is related to the shape of MNPs. For example, the shape anisotropy of spherical MNPs is isotropic and no shape anisotropy but asymmetric shapes like a rod and a disk may induce large shape anisotropy. The shape anisotropy is proportional with the saturation magnetization of MNPs and also decreases with temperature. In a strained system, however, a magnetoelastic anisotropy appears, depending on the strength of strains. In some core@shell MNPs, if one is ferromagnetic and the other is antiferromagnetic, the exchange interaction between the ferromagnetic material and antiferromagnetic material can induce an exchange anisotropy, which is unidirectional parallel or antiparallel to the magnetization of the ferromagnetic material.

For MNPs in most bioassay applications, superparamagnetism is the prerequisite to avoid agglomerates that may cause false magnetic signals or lead to the blocking of blood vessels (in the case of intravenous administration of MNPs for *in vivo* applications). Furthermore, MNPs with uniform or narrow size distribution can help improve magnetic performance and bioassay repeatability, especially when detecting ultra-low amounts of target analytes. Table 1 summarizes the specific saturation magnetizations, anisotropy values, and critical sizes of superparamagnetism of some popular magnetic materials. Here, a specific saturation magnetization ($\sigma_s$) is defined as the maximum magnetic moment per unit weight, which is more convenient to characterize MNPs. Magnetic materials such as pure metals (Fe, Co, Ni), alloys (FeCo, permalloy, etc), and oxides ($Fe_3O_4$, $\gamma$-$Fe_2O_3$, etc) are most frequently reported to produce MNPs. Among which, iron oxide MNPs, such as magnetite ($Fe_2O_3$) and maghemite ($\gamma$-$Fe_2O_3$), are mostly used in biomedical applications due to their outstanding stability and biocompatibility. However, the $\sigma_s$ of iron oxide MNPs is much lower than other magnetic materials such as Fe, $\gamma'$-$Fe_4N$, FeCo, $Fe_{16}N_2$, etc [37-40]. FeCo has a high $\sigma_s$, which is two to three times higher than iron oxides. Although this material is cytotoxic, the issue can be addressed by introducing a biocompatible shell such as silica. The nonmagnetic shell may reduce the $\sigma_s$ of a MNP depending on the shell thickness. It is reported that FeCo

MNPs can show superparamagnetic behaviors with the size around 100 nm [41], which may compensate the reduction of magnetization if coating a nonmagnetic shell. Fe also shows high $\sigma_s$ but it can be easily oxidized. A proper approach is needed to reduce/avoid the oxidation. FeSi MNPs show good biocompatibility and comparable $\sigma_s$ to iron oxides and its Curie temperature is tunable by controlling the Si content, which has been applied for proper self-regulation of thermal energy [42]. $\gamma'$-$Fe_4N$ is another candidate of high moment MNPs. It is stable and biocompatible. However, $\gamma'$-$Fe_4N$ MNPs usually have large size distribution due to the relatively high temperatures during the synthesis process. $\alpha''$-$Fe_{16}N_2$ is known for its giant $\sigma_s$, which can be higher than that of FeCo alloy, which provides much higher magnetic signals. But $\alpha''$-$Fe_{16}N_2$ MNPs tend to be oxidized in the air and the $D_{sp}$ is much smaller due to it high magnetocrystalline anisotropy. $Fe_{16}CN$ also has high $M_s$ and the $D_{sp}$ is larger than that of $\alpha''$-$Fe_{16}N_2$ because of the relatively lower anisotropy. However, no $Fe_{16}CN$ MNPs have been reported yet.

To obtain high magnetic signals when using iron oxide MNPs, larger sizes are required that may exceed the superparamagnetic critical size to make these MNPs not superparamagnetic anymore with non-zero coercivity and remanence [43, 44]. Typically, MNPs are defined as nanoparticles that are smaller than 1 $\mu$m in diameter. To maintain superparamagnetic properties, the sizes of MNPs are usually limited to tens of nanometers, as listed in table 1. On the other hand, magnetic nanoclusters that composed of multiple individual superparamagnetic MNPs, known as magnetic nanobeads, within the size range of 50–200 nm are also a popular choice for biomedical applications. In this review, the superparamagnetic MNPs and magnetic nanobeads are noted as single- and multi-core MNPs.

#### 2.1.2. From bulk magnetic materials to superparamagnetic nanoparticles—

Magnetic materials may be divided into multiple magnetic domains to minimize the magnetostatic energy. A magnetic domain is a small unit that contains magnetic spins in a uniform direction. Each domain is spontaneously magnetized to the saturation state. The domains are separated by domain walls that are transections of magnetizations from one direction to another. The magnetization direction of each domain may not be aligned without the assistance of a high enough external magnetic field. It also requires energy for creating domain walls. Thus, when the size of magnetic materials decreases, the energy required to create a domain wall equals to or larger than the magnetostatic energy. In this case, no domain wall will be created, and a single domain state is achieved. The critical size of a single domain state depends on the magnetic properties of magnetic materials. The size is proportional to $(A/2K)^{1/2}$, where $A$ is the exchange stiffness of a magnetic material. Generally, the single domain size of MNPs ranges from 10 nm to 100 nm depending on the magnetic properties of a specific magnetic material. Figure 2(A1) shows the schematic drawing of the coercivity versus the size of MNPs, where $D_{crit}$ denotes as the critical size of a single domain state. MNPs with single domain state show high coercivity but the coercivity decreases significantly with the decrease of the size of MNPs and becomes zero when the size reaches the superparamagnetic criteria ($D_{sp}$). The $M$–$H$ curves of superparamagnetic and ferromagnetic materials are schematically drawn in figure 2(A2).

**2.1.3. MNP structure designs—**There are many MNP structure designs reported so far, such as the core@shell structure including single-core and multi-core MNPs, the core@shell@shell (i.e. core@multi-shell), the hollow core@shell, the core@porous-shell, and the hollow shell structures, as shown in figure 2(B). Other structures such as inverse core@shell, Janus structure, dumbbell structure, etc are not included [63-67]. Here the shells can be organic and inorganic materials as discussed in section 2.3. For the MNPs with hollow and porous-shell designs (figures 2(B4)-(B6)), the voids and pores are usually designed for drug/gene/biocatalyst loading purposes [68-73]. These structural designs are usually not considered for designing MNPs for bioassay applications since the voids and mesoporous are non-magnetic or paramagnetic thus, the overall magnetic moment of each MNP is lower than the solid MNP counterpart of same size. Which is not practical for magnetic bioassays where higher magnetic moment per MNP is preferred for higher detection sensitivity. On the other hand, the core@shell and core@multi-shell MNP structures are prevalently used for magnetic bioassays. The ‘core’ is typically magnetic material and ‘shell’ is organic compound and/or inorganic material such as polymers, silica, carbon and gold [74-80]. In addition to the application-oriented functions of shells such as for drug loading and releasing (for drug/gene delivery application) [81-83], for dual-modal imaging and thermal therapy [84-87], for dual-modal T1/T2-weighted MRI [73, 88-90], etc. More practical and prevalent functions of shells are (a) to prevent the magnetic core from oxidation, (b) to facilitate the surface functionalization of chemical compounds, and (c) to improve the colloidal stability and biocompatibility of MNPs [82, 91-93].

Herein, we will focus the application of single- and multi-core MNPs (subordinate to the core@shell and core@multi-shell structures). For the single-core design, the magnetic moment comes from the magnetic core. Besides choosing different MNP materials with high saturation magnetizations, an alternative to achieve high moment single-core MNPs is to use larger magnetic cores. With increasing magnetic core size, these MNPs show ferromagnetic behavior and hysteresis loops (non-zero remanent magnetization, as shown in figure 2(A1)), which, is preferred for some applications such as magnetic hyperthermia [99-103]. However, this remanent magnetization may leads to the agglomeration of MNPs, blocking blood vessels and causing false magnetic signals for imaging and biosensing [104-106]. Thus, MNPs with superparamagnetic behaviors (zero remanent magnetization) are chosen for most biomedical applications. Superparamagnetism appears in very small MNPs when the magnetizations randomly flip due to thermal fluctuations. The core sizes of superparamagnetic nanoparticles are usually below several nanometers to several tens of nanometers depending on the materials [107]. Consequently, the requirement on magnetic core size for superparamagnetism limits the achieving of high magnetic moment MNPs. Thus, multi-core MNPs are designed where a cluster of smaller superparamagnetic nanoparticles are embedded in a polymer matrix [32, 108, 109]. These relatively large, multi-core MNPs show negligible remanent magnetization (compared to single-core MNPs with the same overall size), higher colloidal stability, and low tendency to form agglomerates. Thus, multi-core MNPs is an excellent alternative to single-core MNPs. Nowadays, multi-core MNPs have also been exploited for magnetic separation [110, 111], MPI [32, 112, 113], MRI [114-116], and hyperthermia [117]. While for most biological

and biomedical applications, single- and multi-core MNPs hold equally important roles [118-120].

Nowadays, there are many commercially available MNPs of varying sizes, shapes, structure designs, and materials provided by companies such as Ocean NanoTech, LLC (United States), Nanoprobes, Inc. (United States), NANOGRAFI Co. Inc. (Turkey), Nilaco Corp. (Japan), Hongwu International Group Ltd (China), and micromod Partikeltechnologie GmbH (Germany), etc. Available choices are single- and multi-core MNPs with surface functionalization of proteins such as streptavidin, biotin, chemical compounds such as carboxyl, amine, PEG, azide, dextran, PS, PLA, PEI, inorganic materials such as silica, gold, etc. Materials of MNP cores such as oxides ($Fe_3O_4$, $\gamma$-$Fe_2O_3$, etc), pure metals (Fe, Co, Ni, etc), alloys (FeCo, FeNi, etc), nitrides ($Fe_xN$, $x = 2–4$), etc.

## 2.2. Methods for synthesis of MNPs

Numerous methods have been reported for the synthesize of MNPs. Generally, these methods are categorized into two approaches: top-down and bottom-up approaches (as shown in figure 3(A)). Top-down approaches are used to prepare MNPs by breaking down bulk materials into nano-sized particles, such as ball milling, laser ablation, spark ablation, etc. Bottom-up approaches synthesize MNPs from nucleation and growth of atoms, such as physical methods like GPC, wet-chemical methods like co-precipitation, thermal decomposition, sol-gel method, etc. For the top-down approach, we will take the ball milling method as an example. For the bottom-up method, which is the most commonly used for the synthesis of MNP, the GPC method (physical method), the co-precipitation method (chemical method), and the thermal decomposition method (chemical method) are reviewed.

**2.2.1. Ball milling method—**Ball milling is widely used for preparing nanoparticles by breaking down bulk materials into nano-sized particles. This method is firstly developed in 1970 to prepare nanoparticle powders [121]. A schematic drawing of the ball milling machine and the working mechanism of this method is illustrated in figure 3(B). Grinding media (i.e. balls) and materials to grind (the bulk materials) are sealed in a grinding tank. The mechanism of ball milling method is firstly proposed by Fecht *et al* consisting of three stages [122]. In the 1st stage, share bands are induced in bulk materials with a high dislocation density. In the 2nd stage, nano-sized grains are created in the material due to the dislocation rearrangement to minimize the energy of the system. In the last stage, more high angle grain boundaries are induced in the material and some small grains are peeled off to form particles. The size of particle decreases with time following the equation $d = kt^{-2/3}$, where $d$ is the grain diameter, $k$ is a constant, and $t$ is the grinding time [123]. However, due to the cold welding effect between these small particles, they can be welded together to increase the overall particle size, thus, the particle size cannot be reduced indefinitely with the increasement of grinding time $t$ [124, 125]. A ball milling method also has difficulties to obtain MNPs with desired shapes and sizes.

There are two different kinds of ball milling methods that being used for synthesizing nanoparticles. One is milling without surfactants, called dry milling, and the other is milling with surfactants, called wet milling. A surfactant, such as heptane, oleic acid, etc,

is adsorbed on the new surfaces of particles peeled off from the bulk material during the milling process [126-128]. Then, the fresh surfaces of the new particles are separated by layers of surfactant, which can help decrease the welding effect of small particles to obtain nanoparticles with smaller sizes. Nowadays, different kinds of MNPs have been synthesized by the ball milling method including Fe, Co, FeCo, SmCo, NdFeB, etc [129-133]. The size distribution of nanoparticles synthesized by this method is usually very wide. A narrower size distribution can be obtained by dispersing these nanoparticles in a surfactant/solution and extracting the supernatant after centrifugation but the yield of MNPs is low [128, 134].

**2.2.2. GPC method—**The GPC method is a type of bottom-up approach. It synthesizes nanoparticles through the nucleation and growth of atoms in a high vacuum environment [16]. For this method, the atomic gas is obtained through different energy sources, such as evaporation, sputtering, etc, and then the atomic gas is cooled down and begins the nucleation and growth. A sputtering source is more widely used since more materials are suitable for sputtering. Herein, we will focus on a sputtering-based GPC method. A GPC system with a sputtering source is shown in figure 3(C), which has two chambers connected by a small orifice [40, 138]. A pressure differential is created between these two chambers and the synthesized nanoparticles can be carried by a gas flow through the orifice and deposited on a substrate.

In the schematic drawing, the synthesis of Fe nanoparticles is used as an example. Fe atoms are knocked out of the target, forming atomic gas. A high sputtering pressure of several mTorr is used for this system to provide enough Ar atoms to collide with Fe atoms. The energy of the Fe atom will then be transferred to the Ar atom through collision, and the temperature of the Fe atom will decrease. When the temperature is low enough and the density of the Fe atom gas is high enough, the Fe nanoparticles begin to nucleate and grow. By tuning the sputtering current density and the intensity of magnetic field near the target surface, the plasma region and distribution can be tuned back and forth. Thus, Fe nanoparticles with different phases can be obtained. When the sputtering current $I$ is high and magnetic field intensity $B$ is low, the plasma is long and Fe nanoparticles can gradually cool down to obtain bcc Fe nanoparticles. In contrast, bct Fe nanoparticles are obtained if the plasma is short under the condition of low $I$ and large $B$ [40].

Different kinds of MNPs, such as high magnetic moment Fe and FeCo MNPs, have been synthesized by this GPC method, which have different shapes, sizes, and narrow size distributions [39, 139]. By controlling the plasma distribution different sizes and shapes of nanoparticles can be synthesized such as spherical and cubical nanoparticles [40, 140, 141]. MNPs with a narrow size distribution synthesized by the GPC method can also be achieved by separating the nucleation zone and growth zone of nanoparticles. In addition, core@shell nanoparticles can also be synthesized using the GPC technique. Wang *et al* reported the Co@Au, FeCo@Au MNPs prepared by this GPC system with a single sputtering source using an alloy target [142, 143]. Huttel *et al* reported the synthesize of core@shell and core@shell@shell nanoparticles using multiple sputtering sources [144-146]. The ‘shell’ material can help prevent oxidation of nanoparticles and severs as seeding layers for surface chemical functionalization purposes.

However, the yield of MNPs by this method is relatively low compared with chemical synthesis methods. Several groups have proposed solutions to enhance the yield. Liu *et al* reported a hollow cathode designed for the sputtering-based GPC method to increase the utilization rate of the target material and make the output four times higher than that of the conventional GPC system with a flat target material [147]. Huttel *et al* reported a new magnetron design of a GPC system, which can increase the life of a magnetron target up to 100% [148].

**2.2.3. Co-precipitation method—**Co-precipitation is a convenient method for obtaining IONs (magnetite, maghemite) from aqueous solution, which contains $Fe^{2+}$ and $Fe^{3+}$ salts as shown in figure 3(D) [149, 150]. Magnetite nanoparticles can be synthesized by the co-precipitation of these ions when adding alkaline into the solution at room temperature or at elevated temperature under inert atmosphere. Magnetite nanoparticles can be easily oxidized to maghemite or dissolved in acidic environment. Thus, by properly controlling the synthesis conditions, maghemite nanoparticles can also be synthesized using a co-precipitation method. Maghemite nanoparticles are stable in both alkaline and acidic solutions.

This method has a good control on the shape and phase of nanoparticles. But it is challenging to manipulate the size to obtain nanoparticles with a narrow size distribution [149, 150]. Since the blocking temperature of a particular material depends on the size of the nanoparticles, a wide size distribution of MNPs may cause undesirable magnetic properties, for example, some of the larger MNPs are ferromagnetic while others with smaller sizes are superparamagnetic. Thus, a narrow size distribution of MNPs is critical to obtain uniform magnetic performance.

There are several parameters affecting the size of IONs such as the ratio of $Fe^{2+}/Fe^{3+}$, pH values, types of iron salts used, the reaction temperatures, stirring speed, etc [151]. However, once the parameters for synthesizing IONs are fixed, the nanoparticles are reproduceable. It is critical to control these parameters to produce IONs with a narrow size distribution. In general, nanoparticles with a narrow size distribution can be achieved using the co-precipitation technique by controlling a short nucleation time followed by a slower subsequent growth of these nuclei [152].

Recently, significant efforts have been made to explore the synthesis of magnetite nanoparticles with a narrow size distribution by adding organic additives as stabilizing materials, controlling the pH value, manipulating reaction temperatures, etc. Mello *et al* reported that a stabilizer, PEG, was used to synthesize MNPs with a monodisperse size distribution since PEG can provide a coordination to the surface of nanoparticles for stabilization [153]. Some other organics are also used to obtain a better control on the size of nanoparticles, such as PVA, oleic acid, etc [154-157]. The pH value of the reaction solutions also affects the size distribution. A higher pH value usually induces a smaller particle size and narrower size distribution since high pH will modify the electrostatic surface charge of nanoparticles, which enhances the repulsion among nanoparticles [45]. Dewi *et al* investigated on the effect of precipitation pH on magnetite nanoparticles and reported that the size of MNPs tends to decrease with the precipitation pH, demonstrated

by PSA and HRTEM [158]. The size and size distribution of nanoparticles can also be manipulated by the reaction temperature. The crystalline size of nanoparticles increases with the reaction temperature due to the enhanced number of collisions between particles during the synthesis process [159, 160]. Usually, the reaction is processed at ambient temperature instead of elevated temperatures.

**2.2.4. Thermal decomposition method—**The thermal decomposition method prepares MNPs by the decompositions of organometallic precursors in the presence of surfactants. Surfactants such as oleic acid, lauric acid, oleylamine, etc are adsorbed on the surface of MNPs for controlling the shape and size and preventing aggregations of MNPs. Thermal decomposition method has a much better control on the nucleation and growth process of MNPs, compared with the co-precipitation method, since they happen at different temperature ranges, such as 150 °C–200 °C for the decomposition and 250 °C–300 °C for the growth of MNPs. It results in synthesized MNPs with a very narrow size distribution and better structural properties than MNPs prepared by the co-precipitation method. High temperatures also help enhance the crystallinity of synthesized MNPs [161].

The synthesis of MNPs by a thermal decomposition method can be divided into three stages. First, the solvent containing the organometallic precursors, the surfactants, and the stabilizing agent are heated to reach the nucleation or precursor decomposition temperature. In some cases, reactants at high temperatures are directly introduced to the medium instead of heating from room temperature to the decomposition temperature. Thus, it leads to a rapid nucleation process. Then the solution is heated up to the boiling temperature of the solvent. Small nanocrystals are formed at this stage. Finally, the solution is kept at the high temperature in reflux for the growth of MNPs during a certain time and then cooled down to room temperature to collect the synthesized MNPs. All these stages are carried out in a system under inert atmosphere. Herein, we use the synthesis of iron oxide MNPs as an example. Most commonly used iron organic precursors are iron (III) N-nitrosophenyhydroxylamine ($Fe(cup)_3$), cetylacetonate ($Fe(acac)_5$), and iron pentacarbonyl ($Fe(CO)_5$) [162]. The reaction routes are as follows: $Fe(cup)_3$ or $Fe(acac)_3$ directly decompose into magnetite/maghemite, while $Fe(CO)_5$ goes through an intermediate step of metal formation and then an oxidation of $Fe^0$ into magnetite by addition of a mild oxidant [163, 164].

In principle, MNPs with different sizes, shapes, and crystallinities can be synthesized by properly manipulating experimental parameters such as ratios of reagents (i.e. organometallic precursors, surfactants, and solvents) and temperature ramp, which sometimes might make the reproducibility of MNPs more complicated. Additionally, MNPs prepared by a thermal decomposition method are only dispersible in polar solvent but water, which may limit the applications. Some phase transfer agents such as tetramethylammonium hydroxide, PEG can be used in order to make the MNPs dispersible in water [161, 165].

The pros and cons of each MNP synthesis technique reviewed in section 2.2 are listed and compared in table 2.

## 2.3. MNP surface modification and functionalization strategies

**2.3.1. MNP surface modification—**Due to high surface energy and chemical activity, MNPs are easy to agglomerate in solution, and are easy to oxidize or corrode under environmental or physiological conditions [162]. Meanwhile, since MNPs are made of non-precious metal or metal oxide, they often exhibit toxicity to cells and organs [166], which limits the biological applications of MNPs. Therefore, MNPs are usually coated with protective layers (i.e. shells) to increase their dispersibility, stability and improve their biocompatibility. Based on the coating materials, MNPs surface modification strategy can be classified into two categories, organic coating and inorganic coating. Coating can be achieved during the synthesis of MNPs, known as *in situ* coating. Coating layers can also be added to the synthesized MNPs through post-synthesis adsorption and post-synthesis grafting. In this section, we will review the advantages, coating methods, and potential applications of both kinds of coating compounds.

Organic coating layer can be physically absorbed or covalently bonded to the surfaces of MNPs, and forming different structures as shown in figure 4(A). Both natural compounds like proteins, carbohydrates and synthetic compounds like surfactants and synthetic polymers have been extensively investigated.

MNPs coated with surfactant such as small organic molecules generally have micellular or liposomal structures. They are often used to stabilize MNPs in aqueous condition or oil/hydrocarbon carrier fluids [167]. For example, sodium oleate is one kind of biocompatible surfactant. Sun *et al* prepared sodium oleate coated $Fe_2O_3$ nanoparticles with a size distribution of 8–20 nm [168]. The coated MNPs show high dispersity in aqueous solution with the existence of COO— at the surface. Sahoo *et al* demonstrated that citric acid coated MNPs can be stabilized in aqueous condition by exposing at least one hydrophilic carboxylic acid group to the solvent [169]. Moreover, the terminal carboxylic group also extended bond formation with target molecules like proteins and fluorescent dyes.

Synthetic polymers, such as PEG, PVA, PEI, and alginate, if coated, can bring MNPs with tailored and desired properties [162, 170]. The most popular synthetic polymer for MNPs coating is PEG, which is a hydrophilic polymer that has low toxicity. Several studies have shown that PEG-coated MNPs have improved biocompatibility, high water-solubility, and increased blood circulation time [171-174]. Two prevail methods to coat PEG layers are physico-chemical binding and chemical coupling [174-176].

Compared to synthetic polymers, natural polymers usually have milder formulation processes and have advantages in terms of biocompatibility and biodegradability. Various kinds of natural polymers have been exploited for MNPs coating. For instance, dextran and its derivatives are biocompatible, biodegradable and have a high affinity for iron oxide surface owing to their polar interactions [171]. Dextran-coated iron oxide MNPs have been reported as a versatile platform for *in vivo* molecular diagnostic and therapy [177]. A hydrophilic, biodegradable natural polymer chitosan has also drawn the interests of many researches due to its natural abundance and multiple functional groups in its backbone structure [178, 179]. Other common natural coating compounds include starch and gelatin [180, 181].

As an alternative and addition to organic coating materials, oxides like silica, noble metal like gold or silver, and carbon-based materials, are frequently used inorganic coating compounds. Silica is one of the most used inorganic coating compounds, which can be applied on various kinds of MNPs like nickel, cobalt, iron, iron oxide, etc [182]. It is an ideal coating material because of its biocompatibility, hydrophilicity and reactivity with biological ligands [149, 183]. Also, silica shell can prevent the agglomeration and improve the colloidal stability of the MNPs, since it increases the columbic repulsion with a negatively charged surface and is able to shield the magnetic dipole interactions between neighboring magnetic cores. Silica coating strategies for MNPs has been well documented. For instance, it can be directly coated onto the MNPs via the hydrolysis of a sol-gel precursor like TEOS and subsequent condensation [184]. Yue *et al* reported a method to synthesis silica-coated $Fe_3O_4$ with yolk-shell structure [185]. They used an interface sol-gel coating and surfactant-involved co-assembly method to construct $Fe_3O_4$@$SiO_2$@hollow m$SiO_2$ microspheres, then introduced ultra-small Au nanoparticles via an *in situ* reduction method. The synthetic procedure and resulting structures are shown in figure 4(B). This novel structure is ready to be used as a recyclable nanocatalyst with high-performance. Another common synthesis method for silica coating is the microemulsion/reverse microemulsion process which will not be covered in this review [186, 187].

Similar to silica, gold and some other noble metal coatings are nontoxic and can also improve the stability and biological compatibility of MNPs and are nontoxic. Moreover, gold coated MNPs have increased electrical conductivity and additional optical properties, which adds new possibility to the application of the MNPs [188]. Gold shells can be formed directly or indirectly onto the MNP cores. Chemical reduction and reverse micelle method are two common direct coating methods. For example, Wang *et al* synthesized monodispersed core@shell $Fe_3O_4$@Au nanoparticles through an initial synthesis of $Fe_3O_4$ nanoparticles followed by a reduction of $Au(OOCCH_3)_3$ [189]. Cho *et al* prepared Fe@Au nanoparticles through reverse micelle method and reported their potential application as magnetic resonance agents [190]. Indirect coating involves a ‘glue’ layer between the gold layer and the magnetic core, which is often made of silica, polymer or carbon [67].

Besides of the aforementioned compounds, recent years have seen an increasing research interest on carbon coating since carbon-based materials are much more chemically and thermally stable compare to polymer or silica [149]. Several coating strategies have been developed so far, includes vapor deposition [191], sonochemical process [192], and pyrolysis of iron stearate [193]. In one recent example of carbon coating reported by Song *et al*, graphitic carbon shells were coated on FeCo particles through methane CVD to prevent FeCo against oxidation and chemical reaction [194]. Also, the graphitic coating shell shown broad absorbance to the NIR-II region. With further surface modification, these FeCo@C particles have great potentials in facilitating cancer imaging and hyperthermal treatment.

**2.3.2. MNP surface functionalization—**Apart from protection, the coating layer can also serve as the anchoring location for bioconjugates like antibody or protein, which enables further functionalization of MNPs [162, 166, 167, 195]. Surface functionalization is especially important for MNP-based biomedical applications including diagnostics

and targeted therapy [171]. Antibodies are the most commonly used functional groups conjugated on MNP surfaces due to their high specificity and abundance in species [196]. For example, Rashid *et al* synthesized PMIDA grafted, $SiO_2$ coated $Fe_3O_4$ MNPs, then functionalized these MNPs with anti-CD4 antibodies. They demonstrated that these surface functionalized MNPs can be used to positively select peripheral blood T CD4+ lymphocytes [197]. DNA and/or RNA aptamers can also serve as the conjugating ligands. Bamrungsap *et al* reported a kind of aptamer conjugated MNPs for cancer cell recognition. To obtain such MNPs, iron oxide MNPs were first coated with streptavidin and then conjugated with biotin-labeled DNA aptamers [198]. Other ligands used for MNPs surface functionalization include but not limit to peptides, folate and folic acid, affibodies and lectins [199].

### 2.4. Methods for characterization of MNPs

Prior to biomedical applications, the physicochemical properties of MNPs such as crystal structures, sizes and size distribution, elemental compositions, magnetic hysteresis loops, etc are usually characterized by the standard techniques. In this section, we will review the characterization techniques such as XRD, SEM, TEM, VSM, and DLS.

The crystal structures of magnetic materials can be characterized by XRD patterns. As shown in figure 5(A1), the incoming x-ray beam injects into a sample and the atomic plane in the sample diffracts the x-ray, which is collected as the XRD pattern. Different materials have different crystalline structures and thus, the distance between atomic planes ($d_{hkl}$) corresponds to different XRD patterns. Diffraction peaks of a XRD patten represent crystal planes. Hence, XRD patterns indicate the phases of a magnetic material. A XRD pattern of magnetite nanoparticles is shown in figure 5(A2) for example. The positions of diffraction peaks ($2\theta$ values) indicate the phases by comparing them with standard pdf.

The morphologies of MNPs and their sizes and size distributions can be characterized by TEM and SEM. Here, we take the TEM as an example. TEM is comparable to an OM. The source of a TEM is accelerated electrons comparable to a light source in an OM. Electromagnets are used to control the paths of electrons, which works like a lens in an OM. The wavelength of these accelerated electrons, depending on the acceleration voltage of electrons, is much smaller than that of the light source of an OM. Thus, the resolution of TEM can reach sub-nanometers. One TEM image of MNPs is shown in figure 5(B2) as an example. Based on the TEM image, the sizes and size distribution of these nanoparticles can be obtained as shown in figure 5(B3).

The elemental compositions of MNPs can be characterized by EDS. The working principle of EDS is illustrated in figure 5(C1). High energy electromagnetic radiation (x-ray) ejects the inner-shell electrons from an atom. High energy electrons at the outer shells of the atom can fill in, and release energy as x-ray radiations during this process. Such radiation is unique to each element and can be used to identify compositions of a sample. Figure 5(C2) shows the STEM image of magnetite nanoparticles. Figures 5(C3) and (C4) are elemental mappings of iron (Fe) and oxygen (O) using EDS, respectively.

Magnetic properties such as saturation magnetization, remanence magnetization, magnetic coercivity, etc are characterized by VSM. A schematic drawing of a VSM is shown in

figure 5(D1), which has main components such as electromagnets, pick-up coils, sample rod, vibrator, etc. Uniform magnetic field is generated between these two electromagnets and a magnetic sample fixed by a sample rod is put between these electromagnets. When there is a vibration for the sample, it can generate electrical signals in the pick-up coils, which is proportional to the magnetic moment. Thus, a $M$–$H$ curve (hysteresis loop) can be obtained as shown in figure 5(D2). Several magnetic parameters can be obtained from a hysteresis loop such as the saturation magnetization, remanence, coercivity, etc.

Since for most applications, MNPs are surface-functionalized and dispersed in solution, the hydrodynamic sizes and hydrodynamic size distributions of MNPs can be characterized by DLS. DLS measures the Brownian motion of MNPs in solutions. As shown in figure 5(E1), MNPs are dispersed in a solution and a laser beam is used as the incoming source. The detection angle tells the size of nanoparticles, and the PSD then can be characterized and summarized in the format of figure 5(E2).

MFM is used to scan the surface of a sample with a magnetic probe by measuring the interactions between the probe and the sample. The most common approach to use MFM to characterize MNPs is so-called ‘two-pass technique’, where the sample is scanned twice. First, it scans the sample like a conventional AFM to obtain the topographical image, where the van der Waals force plays the significant role. Second, the cantilever of the MFM is then raised to a certain height away from the surface of the sample and then it starts to collect the magnetic single following the topographical pattern defined by the first step. Thus, the MFM image can reflect the magnetic properties of the sample by collecting the long-range magnetic interactions.

## 3. MPS-based bioassays: mechanisms

In this section, we reviewed the theory of MPS-based bioassay including the nonlinear dynamic magnetic responses of MNPs, the higher harmonics uniquely generated by MNPs, and the Brownian and Néel relaxations of MNPs. Different MPS platforms developed by several research groups have been categorized either by the drive field format (mon- and dual-frequency) or by the bioassay method (surface- and volumetric-based). The mechanisms and schematic drawings of each scenario are provided.

### 3.1. From MPI to MPS

Since its first report in 2005, MPI has been developed into an alternative or complementary tomographic technique to MRI [4, 23, 207-210]. MPI is a tracer imaging technique (different from the structural imaging techniques such as x-ray, CT, and MRI) that allows quantitative 3D imaging of MNPs with high spatial and temporal resolution [3]. As shown in figure 7(A2), MPI relies on an AC ‘modulation field’ and a constant ‘selection field’ (i.e. magnetic gradient field) to selectively suppress magnetic responses of MNP tracers in some regions while only record MNP responses from a FFP. To be specific, the ‘modulation field’ with frequency $f$ and a high amplitude $A$ periodically saturates MNPs. Due to the nonlinear magnetic responses of MNPs (figure 7(A1)), the induced magnetic response, $M(t)$, contains not only the ‘modulation field’ frequency $f$ but also a series of higher odd harmonics (figures 7(A3) and (A4)) such as $3f$, $5f$, $7f$, $9f$ etc. These harmonics are extracted for analysis

by means of appropriate filtering. On top of the ‘modulation field’, a ‘selection field’ is applied to selectively suppress these harmonics for spatial encoding purpose (i.e. to suppress the magnetic responses from MNPs outside the FFP). It is a magnetic gradient field that vanishes in the FFP and increases in magnitude towards the edges as shown in figure 7(A6) [23]. The MNPs outside FFP are fully saturated by this ‘selection field’ and their magnetic responses in the form of harmonics are largely suppressed. As shown in figures 7(A2)-(A4), the ‘selection field’ with amplitude $A_0$ shifts the magnetizations of MNPs to the saturated region and the magnetic responses generate not only the odd but also even harmonics. The amplitudes of these harmonics are negligible compared to the odd harmonics generated by MNPs within the FFP. Thus, MNPs within the FFP are the only signal sources of higher odd harmonics responsible for 3D tomographic imaging.

Figure 6(A1) is an example of MPI platform with the magnetic gradient field (‘selection field’) generated by NdFeB permanent magnets and the FFP is steered in $X$ and $Y$ directions. By steering the FFP through the volume of interest, a 3D tomographic image is generated as shown in figure 6(A2). Figure 6(A3) shows a photograph of MPI system. Nowadays, both prototypes and commercial MPI scanners have been reported for *in vivo* applications in vascular imaging [211-213], oncology [214-217], cell-tracking [211, 218-221], etc. For example, figure 6(A5) shows *in vivo* cancer imaging with systemic MNP tracer administration. The MNP dynamics in the tumor is clearly visualized with MPI where they preferentially accumulate in tumor regions due to the abnormally leaky vasculature. By 96 h, the MNPs are cleared. The dissected organs at the end of MPI imaging are shown in figure 6(A6) where the presence of MNP tracers is observed from liver, spleen, and tumor 2 d post injection. As an emerging imaging technique, MPI opens up a new route to *in vivo*, real-time 3D imaging and it is expected that human scanner will reach to clinical stage in the near future [3, 222].

Meanwhile, different MPS platforms derived from MPI have been reported for bioassay purposes and later become a new research topic in magnetic bioassay area [24, 25, 223]. The first generation MPS platforms were independently reported by the Russia group Nikitin *et al* [24] and the Germany group Krause *et al* [25] in 2006, where a magnetic drive field having two frequency components at $f_H$ and $f_L$ was applied to repeatedly saturate MNPs for bioassay application. This platform is named ‘dual-frequency drive field’ modality in this review. Weaver *et al* [223] from the United States reported a second version of MPS platform for bioassay applications, where the magnetic drive field only has one frequency component $f$. This group also reported the combination of one AC magnetic drive field with a constant field for MPS-based bioassays [224, 225]. Herein, we categorized both methods under ‘mono-frequency drive field’ modality. The schematic drawings of mono- and dual-frequency drive field MPS modalities are shown in figure 6(B). The mono-frequency drive field modality has one set of coils responsible for generating one sinusoidal magnetic drive field (figure 6(B1)). While, on the other hand, the dual-frequency drive field modality has two sets of coils responsible for generating two sinusoidal magnetic drive fields of distinct frequencies and amplitudes (figure 6(B1)). It should be noted that both ‘modulation field’ in MPI and magnetic drive field in MPS are sinusoidal fields responsible to repeatedly saturate MNPs. In order to distinguish these two techniques, we use the term ‘magnetic drive field’ in MPS technique only.

MPS-based bioassays are also categorized by the assay strategies. For the surface-based MPS bioassay, a chemically functionalized reaction surface called ‘substrate’ is introduced to fix MNP tracers for the detection of target analytes from biofluid samples. As shown in figure 6(C), combined with LF test strips or 3D fiber filters, MNP tracers can be fixed to the substrate through a sandwich assay format. After washing out the unbound MNP tracers, these fixed MNPs are ‘counted’ by analyzing MPS spectra. For the volumetric-based MPS bioassay, MNP tracers are binding to target analytes from liquid phase and the binding events cause lower degrees of rotational freedom and weaker magnetic responses, which is monitored by MPS readers, as shown in figure 6(D).

MPS is treated as a 0D MPI technique that instead of recording the spatial distribution of MNP tracers in $X$, $Y$, and $Z$ axis, MPS records the magnetic responses of MNPs from the whole sample space. Thus, the ‘selection field’ is not required in MPS-based bioassays. Up to now, MPS platforms have been reported for the detection of nucleic acid [226], virus [227-231], bacteria, fungi and microbial toxins [232-237], protein biomarkers [226, 238], blood clot [225], etc. In addition, portable MPS devices are also reported for on-site bioassays [229, 230, 239]. A summary of these applications is given in table 4.

### 3.2. Different MPS platforms classified by magnetic drive field

MPS technique inherits MPI’s design of applying a ‘modulation field’ (in MPS, it is called magnetic drive field) to trigger the nonlinear magnetic responses of MNP tracers and utilizes the higher harmonics as information for different application purposes. In MPS, tomographic scanning is not required thus, ’selection field’ is removed. There are currently two types of MPS platform classified by the magnetic drive field. The first one is mono-frequency drive field modality where there is only one sinusoidal magnetic drive field $H(t) = A\sin(2\pi ft)$ as shown in figures 7(B2) and (B5). This drive field with amplitude A large enough to repeatedly saturate MNPs and cause nonlinear magnetic responses (figure 7(B3)). Higher harmonics at frequencies of $3f$(the 3rd harmonic), $5f$(the 5th harmonic), $7f$(the 7th harmonic) are generated, filtered, and collected as information (figure 7(B4)). It is similar to the scenario of MNPs within the FFP in MPI. The other one is dual-frequency drive field modality where there are two sinusoidal magnetic drive fields applied. Namely, one drive field with low frequency and large amplitude, expressed as $H_L(t) = A_L \sin(2\pi f_L t)$, is applied to repeatedly saturate MNPs while, a second drive field with high frequency and low amplitude, expressed as $H_H(t) = A_H \sin(2\pi f_H t)$, is applied to modulate the higher harmonics to high frequency regime, as shown in figures 7(C2) and (C5). Higher harmonics at frequencies of $f_L$, $3f_L$, $5f_L$, …, $f_H \pm 2f_L$ (the 3rd harmonics), $f_H \pm 4f_L$ (the 5th harmonics), $f_H \pm 6f_L$ (the 7th harmonics), and $f_H$, $3f_H$, $5f_H$ are observed due to the dynamic magnetic responses of MNP tracers.

Aside from the magnetic drive fields, from a macro perspective, both MPS platforms record the higher odd harmonics from nonlinear dynamic magnetic responses of MNPs [24, 25, 27]. Qualitatively, the amplitudes (or intensities) of higher harmonics are proportional to the number of MNPs, magnetic moment per particle, drive fields (including field amplitude and frequency) and inversely proportional to the phase lag of magnetic moments to the drive fields [27, 36, 240, 241]. The phase lag is affected by the drive field and effective

relaxation time of MNPs (joint effects of Brownian and Néel relaxation processes) [26, 242-245]. While the Brownian and Néel relaxation processes are affected by one or more of the following factors such as temperature, magnetic anisotropy, liquid medium viscosity, magnetic core size, hydrodynamic size and saturation magnetization of MNPs. From a macro perspective, the relaxation time of magnetic moments of MNPs under AC magnetic drive field leads to the AC magnetic susceptibility [241, 246-250].

As a result, in addition to the biomedical applications, the higher harmonics have been exploited as metrics for measuring the temperature ($T$) and viscosity ($\eta$) of MNP medium [251-256], as well as the saturation magnetization ($M_S$), magnetic core size ($V_C$), and hydrodynamic size ($V_h$) of MNPs [36, 241]. Due to the complexity of theoretical models leading to the MPS spectra, this review will not elaborate on the mathematical models contributing to the reconstruction of higher harmonics. Several literatures are suggested for readers to investigate in depth of these theoretical models: [26, 36, 240, 242-245, 251, 253, 257].

### 3.3. Surface- and volumetric-based MPS bioassays

There are two kinds of MPS bioassay methods that have been frequently reported, the surface- and volumetric-based methods. The intrinsic differences between these two methods are that the surface-based bioassay monitors the amount of MNP tracers captured due to the presence of target analytes while, on the other hand, the volumetric-based bioassay monitors the bound status (or, rotational freedom) of MNP tracers in the presence of target analytes. Both methods will be explained in detail in this section.

The surface-based MPS bioassay method is similar to traditional surface biosensors such as LF tests [259-263], GMR [5, 264-269], and SERS [270-274] biosensors. These types of biosensors use a chemically functionalized reaction surface to capture tracers/markers, in the presence of target analytes, tracers/marked are bound to the reaction surface through specific recognition (such as antibody-antigen, DNA-DNA, etc), then they are sensed by means of fluorescence, optical, and magnetic signals. Surface-based MPS bioassay method works in a similar manner. As shown in figure 8(A1), taking a sandwich bioassay design as an example. The substrate (reaction surface) is a nonmagnetic porous membrane or fiber filter [275], and its surface is functionalized with capture antibodies. As biofluid sample passes through the surface, target analytes are captured through antibody-antigen specific binding. Other molecules and compound that are not bound to the reaction surface are washed out. Followed by another layer of detection antibodies specifically bind to target analytes. After removing the excess antibodies, MNP tracers are added and conjugate to one end of detection antibodies. Free MNPs are washed out and only leaving captured MNPs on the substrate. The number of bound MNPs on the substrate is proportional to the number of target analytes, and the amplitudes (intensities) of higher harmonics are proportional to number of MNPs from sample. Thus, allowing for quantitative MPS bioassays. Figure 8(A2) schematically shows the MPS spectra before and after the capture of MNPs. Since biological tissues and fluids are nonmagnetic or paramagnetic, none or negligible harmonic signals can be observed from the sample. MNP tracers captured and fixed on the substrate will be the only magnetic signal sources responsible for MPS spectra.

On the other hand, the volumetric-based MPS bioassay method is a homogeneous assay that detects target analytes directly from liquid phase without wash steps. Where the MNPs are suspended in liquid and, an extra degree of rotational freedom appears, namely, Brownian relaxation (figure 8(B)). For stational/fixed MNPs, like the scenario in surface-based MPS bioassays, their magnetic moments follow the AC magnetic drive field through the Néel relaxation process as shown in figure 8(B). Néel process is the relaxation of magnetic moment inside a stational MNP to align with external magnetic field and there is no physical movement related to this process. While Brownian process is the rotational movement of the whole MNP along with its magnetic moment in response to external magnetic field. Upon the application of magnetic drive fields, the magnetic moments of MNPs in liquid medium try to align with the fields through the joint effects of Brownian and Néel relaxation processes, to minimize magnetostatics energy, which are countered by the thermal fluctuations ($k_B T$, where $k_B$ is the Boltzmann constant and $T$ is temperature). In addition to thermal energy that randomizes magnetic moments, Brownian process is also affected by the hydrodynamic volume, $V_h$, of MNP as well as the viscosity, $\eta$, of the liquid medium. On the other hand, Néel process is also affected by the effective magnetic anisotropy (including crystal and shape anisotropies), $K_{eff}$, and volume of magnetic core, $V_c$. These two processes jointly govern the ability of magnetic moments to follow the time-changing magnetic field, thus, affecting the dynamic magnetic responses of MNPs to the drive fields. The effective relaxation time is dominated by the faster relaxation process. For single-core MNPs with magnetic core size above 25 nm (some papers and books reported this number to between 12 nm and 20 nm), the Brownian process will dominate dynamic magnetic responses [29, 254, 276-278]. It should be noted that the Langevin model that has been frequently reported to describe magnetic responses of MNPs does not contain the phase information or, the phase lag of MNPs' magnetic moments to the external fields. Thus, Langevin model is insufficient to provide the vectorial responses of MNPs. This phase lag leads to a complex magnetic susceptibility that firstly reported in the Debye model [279]. Although the Debye model is valid for describing the vectorial responses of MNPs under small magnetic fields, it is inaccurate when extended to the nonlinear ranges of the magnetization. Wawrzik *et al* reported a modified Debye model that includes both the nonlinear magnetizations and vectorial responses of MNPs in the context of viscosity/binding-dependent MPS measurements [249].

Since the Brownian process can be altered by the hydrodynamic size of MNPs, researchers have been exploiting the Brownian process-dominated MNPs for volumetric-based MPS bioassays. This method detects target analytes from liquid medium where the harmonics from MNPs are used as metrics for monitoring their hydrodynamic size $V_h$, which reflects the bound states of target analytes to MNPs [27]. As shown in figure 8(C1), when the capture antibodies (aptamers, proteins, DNA etc) are functionalized on MNP surface. Target analytes will bind to MNPs through specific antibody-antigen (DNA–DNA, protein–antibody, etc) Interactions. This specific binding process allows us to quantify target analytes from the aqueous testing sample. The dynamic magnetic responses of MNPs will be impaired by the conjugation of target analytes and the Brownian process is countered. As a result, the observed harmonics become weaker and phase lag between magnetic moments to external field becomes larger [27, 226, 280, 281]. The magnetic signals are then recorded

by the pick-up coils in the format of time-varying voltage signals, converting the quantity of target analytes to spectral components, i.e. harmonics.

### 3.4. Portable MPS devices for on-site bioassays

With the increasing demands for high accuracy, rapid, inexpensive, and easy-access devices for routine daily at-home diagnosis, on-site sample diagnosis in regions with scarce medical resources, disease surveillance and control in pandemics. POC devices that combine the advantages of quantitative and high accuracy nature that are comparable to laboratory-based tests, ease-of-access, and short turn-around times have become a new trend [282-289]. In the past 15 years, several groups have reported the design and application of portable MPS devices targeting for rapid and accurate field tests in nonclinical settings, handheld by layperson with minimal training requirements. In this section, we will review different MPS portable devices regarding the design, bioassay method, and capabilities, which are also summarized in table 3.

Wu *et al* reported a MagiCoil MPS portable device along with a smartphone application user interface as shown in figure 9(A1) [239]. The overall dimensions of this device are 212 mm ($L$) × 84 mm ($W$) × 72 mm ($H$). It is powered by wall plug and can communicate with smartphones (Android and IOS systems), tablets, computers through Bluetooth and USB. It is a volumetric-based MPS platform and the biofluidic samples are contained in a flat bottom, USP type I, glass vial with dimensions of 31 mm × 5 mm and a volume capacity of 0.25 ml, as shown in figure 9(A4). This kind of glass vial is one-time use only and disposable and it can be seamlessly inserted into the sample loading port from the top of the MagiCoil device. The user interface gives users step-by-step instructions on carrying out each test.

Pietschmann *et al* and Rettcher *et al* have reported a FMMD MPS portable device with intuitive touch display, as shown in figures 9(A2) and (A3) [230, 236]. Its overall size is 230 mm ($L$) × 100 mm ($W$) × 70 mm ($H$) and it can be connected to a conventional power outlet or battery, allowing the device to be used in remote locations without a power source. It is a surface-based MPS platform where the immuno-filtration columns are sintered polyethylene filters with a pore diameter of 50 $\mu$m to provide reaction surface for binding of MNPs, as shown in figure 9(A5).

For both portable devices in figure 9(A), biofluidic samples and/or reaction substrates (such as immune-filtration columns in figure 9(A5) and cylindrical 3D fiber filters in figure 9(A6)) can be fitted in a small cylindrical vial and inserted into a MPS signal reader as shown in figure 9(A7). Taking the dual-frequency MPS platform as an example, the MPS signal reader consists of two sets of coils generating low- and high-frequency magnetic drive fields, and one-pair of differentially wounded pick-up coils to sense magnetic responses of MNPs. The pick-up coils are designed in a way that the top half is wounded clock-wise as sensing coils and the bottom half is wounded counter-clock-wise as balancing coils. Both the sensing and balancing coils pick up the time-varying magnetic fields from drive coils and MNPs due to Faraday’s law of induction. In order to remove the effect of magnetic drive fields and only read the dynamic magnetic responses from MNP tracers, the balancing coils are designed in a counter-clock-wise manner to cancel out the EMF caused by magnetic drive fields. On

the other hand, the mono-frequency MPS reader is designed in a similar manner except that there is only one set of coils for drive field.

Figure 9(B) shows another type of MPS portable device, named MPQ (magnetic particle quantification), that combined with lateral flow test strips, reported by Orlov *et al* [233], Guteneva *et al* [290], and Bragina *et al* [291]. It is a surface-based MPS bioassay platform relying on lateral flow test strip as reaction surface. Each lateral flow test strip is 3 mm (*W*) × 40 mm (*L*) in dimension and composed of overlapping sample pad, nitrocellulose, and absorbent membranes assembled on an adhesive plastic backing sheet, as shown in figure 9(B3). Multiplexed bioassay design for simultaneous detection of different target analytes has also been reported based on this platform, such as adding multiple test lines on one lateral flow strip for the simultaneous detection of morphine, fentanyl and methamphetamine as shown in figure 12(A3) [290], or stacking several single-plex test strips in a cartridge as shown in figure 6(C1) [233].

Meanwhile, MPS portable devices mounted with microfluidic channels have also been reported for fully automatic disease screening. As shown in figure 9(C1), Kim *et al* [292] have reported a p-FMMD (planar-frequency mixing magnetic detection) system for the detection of amyloid beta 42 ($A\beta_{42}$), a promising biomarker of Alzheimer's disease, at the minimum concentration of 23.8 pg $ml^{-1}$. The p-FMMD system is composed of two parts: a MPS reader and a motorized translation stage in *X* and *Y*-direction with a motion controller. The MPS reader (including drive coils and pick-up coils) is separated into two equally parts by the microfluidic channel. The motorized translation stage is controlled by a user-programmed interface and the speed of this stage can be varied from 0.1 to 8 mm $s^{-1}$. The spatial traveling range of this stage covers a 25 mm (*X*-direction) × 60 mm (*Y*-direction) rectangular region. It is a surface-based MPS bioassay platform and the large detection area allows multiplexed bioassay with ROI functionalized by different capturing probes. Another microfluidic channel mounted MPS device is reported by Rabehi *et al* [293] where the planar drive coils are contained in two PCB structures each with dimensions of 100 mm (*L*) × 40 mm (*W*) × 1.55 mm (*H*) and separated by a serpentine-like microfluidic channel (12 mm × 12 mm), as shown in figure 9(C2). This is the first report of MPS device with planar drive and pick-up coils in PCB structures. Each coil is composed of four layers, the tracks are 100 nm wide with an inter-distance of 100 nm. Each layer of track has a thickness of 35 nm. The drive coils have a radius of 13 mm (60 turns/layer), and the pick-up coils have a radius of 10 mm (46 turns/layer). Despite the concern of magnetic drive field intensity and uniformity, this is the first step in pushing MPS devices into chip-sized devices.

With the progress of miniaturization of the MPS platform and the trend of fully automated bioassays, it can be foreseen that MPS portable devices can transform the current multi-step, laboratory-based bioassays into non-clinical environments such as homes, schools, offices, and airports, etc. Nowadays, the MPS handheld device combined with lateral flow technology is commercially available at OVVI Diagnostics founded in Belgium. Pure Devices GmbH (Germany) is also providing MPS benchtop systems with laptop software.

## 4. MPS-based bioassays: applications

In this section, we reviewed the MPS-based applications in the areas of disease diagnosis, food safety, plant pathology, drug screening, etc. All these applications reported between year 2006 and 2021 are summarized in table 4. Herein, we highlighted some representative works applying MPS in the detection of fT4, an indicator biomarker of thyroid diseases, SARS-CoV-2, H1N1, SEB, aflatoxin B1, and the multiplexed detection of drugs. Other notable MPS-based applications, such as the monitoring of blood clot formation and mechanical force, detecting cold-chain breaches, temperature, pH, and viscosity, as well as the MNP characterizations indicate that MPS can potentially serve as auxiliary tool in different fields in the future.

### 4.1. MPS for disease diagnosis

In the past 15 years, MPS platforms have been applied for disease diagnosis including Hepatitis B, Influenza, and SARS-CoV-2 viruses [227-229, 231, 275], Alzheimer's disease [292], hormones, cytokines and other signaling molecules from body fluid [294, 298], etc. Different MPS-based bioassays reported in the past 15 years are summarized in table 4. In this section, we only highlight a few of recent publications between year 2018 and 2021.

MPS platform combined with lateral flow assay is frequently used as one representative of surface-based MPS bioassay [232-234, 290, 294, 297, 299, 300]. Herein, we provide readers with one example of this detection scheme for the measurement of fT4 [297]. As shown in figures 10(A1) and (A3), each lateral flow test strip is composed of overlapping nitrocellulose and absorbent membranes assembled on an adhesive plastic backing sheet. This is an example of competitive binding assay. The less amount of fT4 from human blood serum sample, the more such streptavidin-T4-bt-MNP-Ab complexes are formed on the test line. Figure 10(A2) shows the magnetic signal vs fT4 concentration from blood serum. Figure 10(A3) shows the SEM images of MNP tracers at different spots of test strip. This developed surface-based (i.e. LF strip), dual-frequency drive field, MPS (competitive assay)-based method provides a tool for detection of ultra-low concentrations of fT4 in small-volume samples of human serum within the range of 20 fM–10 pM (16 fg $ml^{-1}$–8 pg $ml^{-1}$), which is clinically relevant at hypothyroidism.

Figure 10(B) is an example of volumetric-based MPS assay using surface functionalized MNPs and non-magnetic beads, for the detection of SARS-CoV-2 spike protein [228]. In this work, MNPs are surface functionalized with SARS-CoV-2 spike antibody while, nonmagnetic PS beads are coated with SARS-CoV-2 spike protein to mimic SARS-CoV-2 virus particles, as shown in figures 10(B1) and (B2). The presence of mimic SARS-CoV-2 virus particles will cause MNPs form clusters, and the rotational freedom is constrained (figures 10(B3) and (B4)). As a result, the dynamic magnetic responses in time domain (figure 10(B5)) and harmonics in MPS spectra in frequency domain (figure 10(B6)) become weaker. Thus, quantitative detection of SARS-CoV-2 spike protein (or the mimic SARS-CoV-2 virus particles) can be achieved by analyzing the harmonics. In figures 10(B7) and (B8), the authors used the ratios of the 3rd over the 1st harmonic amplitudes as parameters for quantification of mimic virus particles. The results of MNPs with and without

functionalization of antibodies are compared. A detection limit of 0.084 nM (5.9 fmole) mimic SARS-CoV-2 virus particles is achieved in this work.

Figure 10(C) is another example of volumetric-based MPS assay while only surface functionalized MNPs are used for the detection of H1N1 nucleoprotein [227]. It is based on the fact that MNPs coated with pAbs can bind to different epitopes of H1N1 nucleoprotein molecule (figure 10(C1)). Thus, the target analyte caused MNP clustering will further reduce the rotational freedom of MNPs, and lower weaker harmonic signals are observed (figure 10(C2)). The bright-field TEM Images from figure 10(C3) prove that with higher amount of H1N1 nucleoprotein presenting In the sample, larger MNP clusters are formed. This approach achieved a detection limit of 44 nM (4.4 pmole) for H1N1 nucleoprotein molecule.

### 4.2. MPS for food safety and plant pathology

Furthermore, the applications of MPS In food safety Industry has also been reported, such as detecting microbial toxins [232, 233, 236, 237, 291] and antibiotics [296] from food matrices, and detecting plant viruses including GFLV, PVX, and TMV [230].

Bragina *et al* reported the MPS platform combined with LF strip for detection of SEB from different food matrices [291]. MNPs are surface functionalized with detection antibody to SEB. The test line of FL strip is coated with capture antibody to SEB. In their MPS bioassay step, MNP-Ab conjugates are mixed with SEB from different food matrices including buffer, milk, canned meat and canned mushrooms, then magnetically separated to wash out unbound chemicals, as shown in figure 11(A1). The IMS time is varied from 0 min, 30 min, to 4 h. The front end of LP strip is immersed into the solution of separated MNP-Ab-SEB conjugates. Under capillary forces, the conjugates migrate to the test line of LF strip. If the sample contains the SEB, MNPs are captured on the test line and measured by MPQ reader. The authors varied sample volume and IMS time and different LODs are reached for SEB from different food matrices, as shown in figures 11(A2) and (A3).

On the other hand, Pietschmann *et al* reported a surface-based MPS platform with immuno-filtration columns as reaction substrates for the detection of aflatoxin B1 [236]. As shown in figure 11(B1), the immuno-filtration column made of polyethylene matrix is surface coated with aflatoxin B1 and remaining binding sites are blocked by BSA solution. Then the biotinylated, aflatoxin B1-specific monoclonal antibodies with serially diluted free aflatoxin B1, the sample is flushed through an aflatoxin B1-BSA coated immune-filtration column. Non-saturated antibodies bind to the coated antigen from immuno-filtration column and are retained within the matrix. As shown in figure 11(B3), the higher the mycotoxin content within the sample, the more antibodies are saturated and are flushed through the column. Afterward, streptavidin functionalized MNPs are applied onto the column, bind to retained antibodies and can be detected using the portable FMMD device (see figure 11(B2)). The authors compared the platform sensitivity by using 700 nm and 70 nm MNP tracers. Calibration curves are summarized in figures 11(B3) and (B4). Although 700 nm MNP generates higher magnetic moment (thus, higher MPS signal) than 70 nm MNP of the same materials. Results show that under the same conditions, using 70 nm MNP tracers yield a tenfold increase of MPS signal compared to 700 nm tracers. The possible reason is that when large MNPs are applied, steric hindrance can occur on the substrate surface. So, by

applying a higher ratio of small particles onto the column, a higher amount of small MNPs could bind to antigens coated on the column surface. Similar results have also reported by Achtsnicht *et al* where 75 nm MNPs yields better detection sensitivity than 1010 nm MNPs under the same conditions, for the detection of Cholera toxin subunit B [237].

### 4.3. MPS for drug screening

In addition to the disease diagnosis and food safety monitoring, researchers have also reported the drug screening using MPS platform. For example, Guteneva *et al* reported the multiplexed detection of drugs including morphine, fentanyl, and methamphetamine from human urine samples, using a surface-based MPS platform combined with LF strips, as shown in figure 12(A) [290]. A competitive bioassay strategy is used and, combined with MNP tracers, MPS platform, and LF strips, this technique offers significant advances over the traditional LF test. The MPS-based LF assays are rapid, highly sensitive, and user-friendly, on the level of quantitative laboratory methods. As shown in figure 12(A1), biofluidic sample containing free hapten (free target analytes) mixed with MNP/hapten-BSA conjugates (MNP surface functionalized with target analytes and BSA) migrates along the LF strip under capillary forces. Then free hapten competes with MNP/hapten-BSA complexes for the limited number of antibody binding sites on the test line. Some complexes bind at the test line while the unbounded ones pass through and accumulate in the absorbent membrane. The MNPs bound at the test line is then read by MPS reader coils as shown in figure 12(A3). With this design, the authors proposed multiplexed detection of morphine, fentanyl, and methamphetamine from human urine samples, where MNPs functionalized with morphine, fentanyl, methamphetamine and BSA are added to 75 $\mu$l of human urine samples containing known concentrations of morphine and methamphetamine and zero concentration of fentanyl. The obtained solution is incubated for 10 min at room temperature and applied onto the LF test strip. After migration of the sample along the membrane, the test strip is inserted into three MPS reader coils. Thus, the MPS signals from three test lines can be simultaneously readout as shown in figure 12(A2). Although the multiplexed bioassay has 2.3–3-fold deterioration of LODs compared with the monoplexed bioassay. These drawbacks can be eliminated by multiplex spatial separated layout proposed in [233].

MPS has also been reported in the application of mechanical force monitoring [301], where the superparamagnetic microballoons of around 40 $\mu$m with hollow cores are used as sensor particle for mechanical stress as shown in figure 12(C1). These microballoons are patchy silica-IONs obtained by a partial coverage of IONs with condensed TEOS. Their balloon-like structures can be observed by LSM and SEM as shown in figures 12((C1): (b1), (c1), (b2) and (c2)). These magnetic microballoons are susceptible to mechanical forces and are continuously fragmented under static or dynamic force as shown in figure 12((C1): (c2)). The deformation and subsequent fragmentation (depending on the intensity of mechanical forces) results in a modification of their magnetic properties and thus, the MPS spectra. By use of MPS, these structural changes are readily detected and enable the quantification of the applied mechanical forces in ball mills. As shown in figure 12(C2), the MPS spectra are collected from magnetic microballoons after the application of static compression force. The steepening of the signal curve drop with increasing mechanical energy is evident, especially if one considers the logarithmic scale of the *y*-axe. This design enables the quantification of

acting mechanical forces on an arbitrary sample. As MPS is highly sensitive, the magnetic microballoons do not necessarily have to be separated from the processed material for measurements, which may enable a future inline monitoring.

### 4.4. Other MPS-based applications

Other applications of MPS platforms in clinical theragnostic are worth a mention, such as blood clot formation monitoring [224, 225], mechanical force monitoring [301], detection of cold-chain breaches [302], the temperature, pH, and viscosity measurements [254, 257, 303], the MNP characterization [36, 241], the *in situ* MNP biodegradation monitoring [304], etc. For example, Khurshid *et al* proposed to use MPS platform for a noninvasive evaluation of thrombus maturity, providing the promise of much earlier and more accurate diagnosis of diseases ranging from stroke to myocardial infarction to deep vein thrombosis, as shown in figure 12(B) [224, 225]. In their work, MNPs are functionalized with ATP15 and ATP29 aptamers that can bind to two distinct epitopes on thrombin. The event of MNPs binding to thrombus from blood clot causes reduced rotational freedom (Brownian relaxation), reduced relaxation time, as well as weaker harmonics, as shown in figure 12(B2) [26, 224]. Figure 12(B1) shows clear SEM images of MNP clusters bound on the cell surface.

The real-time MNP binding events are monitored by MPS spectra as shown in figure 12(B3) where the harmonic ratios are recorded under different drive field frequencies, following the addition of a blood clot to MNP solution. The first MPS reading is taken from MNPs before adding the blood clot, plotted in blue colored curve. The harmonic ratios drop over time as more and more MNPs bound on the clot. The arrow in figure 12(B3) marks harmonic ratios drop over the course of sequential measurements in a time window of 30 min. As the MNPs are bound to blood clot, the 2nd and the 4th harmonics both drop due to reduced rotational freedom, however, the harmonic ratio also drops since the 4th harmonic drops faster than the 2nd harmonic. Note that in this work, the authors applied a small DC magnetic field along with a sinusoidal magnetic drive field, thus, only the even harmonics are observed. They used the ratio of the 4th harmonic over the 2nd harmonic as a metric for their rotational freedom that reflects the bound state of the MNPs.

## 5. Challenges and opportunities

Many biomedical applications require various MNPs with varying magnetic properties and structures, which provides a good opportunity for the synthesis of MNPs by different methods such as ball milling, GPC, co-precipitation, thermal decomposition, etc. MNPs are synthesized with a narrow size distribution, mono dispersion, well-controlled shapes and phases, and so on to meet the requirements of related applications. However, a specific synthesis method of MNPs not only has its advantages to fulfill the demand of MNPs used for biomedical applications but also has some disadvantages that need to pay attention to. For example, ball milling method can synthesize large amount of MNPs but these MNPs may have large size distribution and some contamination from the grinding balls and containers. Although the GPC method can prepare MNPs with a narrow size distribution, well-controlled phases and shapes, the yield of MNPs is very low. The co-precipitation is a simple way to synthesize MNPs with a good yield, but it is challenging to precisely control

the stoichiometry and sizes of MNPs. The thermal decomposition method can synthesize MNPs with a narrow size distribution and good structural properties, but some toxic organic solvents are bonded with MNPs, and relatively high temperatures are required. Therefore, a proper synthesis method of MNP is needed to be considered based on different biomedical applications.

Although coating strategies has been well developed over the past few decades, the synthesis of the coating layers is still sometimes challenging. For instance, due to the distinct structural difference between Au and $Fe_3O_4$ MNPs, a full coverage of Au shell on $Fe_3O_3$ is often achieved at the expense of forming byproducts like separate Au nanoparticles [307]. Frequently used organic coating approaches usually involves complex conjugation chemistry and prior functionalization, thus are impractical to produce a large amount of MNPs [308, 309]. Therefore, improvements on synthesis process of the coating layers are yet to be achieved. While coating brings additional properties and applications to MNPs, it may cause some adverse effects on the magnetic properties of those nanoparticles. For example, coating layers can change the shape and size of the MNPs, such changes may affect the coercivity and anisotropy of MNPs [17]. Also, since magnetic saturation is proportional to the weight of the materials, the existence of non-magnetic coating materials reduces the overall magnetization of the MNPs. Throat *et al* has compared the magnetic behaviors of bare and dextran coated LSMO MNPs [310]. They observed that the magnetization at 20 kOe for bare LSMO MNPs is about 20% higher than those coated with dextran. Villanueva *et al* also reported that silica-coated manganese oxide nanoparticles shown an obvious drop in saturation magnetization and the Curie temperature than naked ones [311]. Therefore, how to get improved biological properties while maintaining desired magnetic response can be another challenge and optimization direction for future research.

After 15 years of rapid development (2006–2021), MPS platforms have been transformed into POC devices such as the MagiCoil, FMMD, MPQ, and p-FMMD devices independently reported by different groups (listed in table 3). The additions of microfluidic channels and planar coils push this MPS-based bioassay into a more automatic, user-friendly, easy-to-use, on-site and bed-side healthcare solution. Realizing ‘press one button and get the result within a few minutes’. Figure 13 summarizes the 15 year roadmap of MPS technology along with MPS-based applications since 2006. With the ongoing coronavirus disease 2019 (COVID-19) pandemic, MPS technology starts to shine as a possible solution for faster, more accurate, and inexpensive SARS-CoV-2 detection. Several groups have reported the MPS for SARS-CoV-2 specific antibody and antigen detection [228, 229, 295].

The novel combination of MPS with LF strips or filters opens a new door to multiplexed bioassays, allows the use of multi-core superparamagnetic MNPs with high magnetic moment per particle, enables the quantitative detection of target analytes by ‘counting’ the MNPs captured. This surface-based MPS bioassay method relies on the functionalization of reaction surface (i.e. LF strips and filters), and the removal of unbound compounds such as MNPs and proteins. Thus, the multiple wash steps introduced makes the bioassay complicated and not appliable to layperson for on-site bioassays. Although the current trend of adding microfluidic channels to MPS devices that can simplify the steps and allows for

fully automatic assays [292, 293]. At current stage, the surface-based MPS assay method is still one step away from on-site assays that can be handled by layperson.

The volumetric-based MPS bioassay method relies on the Brownian relaxations of MNPs. By functionalizing probing complexes (i.e. DNA, antibody) to MNP surfaces, these MNPs serve as nano-probes to specifically bind to targe analytes (i.e. DNA, antigen) from liquid phase. This volumetric-based MPS assay method directly measures the collective dynamic magnetic signals from the sample thus, allows for one-step, wash-free bioassay. It allows for on-site test handled by layperson with minimum training requirements. However, the sensitivity of this assay method is impaired by the amount of unbound MNP probes in the sample. Since the MNPs bound to target analytes show a different (or weaker) MPS spectra while the spectra from unbound MNPs are unchanged. As a result, the collective MPS spectra from whole MNP sample is a combination of bound MNPs and free MNPs. For scenarios of detecting very low abundancy of target analytes, the vast majority of MNPs are unbound. Thus, the MPS spectra difference caused by a small amount of bound MNPs will be negligible. There are two strategies to solve this issue of detecting low abundancy analytes: (a) use clustering-based assay where more than one MNPs can bind to one targe analytes [226, 227, 239]; (b) use lower amount of MNPs for volumetric-based bioassays [312].

For both surface- and volumetric-based MPS bioassay methods, in order to achieve the fully automatic, one-step, wash-free bioassays at users' end. An all-on-one chip that combines a filtration system along with a microfluidic channel for reagents mixing (i.e. surface functionalized MNPs specifically bind to target analytes) is suggested. The on-chip filtration system can be achieved by introducing a microfabricated micropillar array [313]. This filtration step is of great importance for testing raw/unprocessed biological samples such as whole blood, saliva, etc, where the large cells, viscous mucus, debris may interfere with the signal. Furthermore, the microfabricated micropillar array is fully compatible with the on-chip microfluidic channels. On the other hand, the microfluidic channel can be designed into serpentine shapes to enhance mixing and cut down the biding time (as well as assay time). Thus, allowing faster filtration and reagent mixing all-on-one chip. Another common challenge faced by both surface- and volumetric-based MPS bioassays is the stability issue for continuous measurements. It is caused by heat dissipation from high current-carrying solenoid coils. This heat dissipation causes the temperature of the coil and biological sample to increase, resulting in increased thermal noise and changes in the MPS harmonic spectrum (the magnetic properties of MNPs are temperature dependent). Mitigation strategies for this issue have not been widely discussed in published literature, a possible workaround is discussed by Wu *et al* [295]. In their work, they reported a test strategy that includes a 3 min cooldown between measurements. Although this manual waiting strategy is suitable for lab-based test systems, it is not suitable for the operation of POC devices, so a more robust approach is needed to address thermal-related MPS stability issues.

## Acknowledgments

This study was financially supported by the Institute of Engineering in Medicine, the Robert F Hartmann Endowed Chair professorship, the University of Minnesota Medical School, and the University of Minnesota Physicians and Fairview Health Services through COVID-19 Rapid Response Grant. This study was also financially supported

by the US Department of Agriculture—National Institute of Food and Agriculture (NIFA) under Award Number 2020-67021-31956. Research reported in this publication was supported by the National Institute Of Dental and Craniofacial Research of the National Institutes of Health under Award Number R42DE030832. The content is solely the responsibility of the authors and does not necessarily represent the official views of the National Institutes of Health.

## Data availability statement

No new data were created or analyzed in this study.

## Abbreviations

| | |
|---|---|
| **3D** | Three-dimensiona |
| $\eta$ | Viscosity |
| $\sigma$ | Specific magnetization |
| $\sigma_s$ | Specific saturation magnetization |
| $A$ | Exchange stiffness |
| **Ab** | Antibody |
| $A\beta_{42}$ | Amyloid beta 42 |
| **ATP** | Aptamer |
| **bcc** | Body-centered cubic |
| **bct** | Body-centered tetragona |
| **BSA** | Bovine serum albumin |
| **CRP** | c-reactive protein |
| **CVD** | Chemical vapor deposition |
| $D_{crit}$ | Critical size of a single domain state |
| **DLS** | Dynamic light scattering |
| $D_{sp}$ | Critical size of superparamagnetism |
| **EDS** | Energy dispersive spectroscopy |
| **FFP** | Field-free point |
| **fT4** | Free thyroxine |
| **GFLV** | Grapevine fanleaf virus |
| **GMR** | Giant magnetoresistive |
| **GPC** | Gas-phase condensation |
| **HBsAg** | Hepatitis B surface antigen |

| | |
|---|---|
| **HRTEM** | High-resolution transmission electron microscopy |
| **IMS** | Immunomagnetic separation |
| **IONs** | Iron oxide nanoparticles |
| ***K*** | Magnetic anisotropy |
| $k_B$ | Boltzmann constant |
| $K_{eff}$ | Effective anisotropy |
| **LF** | Lateral flow |
| **LOD** | Limit of detection |
| **LSM** | Laser scanning microscopy |
| **mGZM-B** | Mouse Granzyme B |
| ***M–H* curve** | Hysteresis loop |
| **mIFN-$\gamma$** | Mouse interferon-gamma |
| **mIL-6** | Mouse interleukin-6 |
| **MNP** | Magnetic nanoparticle |
| **MPI** | Magnetic particle imaging |
| **MPQ** | Magnetic particle quantification |
| **MPS** | Magnetic particle spectroscopy |
| **MR** | Magnetoresistive |
| **MRI** | Magnetic resonance imaging |
| $M_s$ | Saturation magnetization |
| **mVEGF** | Mouse vascular endothelial growth factor |
| **NIR-II** | Second near infrared red |
| **NMR** | Nuclear magnetic resonance |
| **OM** | Optical microscopy |
| **pAb** | Polyclonal antibody |
| **PCB** | Printed circuit board |
| **Pdf** | Powder diffraction files |
| **PEG** | Polyethylene glycol |
| **PEI** | Polyethylenimine |

| | |
|---|---|
| **p-FMMD** | planar-frequency mixing magnetic detection |
| **PLA** | Polylactic acid |
| **PMIDA** | N-(phosphonomethyl) iminodiacetic acid |
| **POC** | Point-of-care |
| **PS** | Polystyrene |
| **PSA** | Particle size analyzer |
| **PSA** | Prostate specific antigen |
| **PVA** | Polyvinyl alcohol |
| **PVX** | Potato virus X |
| **rCGRP** | Rat calcitonin gene related peptide |
| **rIL-6** | Rat interleukin-6 |
| **ROI** | Regions of interest |
| **SARS-CoV-2** | Severe acute respiratory syndrome coronavirus 2 |
| **SEA** | Staphylococcal enterotoxin A |
| **SEB** | Staphylococcal enterotoxin B |
| **SEM** | Scanning electron microscope |
| **SERS** | Surface-enhanced Raman spectroscopy |
| **STEM** | Scanning transmission electron microscopy |
| ***T*** | Temperature |
| **T4** | Thyroxine |
| **T4-bt** | biotinylated T4 |
| **TEM** | Transmission electron microscope |
| **TEOS** | Tetraethoxysilane |
| **TEOS** | Tetraethyl orthosilicate |
| **TMV** | Tobacco mosaic virus |
| **TSST** | Toxic shock syndrome toxin |
| $V_c$ | Magnetic core size |
| $V_h$ | Hydrodynamic size |
| **VSM** | Vibrating sample magnetometer |

| | |
|---|---|
| **XRD** | X-ray diffraction |

## References


[1]. Moser E, Laistler E, Schmitt F and Kontaxis G 2017 Ultra-high field NMR and MRI—the role of magnet technology to increase sensitivity and specificity Front. Phys 5 33

[2]. Grebenkov DS 2018 Diffusion MRI/NMR at high gradients: challenges and perspectives Microporous Mesoporous Mater. 269 79–82

[3]. Wu LC, Zhang Y, Steinberg G, Qu H, Huang S, Cheng M, Bliss T, Du F, Rao J and Song G 2019 A review of magnetic particle imaging and perspectives on neuroimaging Am. J. Neuroradiol 40 206–12 [PubMed: 30655254]

[4]. Bulte JW 2019 Superparamagnetic iron oxides as MPI tracers: a primer and review of early applications Adv. Drug Deliv. Rev 138 293–301 [PubMed: 30552918]

[5]. Su D, Wu K, Saha R, Peng C and Wang J-P 2020 Advances in magnetoresistive biosensors Micromachines 11 34

[6]. Giouroudi I and Kokkinis G 2017 Recent advances in magnetic microfluidic biosensors Nanomaterials 7 171

[7]. Saei A, Asfia S, Kouchakzadeh H and Rahmandoust M 2020 Antibody-modified magnetic nanoparticles as specific high-efficient cell-separation agents J. Biomed. Mater. Res. B 108 2633–42

[8]. Nithya R, Thirunavukkarasu A, Sathya AB and Sivashankar R 2021 Magnetic materials and magnetic separation of dyes from aqueous solutions: a review Environ. Chem. Lett 19 1275–94

[9]. Chang D, Lim M, Goos JA, Qiao R, Ng YY, Mansfeld FM, Jackson M, Davis TP and Kavallaris M 2018 Biologically targeted magnetic hyperthermia: potential and limitations Front. Pharmacol 9 831 [PubMed: 30116191]

[10]. Spirou SV, Basini M, Lascialfari A, Sangregorio C and Innocenti C 2018 Magnetic hyperthermia and radiation therapy: radiobiological principles and current practice Nanomaterials 8 401

[11]. Moros M, Idiago-López J, Asín L, Moreno-Antolín E, Beola L, Grazú V, Fratila RM, Gutiérrez L and de la Fuente JM 2019 Triggering antitumoural drug release and gene expression by magnetic hyperthermia Adv. Drug Deliv. Rev 138 326–43 [PubMed: 30339825]

[12]. Huang R-Y, Lin Y-H, Lin S-Y, Li Y-N, Chiang C-S and Chang C-W 2019 Magnetic ternary nanohybrids for nonviral gene delivery of stem cells and applications on cancer therapy Theranostics 9 2411 [PubMed: 31149052]

[13]. Alula MT, Lemmens P, Bo L, Wulferding D, Yang J and Spende H 2019 Preparation of silver nanoparticles coated ZnO/$Fe_3O_4$ composites using chemical reduction method for sensitive detection of uric acid via surface-enhanced Raman spectroscopy Anal. Chim. Acta 1073 62–71 [PubMed: 31146837]

[14]. Jiao W, Chen C, You W, Zhang J, Liu J and Che R 2019 Yolk–shell Fe/$Fe_4N$@Pd/C magnetic nanocomposite as an efficient recyclable ORR electrocatalyst and SERS substrate Small 15 1805032

[15]. Sun S, Zeng H, Robinson DB, Raoux S, Rice PM, Wang SX and Li G 2004 Monodisperse $MFe_2O_2$ (M = Fe, Co, Mn) nanoparticles J. Am. Chem. Soc 126 273–9 [PubMed: 14709092]

[16]. Liu J, Su D, Wu K and Wang J-P 2020 High-moment magnetic nanoparticles J. Nanopart. Res 22 1–16 [PubMed: 35517915]

[17]. Wu K, Su D, Liu J, Saha R and Wang J-P 2019 Magnetic nanoparticles in nanomedicine: a review of recent advances Nanotechnology 30 502003 [PubMed: 31491782]

[18]. Yeap SP, Lim J, Ooi BS and Ahmad AL 2017 Agglomeration, colloidal stability, and magnetic separation of magnetic nanoparticles: collective influences on environmental engineering applications J. Nanopart. Res 19 1–15

[19]. Stauch C, Späth S, Ballweg T, Luxenhofer R and Mandel K 2017 Nanostructured micro-raspberries from superparamagnetic iron oxide nanoparticles: studying agglomeration degree and redispersibility of nanoparticulate powders via magnetisation measurements J. Colloid Interface Sci 505 605–14 [PubMed: 28651200]

[20]. Ansari SAMK, Ficiarà E, Ruffinatti FA, Stura I, Argenziano M, Abollino O, Cavalli R, Guiot C and d'Agata F 2019 Magnetic iron oxide nanoparticles: synthesis, characterization and functionalization for biomedical applications in the central nervous system Materials 12 465

[21]. Kudr J, Haddad Y, Richtera L, Heger Z, Cernak M, Adam V and Zitka O 2017 Magnetic nanoparticles: from design and synthesis to real world applications Nanomaterials 7 243

[22]. Nikam AV, Prasad BLV and Kulkarni AA 2018 Wet chemical synthesis of metal oxide nanoparticles: a review CrystEngComm 20 5091–107

[23]. Gleich B and Weizenecker J 2005 Tomographic imaging using the nonlinear response of magnetic particles Nature 435 1214–7 [PubMed: 15988521]

[24]. Nikitin PI, Vetoshko PM and Ksenevich TI 2007 New type of biosensor based on magnetic nanoparticle detection J. Magn. Magn. Mater 311 445–9

[25]. Krause H-J, Wolters N, Zhang Y, Offenhäusser A, Miethe P, Meyer MH, Hartmann M and Keusgen M 2007 Magnetic particle detection by frequency mixing for immunoassay applications J. Magn. Magn. Mater 311 436–44

[26]. Weaver JB, Rauwerdink AM, Sullivan CR and Baker I 2008 Frequency distribution of the nanoparticle magnetization in the presence of a static as well as a harmonic magnetic field Med. Phys 35 1988–94 [PubMed: 18561675]

[27]. Wu K, Su D, Saha R, Wong D and Wang J-P 2019 Magnetic particle spectroscopy-based bioassays: methods, applications, advances, and future opportunities J. Phys. Appl. Phys 52 173001

[28]. Wu K, Su D, Saha R, Liu J, Chugh VK and Wang J-P 2020 Magnetic particle spectroscopy: a short review of applications using magnetic nanoparticles ACS Appl. Nano Mater 3 4972–89

[29]. Tu L, Wu K, Klein T and Wang J-P 2014 Magnetic nanoparticles colourization by a mixing-frequency method J. Phys. D: Appl. Phys 47 155001

[30]. Wu K, Batra A, Jain S, Ye C, Liu J, Wang J-P and Simulation A 2015 Study on superparamagnetic nanoparticle based multi-tracer tracking Appl. Phys. Lett 107 173701

[31]. Wu K, Su D, Liu J and Wang J-P 2019 Estimating saturation magnetization of superparamagnetic nanoparticles in liquid phase J. Magn. Magn. Mater 471 394–9

[32]. Kratz H, Taupitz M, de Schellenberger AA, Kosch O, Eberbeck D, Wagner S, Trahms L, Hamm B and Schnorr J 2018 Novel magnetic multicore nanoparticles designed for MPI and other biomedical applications: from synthesis to first *in vivo* studies PLoS One 13 e0190214 [PubMed: 29300729]

[33]. Müssig S, Fidler F, Haddad D, Hiller K-H, Wintzheimer S and Mandel K 2019 Supraparticles with a magnetic fingerprint readable by magnetic particle spectroscopy: an alternative beyond optical tracers Adv. Mater. Technol 4 1900300

[34]. Haegele J, Vaalma S, Panagiotopoulos N, Barkhausen J, Vogt FM, Borgert J and Rahmer J 2016 Multi-color magnetic particle imaging for cardiovascular interventions Phys. Med. Biol 61 N415 [PubMed: 27476675]

[35]. Rauwerdink AM, Giustini AJ and Weaver JB 2010 Simultaneous quantification of multiple magnetic nanoparticles Nanotechnology 21 455101 [PubMed: 20947953]

[36]. Wu K, Schliep K, Zhang X, Liu J, Ma B and Wang J 2017 Characterizing physical properties of superparamagnetic nanoparticles in liquid phase using Brownian relaxation Small 13 1604135

[37]. Liu J, Guo G, Zhang F, Wu Y, Ma B and Wang J-P 2019 Synthesis of A″-$Fe_{16}N_2$ ribbons with a porous structure Nanoscale Adv.1 1337–42 [PubMed: 36132589]

[38]. Liu J, Guo G, Zhang X, Zhang F, Ma B and Wang J-P 2020 Synthesis of α″-$Fe_{16}N_2$ foils with an ultralow temperature coefficient of coercivity for rare-earth-free magnets Acta Mater. 184 143–50

[39]. Liu J, Wu K and Wang J-P 2016 Magnetic properties of cubic FeCo nanoparticles with anisotropic long chain structure AIP Adv.6 056126

[40]. Liu J, Schliep K, He S-H, Ma B, Jing Y, Flannigan DJ and Wang J-P 2018 Iron nanoparticles with tunable tetragonal structure and magnetic properties Phys. Rev. Mater 2 054415

[41]. Liu J, Wu K, He S, Bai J, Xu Y-H and Wang J-P 2021 Large superparamagnetic FeCo nanocubes for magnetic theranostics ACS Appl. Nano Mater 4 9382–90

[42]. Jing Y, Liu J, Ji W-H, Wang W, He S-H, Jiang X-Z, Wiedmann T, Wang C and Wang J-P 2015 Biocompatible Fe–Si nanoparticles with adjustable self-regulation of temperature for medical applications ACS Appl. Mater. Interfaces 7 12649–54 [PubMed: 25996162]

[43]. Zhang L, Gu FX, Chan JM, Wang AZ, Langer RS and Farokhzad OC 2008 Nanoparticles in medicine: therapeutic applications and developments Clin. Pharmacol. Ther 83 761–9 [PubMed: 17957183]

[44]. Srinivasan B, Li Y, Jing Y, Xu Y, Yao X, Xing C and Wang J 2009 A detection system based on giant magnetoresistive sensors and high-moment magnetic nanoparticles demonstrates zeptomole sensitivity: potential for personalized medicine Angew. Chem., Int. Ed 48 2764–7

[45]. Colombo M, Carregal-Romero S, Casula MF, Gutierrez L, Morales MP, Boehm IB, Heverhagen JT, Prosperi D and Parak WJ 2012 Biological applications of magnetic nanoparticles Chem. Soc. Rev 41 4306–34 [PubMed: 22481569]

[46]. Zhang Y, Xu J, Li Q, Cao D and Li S 2019 The effect of the particle size and magnetic moment of the $Fe_3O_4$ superparamagnetic beads on the sensitivity of biodetection AIP Adv. 9 015215

[47]. Li Q, Kartikowati CW, Horie S, Ogi T, Iwaki T and Okuyama K 2017 Correlation between particle size/domain structure and magnetic properties of highly crystalline $Fe_3O_4$ nanoparticles Sci. Rep 7 1–7 [PubMed: 28127051]

[48]. Wu K, Liu J, Saha R, Ma B, Su D, Peng C, Sun J and Wang J-P 2020 Irregularly shaped iron nitride nanoparticles as a potential candidate for biomedical applications: from synthesis to characterization ACS Omega 5 11756–67 [PubMed: 32478267]

[49]. Robertson JD, Rizzello L, Avila-Olias M, Gaitzsch J, Contini C, Magoń MS, Renshaw SA and Battaglia G 2016 Purification of nanoparticles by size and shape Sci. Rep 6 1–9 [PubMed: 28442746]

[50]. Yang FJ, Yao J, Min JJ, Li JH and Chen XQ 2016 Synthesis of high saturation magnetization FeCo nanoparticles by polyol reduction method Chem. Phys. Lett 648 143–6

[51]. Poudyal N, Chaubey GS, Rong C-B, Cui J and Liu JP 2013 Synthesis of monodisperse FeCo nanoparticles by reductive salt-matrix annealing Nanotechnology 24 345605 [PubMed: 23912629]

[52]. Vas' Ko VA, Rantschler JO and Kief MT 2004 Structure, stress, and magnetic properties of high saturation magnetization films of FeCo IEEE Trans. Magn 40 2335–7

[53]. Cullity BD and Graham CD 2011 Introduction to Magnetic Materials (New York: Wiley)

[54]. Tobise M, Ogawa T and Saito S 2017 Morphology and magnetic properties of $\alpha''$-$Fe_{16}N_2$ nanoparticles synthesized from iron hydroxide and iron oxides J. Magn. Soc. Japan 41 58–62

[55]. Costa-Krämer JL, Borsa DM, García-Martín JM, Martín-González MS, Boerma DO and Briones F 2004 Structure and magnetism of single-phase epitaxial $\Gamma'$–$Fe_4N$ Phys. Rev. B 69 144402

[56]. Takahashi T, Takahashi N and Nakamura T 2004 Preparation of freestanding $Fe_4N$ crystal by vapor-phase epitaxy under atmospheric pressure Mater. Chem. Phys 83 7–9

[57]. Wu X, Zhong W, Jiang H, Tang N, Zou W and Du Y 2004 Magnetic properties and thermal stability of $\Gamma'$-$Fe_4N$ nanoparticles prepared by a combined method of reduction and nitriding J. Magn. Magn. Mater 281 77–81

[58]. Jiang Y, Al Mehedi M, Fu E, Wang Y, Allard LF and Wang J-P 2016 Synthesis of $Fe_{16}N_2$ compound free-standing foils with 20 MGOe magnetic energy product by nitrogen ion-implantation Sci. Rep 6 1–7 [PubMed: 28442746]

[59]. Ogawa T, Ogata Y, Gallage R, Kobayashi N, Hayashi N, Kusano Y, Yamamoto S, Kohara K, Doi M and Takano M 2013 Challenge to the synthesis of $\alpha''$-$Fe_{16}N_2$ compound nanoparticle with high saturation magnetization for rare earth free new permanent magnetic material Appl. Phys. Express 6 073007

[60]. Kim TK and Takahashi M 1972 New magnetic material having ultrahigh magnetic moment Appl. Phys. Lett 20 492–4

[61]. Mehedi M, Jiang Y, Suri PK, Flannigan DJ and Wang J-P 2017 Minnealloy: a new magnetic material with high saturation flux density and low magnetic anisotropy J. Phys. D: Appl. Phys 50 37LT01

[62]. Zhang X and Wang J-P 2019 High saturation magnetization and low magnetic anisotropy Fe-CN martensite thin film Appl. Phys. Lett 114 152401

[63]. Ali N, Zhang B, Zhang H, Zaman W, Li W and Zhang Q 2014 Key synthesis of magnetic janus nanoparticles using a modified facile method Particuology 17 59–65

[64]. Yánez-Sedeño P, Campuzano S and Pingarrón JM 2017 Janus particles for (bio) sensing Appl. Mater. Today 9 276–88

[65]. Campuzano S, Gamella M, Serafín V, Pedrero M, Yáñez-Sedeño P and Pingarrón JM 2019 Magnetic janus particles for static and dynamic (Bio) sensing Magnetochemistry 5 47

[66]. Kolhatkar AG, Jamison AC, Litvinov D, Willson RC and Lee TR 2013 Tuning the magnetic properties of nanoparticles Int. J. Mol. Sci 14 15977–6009 [PubMed: 23912237]

[67]. Zhu N, Ji H, Yu P, Niu J, Farooq MU, Akram MW, Udego IO, Li H and Niu X 2018 Surface modification of magnetic iron oxide nanoparticles Nanomaterials 8 810

[68]. Yue Q, Li J, Luo W, Zhang Y, Elzatahry AA, Wang X, Wang C, Li W, Cheng X and Alghamdi A 2015 An interface coassembly in biliquid phase: toward core-shell magnetic mesoporous silica microspheres with tunable pore size J. Am. Chem. Soc 137 13282–9 [PubMed: 26186087]

[69]. Hong Y, Choi IA and Seo WS 2018 Au nanoparticle@hollow mesoporous carbon with FeCo/graphitic shell nanoparticls as a magnetically recyclable yolk–shell nanocatalyst for catalytic reduction of nitroaromatics Sci. Rep 8 7469 [PubMed: 29748617]

[70]. Luo S-C, Jiang J, Liour SS, Gao S, Ying JY and Yu H 2009 Magnetic PEDOT hollow capsules with single holes Chem. Commun19 2664–6

[71]. Chen W-H, Luo G-F, Lei Q, Cao F-Y, Fan J-X, Qiu W-X, Jia H-Z, Hong S, Fang F and Zeng X 2016 Rational design of multifunctional magnetic mesoporous silica nanoparticle for tumor-targeted magnetic resonance imaging and precise therapy Biomaterials 76 87–101 [PubMed: 26519651]

[72]. Gharibshahian M, Mirzaee O and Nourbakhsh M 2017 Evaluation of superparamagnetic and biocompatible properties of mesoporous silica coated cobalt ferrite nanoparticles synthesized via microwave modified pechini method J. Magn. Magn. Mater 425 48–56

[73]. Niu D, Luo X, Li Y, Liu X, Wang X and Shi J 2013 Manganese-loaded dual-mesoporous silica spheres for efficient T1-and T2-weighted dual mode magnetic resonance imaging ACS Appl. Mater. Interfaces 5 9942–8 [PubMed: 24059807]

[74]. Tang D, Yuan R and Chai Y 2006 Magnetic core–shell $Fe_3O_4$@Ag nanoparticles coated carbon paste interface for studies of carcinoembryonic antigen in clinical immunoassay J. Phys. Chem. B 110 11640–6 [PubMed: 16800458]

[75]. Hou S, Chi Y and Zhao Z 2017 Synthesis of core-shell structured magnetic nanoparticles with a carbide shell IOP Conf. Ser.: Mater. Sci. Eng 182 012026

[76]. Chen D, Deng J, Liang J, Xie J, Hu C and Huang K 2013 A core–shell molecularly imprinted polymer grafted onto a magnetic glassy carbon electrode as a selective sensor for the determination of metronidazole Sens. Actuators B 183 594–600

[77]. Liu R, Guo Y, Odusote G, Qu F and Priestley RD 2013 Core–shell $Fe_3O_4$ polydopamine nanoparticles serve multipurpose as drug carrier, catalyst support and carbon adsorbent ACS Appl. Mater. Interfaces 5 9167–71 [PubMed: 24010676]

[78]. Schärtl W 2010 Current directions in core–shell nanoparticle design Nanoscale 2 829–43 [PubMed: 20644772]

[79]. Arvand M and Hassannezhad M 2015 Square wave voltammetric determination of uric acid and diclofenac on multi-walled carbon nanotubes decorated with magnetic core-shell $Fe_3O_4$@$SiO_2$ nanoparticles as an enhanced sensing interface Ionics 21 3245–56

[80]. Tajyani S and Babaei A 2018 A new sensing platform based on magnetic $Fe_3O_4$@NiO core/shell nanoparticles modified carbon paste electrode for simultaneous voltammetric determination of quercetin and tryptophan J. Electroanal. Chem 808 50–58

[81]. Albinali KE, Zagho MM, Deng Y and Elzatahry AA 2019 A perspective on magnetic core–shell carriers for responsive and targeted drug delivery systems Int. J. Nanomed 14 1707

[82]. Hoang Thi TT, Nguyen Tran D-H, Bach LG, Vu-Quang H, Nguyen DC, Park KD and Nguyen DH 2019 Functional magnetic core-shell system-based iron oxide nanoparticle coated with biocompatible copolymer for anticancer drug delivery Pharmaceutics 11 120

[83]. Peralta ME, Jadhav SA, Magnacca G, Scalarone D, Mártire DO, Parolo ME and Carlos L 2019 Synthesis and *in vitro* testing of thermoresponsive polymer-grafted core-shell magnetic

mesoporous silica nanoparticles for efficient controlled and targeted drug delivery J. Colloid Interface Sci 544 198–205 [PubMed: 30844568]

[84]. Tian Q, Hu J, Zhu Y, Zou R, Chen Z, Yang S, Li R, Su Q, Han Y and Liu X 2013 Sub-10 Nm $Fe_3O_4$@$Cu_{2-x}S$ core–shell nanoparticles for dual-modal imaging and photothermal therapy J. Am. Chem. Soc 135 8571–7 [PubMed: 23687972]

[85]. Wang D, Guo Z, Zhou J, Chen J, Zhao G, Chen R, He M, Liu Z, Wang H and Chen Q 2015 Novel $Mn_3$ $[Co(CN)_6]_2$@$SiO_2$@Ag core–shell nanocube: enhanced two-photon fluorescence and magnetic resonance dual-modal imaging-guided photothermal and chemo-therapy Small 11 5956–67 [PubMed: 26437078]

[86]. Tian Q, Wang Q, Yao KX, Teng B, Zhang J, Yang S and Han Y 2014 Multifunctional polypyrrole@$Fe_3O_4$ nanoparticles for dual-modal imaging and *in vivo* photothermal cancer therapy Small 10 1063–8 [PubMed: 24285365]

[87]. Wang H, Mu Q, Revia R, Wang K, Tian B, Lin G, Lee W, Hong Y-K and Zhang M 2018 Iron oxide-carbon core-shell nanoparticles for dual-modal imaging-guided photothermal therapy J. Control. Release 289 70–78 [PubMed: 30266634]

[88]. Xia A, Gao Y, Zhou J, Li C, Yang T, Wu D, Wu L and Li F 2011 Core–shell $NaYF_4$ : $Yb_3^+$, $Tm_3^+$@$Fe_xO_y$ nanocrystals for dual-modality T2-enhanced magnetic resonance and NIR-to-NIR upconversion luminescent imaging of small-animal lymphatic node Biomaterials 32 7200–8 [PubMed: 21742376]

[89]. Wang K, An L, Tian Q, Lin J and Yang S 2018 Gadolinium-labelled iron/iron oxide core/shell nanoparticles as T1–T2 contrast agent for magnetic resonance imaging RSC Adv. 8 26764–70 [PubMed: 35541075]

[90]. Duan B, Wang D, Wu H, Xu P, Jiang P, Xia G, Liu Z, Wang H, Guo Z and Chen Q 2018 Core–shell structurized $Fe_3O_4$@C@$MnO_2$ nanoparticles as PH responsive T1-T2* dual-modal contrast agents for tumor diagnosis ACS Biomater. Sci. Eng 4 3047–54 [PubMed: 33435024]

[91]. Rodriguez-Arco L, Rodriguez IA, Carriel V, Bonhome-Espinosa AB, Campos F, Kuzhir P, Duran JD and Lopez-Lopez MT 2016 Biocompatible magnetic core–shell nanocomposites for engineered magnetic tissues Nanoscale 8 8138–50 [PubMed: 27029891]

[92]. Habib AH, Ondeck CL, Chaudhary P, Bockstaller MR and McHenry ME 2008 Evaluation of iron-cobalt/ferrite core-shell nanoparticles for cancer thermotherapy J. Appl. Phys 103 07A307

[93]. Abbas M, Torati SR, Lee CS, Rinaldi C and Kim CG 2014 $Fe_3O_4/SiO_2$ core/shell nanocubes: novel coating approach with tunable silica thickness and enhancement in stability and biocompatibility J. Nanomed. Nanotechnol 5 1–8

[94]. Shi W, Du D, Shen B, Cui C, Lu L, Wang L and Zhang J 2016 Synthesis of yolk–shell structured $Fe_3O_4$@Void@CdS nanoparticles: a general and effective structure design for photo-fenton reaction ACS Appl. Mater. Interfaces 8 20831–8 [PubMed: 27466968]

[95]. Guntlin CP, Ochsenbein ST, Wörle M, Erni R, Kravchyk KV and Kovalenko MV 2018 Popcorn-shaped $Fe_xO$ (Wustite) nanoparticles from a single-source precursor: colloidal synthesis and magnetic properties Chem. Mater 30 1249–56 [PubMed: 29606798]

[96]. Yang Y, Huang M, Qian J, Gao D and Liang X 2020 Tunable $Fe_3O_4$ nanorods for enhanced magnetic hyperthermia performance Sci. Rep 10 1–7 [PubMed: 31913322]

[97]. Gutiérrez L, Costo R, Grüttner C, Westphal F, Gehrke N, Heinke D, Fornara A, Pankhurst Q, Johansson C and Veintemillas-Verdaguer S 2015 Synthesis methods to prepare single-and multi-core iron oxide nanoparticles for biomedical applications Dalton Trans. 44 2943–52 [PubMed: 25564784]

[98]. Yin NQ, Wu P, Yang TH and Wang M 2017 Preparation and study of a mesoporous silica-coated $Fe_3O_4$ photothermal nanoprobe RSC Adv. 7 9123–9

[99]. Carrey J, Mehdaoui B and Respaud M 2011 Simple models for dynamic hysteresis loop calculations of magnetic single-domain nanoparticles: application to magnetic hyperthermia optimization J. Appl. Phys 109 083921

[100]. Ruta S, Chantrell R and Hovorka O 2015 Unified model of hyperthermia via hysteresis heating in systems of interacting magnetic nanoparticles Sci. Rep 5 9090 [PubMed: 25766365]

[101]. Mehdaoui B, Carrey J, Stadler M, Cornejo A, Nayral C, Delpech F, Chaudret B and Respaud M 2012 Influence of a transverse static magnetic field on the magnetic hyperthermia properties

and high-frequency hysteresis loops of ferromagnetic FeCo nanoparticles Appl. Phys. Lett 100 052403

[102]. Hergt R, Dutz S and Röder M 2008 Effects of size distribution on hysteresis losses of magnetic nanoparticles for hyperthermia J. Phys.: Condens. Matter 20 385214 [PubMed: 21693832]

[103]. Wu K and Wang J-P 2017 Magnetic hyperthermia performance of magnetite nanoparticle assemblies under different driving fields AIP Adv. 7 056327

[104]. Drašler B, Drobne D, Novak S, Valant J, Boljte S, Otrin L, Rappolt M, Sartori B, Iglič A and Kralj-Iglič V 2014 Effects of magnetic cobalt ferrite nanoparticles on biological and artificial lipid membranes Int. J. Nanomed 9 1559

[105]. Rümenapp C, Gleich B and Haase A 2012 Magnetic nanoparticles in magnetic resonance imaging and diagnostics Pharm. Res 29 1165–79 [PubMed: 22392330]

[106]. Taylor A, Wilson KM, Murray P, Fernig DG and Lévy R 2012 Long-term tracking of cells using inorganic nanoparticles as contrast agents: are we there yet? Chem. Soc. Rev 41 2707–17 [PubMed: 22362426]

[107]. Singamaneni S, Bliznyuk VN, Binek C and Tsymbal EY 2011 Magnetic nanoparticles: recent advances in synthesis, self-assembly and applications J. Mater. Chem 21 16819–45

[108]. Marin-Barba M, Gavilán H, Gutierrez L, Lozano-Velasco E, Rodríguez-Ramiro I, Wheeler GN, Morris CJ, Morales MP and Ruiz A 2018 Unravelling the mechanisms that determine the uptake and metabolism of magnetic single and multicore nanoparticles in a Xenopus Laevis model Nanoscale 10 690–704 [PubMed: 29242877]

[109]. Bender P, Bogart LK, Posth O, Szczerba W, Rogers SE, Castro A, Nilsson L, Zeng LJ, Sugunan A and Sommertune J 2017 Structural and magnetic properties of multi-core nanoparticles analysed using a generalised numerical inversion method Sci. Rep 7 45990 [PubMed: 28397851]

[110]. Jeong A and Lim HB 2018 Magnetophoretic separation ICP-MS immunoassay using Cs-doped multicore magnetic nanoparticles for the determination of salmonella typhimurium Talanta 178 916–21 [PubMed: 29136916]

[111]. Witte K, Müller K, Grüttner C, Westphal F and Johansson C 2017 Particle size-and concentration-dependent separation of magnetic nanoparticles J. Magn. Magn. Mater 427 320–4

[112]. Eberbeck D, Dennis CL, Huls NF, Krycka KL, Gruttner C and Westphal F 2012 Multicore magnetic nanoparticles for magnetic particle imaging IEEE Trans. Magn 49 269–74

[113]. Ota S, Takeda R, Yamada T, Kato I, Nohara S and Takemura Y 2017 Effect of particle size and structure on harmonic intensity of blood-pooling multi-core magnetic nanoparticles for magnetic particle imaging Int. J. Magn. Part. Imaging 3 1703003

[114]. Lartigue L, Hugounenq P, Alloyeau D, Clarke SP, Lévy M, Bacri J-C, Bazzi R, Brougham DF, Wilhelm C and Gazeau F 2012 Cooperative organization in iron oxide multi-core nanoparticles potentiates their efficiency as heating mediators and MRI contrast agents ACS Nano 6 10935–49 [PubMed: 23167525]

[115]. Vargas-Osorio Z, Argibay B, Piñeiro Y, Vázquez-Vázquez C, López-Quintela MA, Alvarez-Perez MA, Sobrino T, Campos F, Castillo J and Rivas J 2016 Multicore magnetic $Fe_3O_4$@C beads with enhanced magnetic response for MRI in brain biomedical applications IEEE Trans. Magn 52 1–4

[116]. Kostevšek N, Šturm S, Serša I, Sepe A, Bloemen M, Verbiest T, Kobe S and Rožman KŽ 2015 “Single-” and “multi-core” FePt nanoparticles: from controlled synthesis via zwitterionic and silica bio-functionalization to MRI applications J. Nanopart. Res17 464

[117]. Blanco-Andujar C, Ortega D, Southern P, Pankhurst QA and Thanh NTK 2015 High performance multi-core iron oxide nanoparticles for magnetic hyperthermia: microwave synthesis, and the role of core-to-core interactions Nanoscale 7 1768–75 [PubMed: 25515238]

[118]. Dutz S, Clement JH, Eberbeck D, Gelbrich T, Hergt R, Müller R, Wotschadlo J and Zeisberger M 2009 Ferrofluids of magnetic multicore nanoparticles for biomedical applications J. Magn. Magn. Mater 321 1501–4

[119]. Green LA, Thuy TT, Mott DM, Maenosono S and Thanh NTK 2014 Multicore magnetic FePt nanoparticles: controlled formation and properties RSC Adv. 4 1039–44

[120]. Dutz S 2016 Are magnetic multicore nanoparticles promising candidates for biomedical applications? IEEE Trans. Magn 52 1–3

[121]. Benjamin JS 1970 Dispersion strengthened superalloys by mechanical alloying Metall. Trans 1 2943–51

[122]. Fecht H, Hellstern E, Fu Z and Johnson W 1990 Nanocrystalline metals prepared by high-energy ball milling Metall. Trans. A 21 2333

[123]. Li S, Wang K, Sun L, Wang Z and Simple A 1992 Model for the refinement of nanocrystalline grain size during ball milling Scr. Metall. Mater 27 437–42

[124]. Kirkpatrick E, Majetich S and McHenry M 1996 Magnetic properties of single domain samarium cobalt nanoparticles IEEE Trans. Magn 32 4502–4

[125]. Jiang Y, Liu J, Suri PK, Kennedy G, Thadhani NN, Flannigan DJ and Wang J 2016 Preparation of an $\alpha''$-$Fe_{16}N_2$ magnet via a ball milling and shock compaction approach Adv. Eng. Mater 18 1009–16

[126]. Fang L, Zhang T, Wang H, Jiang C and Liu J 2018 Effect of ball milling process on coercivity of nanocrystalline $SmCo_5$ magnets J. Magn. Magn. Mater 446 200–5

[127]. Tan Y, Sha L, Qu J, Jiang J, Ren J, Wu C and Xu Z 2021 Oleic acid as grinding aid and surface antioxidant for ultrafine zirconium hydride particle preparation Appl. Surf. Set 535 147688

[128]. Wu K, Liu J, Saha R, Ma B, Su D, Chugh VK and Wang J-P 2021 Stable and monodisperse iron nitride nanoparticle suspension for magnetic diagnosis and treatment: development of synthesis and surface functionalization strategies ACS Appl. Nano Mater 4 4409–18

[129]. Zhang Z and Wen G 2020 Synthesis and characterization of carbon-encapsulated magnetite, martensite and iron nanoparticles by high-energy ball milling method Mater. Charact 167 110502

[130]. Aslibeiki B and Kameli P 2020 Structural and magnetic properties of $Co/Al_2O_3$ cermet synthesized by mechanical ball milling Ceram. Int 46 20116–21

[131]. Albaaji AJ, Castle EG, Reece MJ, Hall JP and Evans SL 2017 Effect of ball-milling time on mechanical and magnetic properties of carbon nanotube reinforced FeCo alloy composites Mater. Des 122 296–306

[132]. Zhang D-T, Zhu R-C, Yue M and Liu W-Q 2020 Microstructure and magnetic properties of $SmCo_5$ sintered magnets Rare Met. 39 1295–9

[133]. An X, Jin K, Abbas N, Fang Q, Wang F, Du J, Xia W, Yan A, Liu JP and Zhang J 2017 High anisotropic NdFeB submicro/nanoflakes prepared by surfactant-assisted ball milling at low temperature J. Magn. Magn. Mater 442 279–87

[134]. Poudyal N, Rong C and Liu JP 2011 Morphological and magnetic characterization of Fe, Co, and FeCo nanoplates and nanoparticles prepared by surfactants-assisted ball milling J. Appl. Phys 109 07B526

[135]. Yin Z, Peng Y, Zhu Z, Yu Z and Li T 2017 Impact load behavior between different charge and lifter in a laboratory-scale mill Materials 10 882

[136]. Thapa B, Diaz-Diestra D, Beltran-Huarac J, Weiner BR and Morell G 2017 Enhanced MRI T2 relaxivity in contrast-probed anchor-free PEGylated iron oxide nanoparticles Nanoscale Res. Lett 12 1–13 [PubMed: 28050875]

[137]. Mahhouti Z, El Moussaoui H, Mahfoud T, Hamedoun M, El Marssi M, Lahmar A, El Kenz A and Benyoussef A 2019 Chemical synthesis and magnetic properties of monodisperse cobalt ferrite nanoparticles J. Mater. Sci. Mater. Electron 30 14913–22

[138]. Liu J, Zhang D, Wu K, Hang X and Wang J-P 2019 Magnetic field enhanced coercivity of Fe nanoparticles embedded in antiferromagnetic MnN films J. Phys. Appl. Phys 53 035003

[139]. Jing Y, He S-H and Wang J-P 2012 Composition-and phase-controlled high-magnetic-moment $Fe_{1-x}Co_x$ nanoparticles for biomedical applications IEEE Trans. Magn 49 197–200

[140]. Xu YH, Bai J and Wang J-P 2007 High-magnetic-moment multifunctional nanoparticles for nanomedicine applications J. Magn. Magn. Mater 311 131–4

[141]. Xia Y, Nelli D, Ferrando R, Yuan J and Li ZY 2021 Shape control of size-selected naked platinum nanocrystals Nat. Commun12 1–8 [PubMed: 33397941]

[142]. Xu Y-H and Wang J-P 2007 FeCo–Au core-shell nanocrystals Appl. Phys. Lett 91 233107

[143]. Xu Y and Wang J 2008 Direct gas-phase synthesis of heterostructured nanoparticles through phase separation and surface segregation Adv. Mater 20 994–9

[144]. Llamosa D, Ruano M, Martinez L, Mayoral A, Roman E, Garcia-Hernandez M and Huttel Y 2014 The ultimate step towards a tailored engineering of core@shell and core@shell@shell nanoparticles Nanoscale 6 13483–6 [PubMed: 25180699]

[145]. Martínez L, Mayoral A, Espiñeira M, Roman E, Palomares FJ and Huttel Y 2017 Core@shell, Au@$TiO_x$ nanoparticles by gas phase synthesis Nanoscale 9 6463–70 [PubMed: 28466930]

[146]. Soler-Morala J, Jefremovas EM, Martínez L, Mayoral Á, Sánchez EH, de Toro J A, Navarro E and Huttel Y 2020 Spontaneous formation of core@shell Co@Cr nanoparticles by gas phase synthesis Appl. Nano 1 87–101

[147]. Shinde NB, Ryu BD, Meganathan K, Francis B, Hong C-H, Chandramohan S and Eswaran SK 2020 Large-scale atomically thin monolayer 2H-$MoS_2$ field-effect transistors ACS Appl. Nano Mater 3 7371–6

[148]. Huttel Y, Martínez L, Mayoral A and Fernández I 2018 Gas-phase synthesis of nanoparticles: present status and perspectives MRS Commun. 8 947 [PubMed: 30298115]

[149]. Lu A, Salabas EL and Schüth F 2007 Magnetic nanoparticles: synthesis, protection, functionalization, and application Angew. CheM., Int. Ed 46 1222–44

[150]. Mosayebi J, Kiyasatfar M and Laurent S 2017 Synthesis, functionalization, and design of magnetic nanoparticles for theranostic applications Adv. Healthc. Mater 6 1700306

[151]. Surowiec Z, Budzyński M, Durak K and Czernel G 2017 Synthesis and characterization of iron oxide magnetic nanoparticles Nukleonika 62 73–77

[152]. Hosseinzadeh S, Behboudnia M, Jamilpanah L, Sheikhi MH, Mohajerani E, Tian K, Tiwari A, Elahi P and Mohseni SM 2019 High saturation magnetization, low coercivity and fine YIG nanoparticles prepared by modifying co-precipitation method J. Magn. Magn. Mater 476 355–60

[153]. Botcha VD, Hong Y, Huang Z, Li Z, Liu Q, Wu J, Lu Y and Liu X 2019 Growth and thermal properties of various $In_2Se_3$ nanostructures prepared by single step PVD technique J. Alloys Compd 773 698–705

[154]. Tran PA, Nguyen HT, Fox K and Tran N 2018 *In vitro* cytotoxicity of iron oxide nanoparticles: effects of chitosan and polyvinyl alcohol as stabilizing agents Mater. Res. Express 5 035051

[155]. Mirzaee S, Azad-Kalandaragh M and Azizian-Kalandaragh Y 2021 Nonzero coercivity of $Fe_3O_4$/polyvinyl alcohol nanocomposites synthesized by different polymer-assisted co-precipitation processes Polym. Bull 78 2177–89

[156]. Darwish MS 2017 Effect of carriers on heating efficiency of oleic acid-stabilized magnetite nanoparticles J. Mol. Liq 231 80–85

[157]. Montaseri H, Alipour S and Vakilinezhad MA 2017 Development, evaluation and optimization of superparamagnetite nanoparticles prepared by co-precipitation method Res. Pharm. Set 12 274

[158]. Dewi R, Husain H, Sulthonul M and Pratapa S 2020 The effect of precipitation PH on structural properties of magnetite nanoparticles AIP Conf. Proc 2256 030014

[159]. Mahdavi M, Ahmad MB, Haron MJ, Namvar F, Nadi B, Rahman MZA and Amin J 2013 Synthesis, surface modification and characterisation of biocompatible magnetic iron oxide nanoparticles for biomedical applications Molecules 18 7533–48 [PubMed: 23807578]

[160]. Saragi T, Depi BL, Butarbutar S and Permana B 2018 The impact of synthesis temperature on magnetite nanoparticles size synthesized by co-precipitation method J. Phys.: Conf. Ser 1013 012190

[161]. Alonso J, Barandiarán JM, Barquín LF and García-Arribas A 2018 Magnetic nanoparticles, synthesis, properties, and applications Magnetic Nanostructured Materials 1st edn (Amsterdam: Elsevier) pp 1–40

[162]. Wu W, He Q and Jiang C 2008 Magnetic iron oxide nanoparticles: synthesis and surface functionalization strategies Nanoscale Res. Lett 3 397–415 [PubMed: 21749733]

[163]. Hyeon T, Lee SS, Park J, Chung Y and Na HB 2001 Synthesis of highly crystalline and monodisperse maghemite nanocrystallites without a size-selection process J. Am. Chem. Soc 123 12798–801 [PubMed: 11749537]

[164]. Effenberger FB, Couto RA, Kiyohara PK, Machado G, Masunaga SH, Jardim RF and Rossi LM 2017 Economically attractive route for the preparation of high quality magnetic nanoparticles by the thermal decomposition of iron (III) acetylacetonate Nanotechnology 28 115603 [PubMed: 28192283]

[165]. Dutta B, Shetake NG, Gawali SL, Barick BK, Barick KC, Babu PD, Pandey BN, Priyadarsini KI and Hassan PA 2018 PEG mediated shape-selective synthesis of cubic $Fe_3O_4$ nanoparticles for cancer therapeutics J. Alloys Compd 737 347–55

[166]. Yoon T-J, Yu KN, Kim E, Kim JS, Kim BG, Yun S-H, Sohn B-H, Cho M-H, Lee J-K and Park SB 2006 Specific targeting, cell sorting, and bioimaging with smart magnetic silica core–shell nanomaterials Small 2 209–15 [PubMed: 17193022]

[167]. Laurent S, Forge D, Port M, Roch A, Robic C, Vander Elst L and Muller RN 2008 Magnetic iron oxide nanoparticles: synthesis, stabilization, vectorization, physicochemical characterizations, and biological applications Chem. Rev 108 2064–110 [PubMed: 18543879]

[168]. Sun J, Zhou S, Hou P, Yang Y, Weng J, Li X and Li M 2007 Synthesis and characterization of biocompatible $Fe_3O_4$ nanoparticles J. Biomed. Mater. Res. A 80 333–41 [PubMed: 17001648]

[169]. Sahoo Y, Goodarzi A, Swihart MT, Ohulchanskyy TY, Kaur N, Furlani EP and Prasad PN 2005 Aqueous ferrofluid of magnetite nanoparticles: fluorescence labeling and magnetophoretic control J. Phys. Chem. B 109 3879–85 [PubMed: 16851439]

[170]. Zhang N, Xu C, Azer A and Liu H 2019 Dispersibility and characterization of polyvinyl alcohol–coated magnetic nanoparticles in poly (glycerol sebacate) for biomedical applications J. Nanopart. Res 21 1–11 [PubMed: 32184700]

[171]. Veiseh O, Gunn JW and Zhang M 2010 Design and fabrication of magnetic nanoparticles for targeted drug delivery and imaging Adv. Drug Deliv. Rev 62 284–304 [PubMed: 19909778]

[172]. Závišová V, Koneracká M, Múčková M, Lazová J, Juríková A, Lancz G, Tomašovičová N, Timko M, Kováč J and Vávra I 2011 Magnetic fluid poly (ethylene glycol) with moderate anticancer activity J. Magn. Magn. Mater 323 1408–12

[173]. Masoudi A, Hosseini HRM, Shokrgozar MA, Ahmadi R and Oghabian MA 2012 The effect of poly (ethylene glycol) coating on colloidal stability of superparamagnetic iron oxide nanoparticles as potential MRI contrast agent Int. J. Pharm 433 129–41 [PubMed: 22579990]

[174]. Illés E, Szekeres M, Kupcsik E, Tóth IY, Farkas K, Jedlovszky-Hajdú A and Tombácz E 2014 PEGylation of surfacted magnetite core–shell nanoparticles for biomedical application Colloids Surf. Physicochem. Eng. Asp 460 429–40

[175]. Mishra B, Patel BB and Tiwari S 2010 Colloidal nanocarriers: a review on formulation technology, types and applications toward targeted drug delivery Nanomedicine 6 9–24 [PubMed: 19447208]

[176]. Pankhurst QA, Thanh NTK, Jones SK and Dobson J 2009 Progress in applications of magnetic nanoparticles in biomedicine J. Phys. D: Appl. Phys 42 224001

[177]. Tassa C, Shaw SY and Weissleder R 2011 Dextran-coated iron oxide nanoparticles: a versatile platform for targeted molecular imaging, molecular diagnostics, and therapy Acc. Chem. Res 44 842–52 [PubMed: 21661727]

[178]. Mohammed L, Gomaa HG, Ragab D and Zhu J 2017 Magnetic nanoparticles for environmental and biomedical applications: a review Particuology 30 1–14

[179]. Khmara I, Strbak O, Zavisova V, Koneracka M, Kubovcikova M, Antal I, Kavecansky V, Lucanska D, Dobrota D and Kopcansky P 2019 Chitosan-stabilized iron oxide nanoparticles for magnetic resonance imaging J. Magn. Magn. Mater 474 319–25

[180]. Zahn D, Klein K, Radon P, Berkov D, Erokhin S, Nagel E, Eichhorn M, Wiekhorst F and Dutz S 2020 Investigation of magnetically driven passage of magnetic nanoparticles through eye tissues for magnetic drug targeting Nanotechnology 31 495101 [PubMed: 32946423]

[181]. Sirivat A and Paradee N 2019 Facile synthesis of gelatin-coated $Fe_3O_4$ nanoparticle: effect of PH in single-step co-precipitation for cancer drug loading Mater. Des 181 107942

[182]. Bychkova AV, Sorokina ON, Rosenfeld MA and Kovarski AL 2012 Multifunctional biocompatible coatings on magnetic nanoparticles Russ. Chem. Rev 81 1026

[183]. de Mendonça ESDT, de Faria ACB, Dias SCL, Aragón FF, Mantilla JC, Coaquira JA and Dias JA 2019 Effects of silica coating on the magnetic properties of magnetite nanoparticles Surf. Interfaces 14 34–43

[184]. Lu Y, Yin Y, Mayers BT and Xia Y 2002 Modifying the surface properties of superparamagnetic iron oxide nanoparticles through a sol–gel approach Nano Lett. 2 183–6

[185]. Yue Q, Zhang Y, Wang C, Wang X, Sun Z, Hou X-F, Zhao D and Deng Y 2015 Magnetic yolk–shell mesoporous silica microspheres with supported Au nanoparticles as recyclable high-performance nanocatalysts J. Mater. Chem. A 3 4586–94

[186]. Santra S, Tapec R, Theodoropoulou N, Dobson J, Hebard A and Tan W 2001 Synthesis and characterization of silica-coated iron oxide nanoparticles in microemulsion: the effect of nonionic surfactants Langmuir 17 2900–6

[187]. Pham X-H, Hahm E, Kim H-M, Son BS, Jo A, An J, Tran Thi TA, Nguyen DQ and Jun B-H 2020 Silica-coated magnetic iron oxide nanoparticles grafted onto graphene oxide for protein isolation Nanomaterials 10 117

[188]. Silva SM, Tavallaie R, Sandiford L, Tilley RD and Gooding JJ 2016 Gold coated magnetic nanoparticles: from preparation to surface modification for analytical and biomedical applications Chem. Commun 52 7528–40

[189]. Wang L, Wang L, Luo J, Fan Q, Suzuki M, Suzuki IS, Engelhard MH, Lin Y, Kim N and Wang JQ 2005 Monodispersed core–shell $Fe_3O_4$@Au nanoparticles J. Phys. Chem. B 109 21593–601 [PubMed: 16853803]

[190]. Cho S-J, Jarrett BR, Louie AY and Kauzlarich SM 2006 Gold-coated iron nanoparticles: a novel magnetic resonance agent for T1 and T2 weighted imaging Nanotechnology 17 640

[191]. Seo WS, Lee JH, Sun X, Suzuki Y, Mann D, Liu Z, Terashima M, Yang PC, McConnell MV and Nishimura DG 2006 FeCo/graphitic-shell nanocrystals as advanced magnetic-resonance-imaging and near-infrared agents Nat. Mater 5 971 [PubMed: 17115025]

[192]. Nikitenko SI, Koltypin Y, Palchik O, Felner I, Xu XN and Gedanken A 2001 Synthesis of highly magnetic, air-stable iron–iron carbide nanocrystalline particles by using power ultrasound Angew. Chem 113 4579–81

[193]. Geng J, Jefferson DA and Johnson BF 2004 Direct conversion of iron stearate into magnetic Fe and $Fe_3C$ nanocrystals encapsulated in polyhedral graphite cages Chem. Commun 2442–3

[194]. Song G, Kenney M, Chen Y-S, Zheng X, Deng Y, Chen Z, Wang SX, Gambhir SS, Dai H and Rao J 2020 Carbon-coated FeCo nanoparticles as sensitive magnetic-particle-imaging tracers with photothermal and magnetothermal properties Nat. Biomed.Eng 4 325–34 [PubMed: 32015409]

[195]. García-Merino B, Bringas E and Ortiz I 2021 Synthesis and applications of surface-modified magnetic nanoparticles: progress and future prospects Rev. Chem. Eng (10.1515/revce-2020-0072)

[196]. Puertas S, Batalla P, Moros M, Polo E, Del Pino P, Guisán JM, Grazú V and de la Fuente JM 2011 Taking advantage of unspecific interactions to produce highly active magnetic nanoparticle–antibody conjugates ACS Nano 5 4521–8 [PubMed: 21526783]

[197]. Rashid Z, Shokri F, Abbasi A, Khoobi M and Zarnani A-H 2020 Surface modification and bioconjugation ofanti-CD4 monoclonal antibody to magnetic nanoparticles as a highly efficient affinity adsorbent for positive selection of peripheral blood T CD4+ lymphocytes Int. J. Biol. Macromol 161 729–37 [PubMed: 32497673]

[198]. Bamrungsap S, Chen T, Shukoor MI, Chen Z, Sefah K, Chen Y and Tan W 2012 Pattern recognition of cancer cells using aptamer-conjugated magnetic nanoparticles ACS Nano 6 3974–81 [PubMed: 22424140]

[199]. Zhu Y, Kekalo K, NDong C, Huang Y-Y, Shubitidze F, Griswold KE, Baker I and Zhang JX 2016 Magnetic-nanoparticle-based immunoassays-on-chip: materials synthesis, surface functionalization, and cancer cell screening Adv. Funct. Mater 26 3953–72

[200]. Epp J 2016 X-ray diffraction (XRD) techniques for materials characterization Materials Characterization Using Nondestructive Evaluation (NDE) Methods (Amsterdam: Elsevier) pp 81–124

[201]. Scopel E, Conti PP, Stroppa DG and Dalmaschio CJ 2019 Synthesis of functionalized magnetite nanoparticles using only oleic acid and iron (III) acetylacetonate SN Appl. Set 1 147

[202]. Inkson BJ 2016 Scanning electron microscopy (SEM) and transmission electron microscopy (TEM) for materials characterization Materials Characterization Using Nondestructive Evaluation (NDE) Methods (Amsterdam: Elsevier) pp 17–43

[203]. Wierzbinski KR, Szymanski T, Rozwadowska N, Rybka JD, Zimna A, Zalewski T, Nowicka-Bauer K, Malcher A, Nowaczyk M and Krupinski M 2018 Potential use of superparamagnetic iron oxide nanoparticles for *in vitro* and *in vivo* bioimaging of human myoblasts Sci. Rep 8 1–17 [PubMed: 29311619]

[204]. Boratto MH 2018 Semiconducting and Insulating Oxides Applied to Electronic Devices Doctoral thesis Universidade Estadual Paulista

[205]. Jordán D, González-Chávez D, Laura D, Hilario LL, Monteblanco E, Gutarra A and Avilés-Félix L 2018 Detection of magnetic moment in thin films with a home-made vibrating sample magnetometer J. Magn. Magn. Mater 456 56–61

[206]. Malm AV and Corbett JC 2019 Improved dynamic light scattering using an adaptive and statistically driven time resolved treatment of correlation data Sci. Rep 9 1–11 [PubMed: 30626917]

[207]. Vogel P, Lother S, Rückert MA, Kullmann WH, Jakob PM, Fidler F, Behr VC and Meets MRI 2014 MPI: a bimodal MPI-MRI tomograph IEEE Trans. Med. Imaging 33 1954–9 [PubMed: 25291350]

[208]. Schmale I, Gleich B, Rahmer J, Bontus C, Schmidt J and Borgert J 2015 MPI safety in the view of MRI safety standards IEEE Trans. Magn 51 6502604

[209]. Bulte JW, Walczak P, Gleich B, Weizenecker J, Markov DE, Aerts HC, Boeve H, Borgert J and Kuhn M 2011 MPI cell tracking: what can we learn from MRI? Proc. SPIE 7965 79650Z

[210]. Franke J, Heinen U, Lehr H, Weber A, Jaspard F, Ruhm W, Heidenreich M and Schulz V 2016 System characterization of a highly integrated preclinical hybrid MPI-MRI scanner IEEE Trans. Med. Imaging 35 1993–2004 [PubMed: 26991821]

[211]. Zhou XY, Tay ZW, Chandrasekharan P, Elaine YY, Hensley DW, Orendorff R, Jeffris KE, Mai D, Zheng B and Goodwill PW 2018 Magnetic particle imaging for radiation-free, sensitive and high-contrast vascular imaging and cell tracking Curr. Opin. Chem. Biol 45 131–8 [PubMed: 29754007]

[212]. Werner R, Weller D, Salamon J, Möddel M and Knopp T 2019 Toward employing the full potential of magnetic particle imaging: exploring visualization techniques and clinical use cases for real-time 3D vascular imaging Proc. SPIE 10953 109531V

[213]. Haegele J, Rahmer J, Gleich B, Borgert J, Wojtczyk H, Panagiotopoulos N, Buzug TM, Barkhausen J and Vogt FM 2012 Magnetic particle imaging: visualization of instruments for cardiovascular intervention Radiology 265 933–8 [PubMed: 22996744]

[214]. Yu EY, Bishop M, Zheng B, Ferguson RM, Khandhar AP, Kemp SJ, Krishnan KM, Goodwill PW and Conolly SM 2017 Magnetic particle imaging: a novel *in vivo* imaging platform for cancer detection Nano Lett. 17 1648–54 [PubMed: 28206771]

[215]. Lindemann A, Lüdtke-Buzug K, Fräderich BM, Gräfe K, Pries R and Wollenberg B 2014 Biological impact of superparamagnetic iron oxide nanoparticles for magnetic particle imaging of head and neck cancer cells Int. J. Nanomed 9 5025

[216]. Gaudet J, Mansfield J and Goodwill P 2019 Imaging cancer immunology: tracking immune cells in vivo with magnetic particle imaging J. Immunol 202

[217]. Zhu X, Li J, Peng P, Hosseini Nassab N and Smith BR 2019 Quantitative drug release monitoring in tumors of living subjects by magnetic particle imaging nanocomposite Nano Lett. 19 6725–33 [PubMed: 31498999]

[218]. Lemaster JE, Chen F, Kim T, Hariri A and Jokerst JV 2018 Development of a trimodal contrast agent for acoustic and magnetic particle imaging of stem cells ACS Appl. Nano Mater 1 1321–31 [PubMed: 33860154]

[219]. Them K, Salamon J, Szwargulski P, Sequeira S, Kaul MG, Lange C, Ittrich H and Knopp T 2016 Increasing the sensitivity for stem cell monitoring in system-function based magnetic particle imaging Phys. Med. Biol 61 3279 [PubMed: 27032447]

[220]. Zheng B, Vazin T, Goodwill PW, Conway A, Verma A, Saritas EU, Schaffer D and Conolly SM 2015 Magnetic particle imaging tracks the long-term fate of *in vivo* neural cell implants with high image contrast Sci. Rep 5 1–9

[221]. Zheng B, Marc P, Yu E, Gunel B, Lu K, Vazin T, Schaffer DV, Goodwill PW and Conolly SM 2016 Quantitative magnetic particle imaging monitors the transplantation, biodistribution, and clearance of stem cells in vivo Theranostics 6 291 [PubMed: 26909106]

[222]. Gräser M, Thieben F, Szwargulski P, Werner F, Gdaniec N, Boberg M, Griese F, Möddel M, Ludewig P and van de Ven D 2019 Human-sized magnetic particle imaging for brain applications Nat. Commun 10 1–9 [PubMed: 30602773]

[223]. Rauwerdink AM and Weaver JB 2010 Measurement of molecular binding using the brownian motion of magnetic nanoparticle probes Appl. Phys. Lett 96 033702

[224]. Khurshid H, Friedman B, Berwin B, Shi Y, Ness DB and Weaver JB 2017 Blood clot detection using magnetic nanoparticles AIP Adv. 7 056723 [PubMed: 28289550]

[225]. Khurshid H, Shi Y, Berwin BL and Weaver JB 2018 Evaluating blood clot progression using magnetic particle spectroscopy Med. Phys 45 3258–63 [PubMed: 29772078]

[226]. Zhang X, Reeves DB, Perreard IM, Kett WC, Griswold KE, Gimi B and Weaver JB 2013 Molecular sensing with magnetic nanoparticles using magnetic spectroscopy of nanoparticle brownian motion Biosens. Bioelectron 50 441–6 [PubMed: 23896525]

[227]. Wu K, Liu J, Saha R, Su D, Krishna VD, Cheeran MC-J and Wang J-P 2020 Magnetic particle spectroscopy for detection of influenza A virus subtype H1N1 ACS Appl. Mater. Interfaces 12 13686–97 [PubMed: 32150378]

[228]. Zhong J, Rösch EL, Viereck T, Schilling M and Ludwig F 2021 Toward rapid and sensitive detection of SARS-CoV-2 with functionalized magnetic nanoparticles ACS Sens. 6 976–84 [PubMed: 33496572]

[229]. Pietschmann J, Voepel N, Voß L, Rasche S, Schubert M, Kleines M, Krause H-J, Shaw TM, Spiegel H and Schroeper F 2021 Development of fast and portable frequency magnetic mixing-based serological SARS-CoV-2-specific antibody detection assay Front. Microbiol 12 841

[230]. Rettcher S, Jungk F, Kühn C, Krause H-J, Nölke G, Commandeur U, Fischer R, Schillberg S and Schröper F 2015 Simple and portable magnetic immunoassay for rapid detection and sensitive quantification of plant viruses Appl. Environ. Microbiol 81 3039–48 [PubMed: 25710366]

[231]. Hong H-B, Krause H-J, Song K-B, Choi C-J, Chung M-A, Son S and Offenhäusser A 2011 Detection of two different influenza a viruses using a nitrocellulose membrane and a magnetic biosensor J. Immunol. Methods 365 95–100 [PubMed: 21182841]

[232]. Orlov AV, Khodakova JA, Nikitin MP, Shepelyakovskaya AO, Brovko FA, Laman AG, Grishin EV and Nikitin PI 2013 Magnetic immunoassay for detection of staphylococcal toxins in complex media Anal. Chem 85 1154–63 [PubMed: 23244173]

[233]. Orlov AV, Znoyko SL, Cherkasov VR, Nikitin MP and Nikitin PI 2016 Multiplex biosensing based on highly sensitive magnetic nanolabel quantification: rapid detection of botulinum neurotoxins A, B, and E in liquids Anal. Chem 88 10419–26 [PubMed: 27709895]

[234]. Orlov AV, Burenin AG, Massarskaya NG, Betin AV, Nikitin MP and Nikitin PI 2017 Highly reproducible and sensitive detection of mycotoxins by label-free biosensors Sens. Actuators B 246 1080–4

[235]. Meyer MH, Krause H-J, Hartmann M, Miethe P, Oster J and Keusgen M 2007 Francisella tularensis detection using magnetic labels and a magnetic biosensor based on frequency mixing J. Magn. Magn. Mater 311 259–63

[236]. Pietschmann J, Spiegel H, Krause H-J, Schillberg S and Schröper F 2020 Sensitive aflatoxin B1 detection using nanoparticle-based competitive magnetic immunodetection Toxins 12 337

[237]. Achtsnicht S, Neuendorf C, Faßbender T, Nölke G, Offenhäusser A, Krause H-J and Schröper F 2019 Sensitive and rapid detection of cholera toxin subunit B using magnetic frequency mixing detection PLoS One 14 e0219356 [PubMed: 31276546]

[238]. Meyer MH, Hartmann M, Krause H-J, Blankenstein G, Mueller-Chorus B, Oster J, Miethe P and Keusgen M 2007 CRP determination based on a novel magnetic biosensor Biosens. Bioelectron 22 973–9 [PubMed: 16766177]

[239]. Wu K, Chugh VK, di Girolamo A, Liu J, Saha R, Su D, Krishna VD, Nair A, Davies W and Wang YA 2021 A portable magnetic particle spectrometer for future rapid and wash-free bioassays ACS Appl. Mater. Interfaces 13 7966–76 [PubMed: 33566573]

[240]. Wu K, Tu L, Su D and Wang J-P 2017 Magnetic dynamics of ferrofluids: mathematical models and experimental investigations J. Phys. D: Appl. Phys 50 085005

[241]. Draack S, Lucht N, Remmer H, Martens M, Fischer B, Schilling M, Ludwig F and Viereck T 2019 Multiparametric magnetic particle spectroscopy of $CoFe_2O_4$ nanoparticles in viscous media J. Phys. Chem. C 123 6787–801

[242]. Dieckhoff J, Eberbeck D, Schilling M and Ludwig F 2016 Magnetic-field dependence of Brownian and Néel relaxation times J. Appl. Phys 119 043903

[243]. Deissler RJ, Wu Y and Martens MA 2014 Dependence of Brownian and Néel relaxation times on magnetic field strength Med. Phys 41 012301 [PubMed: 24387522]

[244]. Waldron J, Kalmykov YP and Coffey W 1994 Rotational Brownian motion and dielectric relaxation of polar molecules subjected to a constant bias field: exact solution Phys. Rev. E 49 3976

[245]. Cregg P, Crothers D and Wickstead A 1994 An approximate formula for the relaxation time of a single domain ferromagnetic particle with uniaxial anisotropy and collinear field J. Appl. Phys 76 4900–2

[246]. Ludwig F, Balceris C, Jonasson C and Johansson C 2017 Analysis of AC susceptibility spectra for the characterization of magnetic nanoparticles IEEE Trans. Magn 53 6100904

[247]. Kreissl P, Holm C and Weeber R 2021 Frequency-dependent magnetic susceptibility of magnetic nanoparticles in a polymer solution: a simulation study Soft Matter 17 174–83 [PubMed: 33165470]

[248]. Bohorquez AC and Rinaldi C 2014 *In situ* evaluation of nanoparticle–protein interactions by dynamic magnetic susceptibility measurements Part. Part. Syst. Charact 31 561–70

[249]. Wawrzik T, Yoshida T, Schilling M and Ludwig F 2015 Debye-based frequency-domain magnetization model for magnetic nanoparticles in magnetic particle spectroscopy IEEE Trans. Magn 51 5300404

[250]. Topping CV and Blundell SJ 2018 AC susceptibility as a probe of low-frequency magnetic dynamics J. Phys.: Condens. Matter 31 013001 [PubMed: 30499450]

[251]. Draack S, Viereck T, Kuhlmann C, Schilling M and Ludwig F 2017 Temperature-dependent MPS measurements Int. J. Magn. Part. Imaging 3 1703018

[252]. Perreard I, Reeves D, Zhang X, Kuehlert E, Forauer E and Weaver J 2014 Temperature of the magnetic nanoparticle microenvironment: estimation from relaxation times Phys. Med. Biol 59 1109 [PubMed: 24556943]

[253]. Rauwerdink AM, Hansen EW and Weaver JB 2009 Nanoparticle temperature estimation in combined ac and dc magnetic fields Phys. Med. Biol 54 L51 [PubMed: 19741275]

[254]. Wu K, Liu J, Wang Y, Ye C, Feng Y and Wang J-P 2015 Superparamagnetic nanoparticle-based viscosity test Appl. Phys. Lett 107 053701

[255]. Wu K, Ye C, Liu J, Wang Y, Feng Y and Wang J-P 2016 *In vitro* viscosity measurement on superparamagnetic nanoparticle suspensions IEEE Trans. Magn 52 1–4

[256]. Weaver JB, Harding M, Rauwerdink AM and Hansen EW 2010 The effect of viscosity on the phase of the nanoparticle magnetization induced by a harmonic applied field Proc. SPIE 7626 762627–8

[257]. Shi Y and Weaver JB 2019 Concurrent quantification of magnetic nanoparticles temperature and relaxation time Med. Phys 46 4070–6 [PubMed: 31209904]

[258]. Bauer LM, Situ SF, Griswold MA and Samia ACS 2015 Magnetic particle imaging tracers: state-of-the-art and future directions J. Phys. Chem. Lett 6 2509–17 [PubMed: 26266727]

[259]. Fu E, Liang T, Houghtaling J, Ramachandran S, Ramsey SA, Lutz B and Yager P 2011 Enhanced sensitivity of lateral flow tests using a two-dimensional paper network format Anal. Chem 83 7941–6 [PubMed: 21936486]

[260]. Deeks JJ and Raffle AE 2020 Lateral flow tests cannot rule out SARS-CoV-2 infection BMJ 371:m4787 [PubMed: 33310701]

[261]. Montesinos I, Gruson D, Kabamba B, Dahma H, van den Wijngaert S, Reza S, Carbone V, Vandenberg O, Gulbis B and Wolff F 2020 Evaluation of two automated and three rapid lateral flow immunoassays for the detection of anti-SARS-CoV-2 antibodies J. Clin. Virol 128 104413 [PubMed: 32403010]

[262]. Schwenke KU, Spiehl D, Krauße M, Riedler L, Ruppenthal A, Villforth K, Meckel T, Biesalski M, Rupprecht D and Schwall G 2019 Analysis of free chlorine in aqueous solution at very low concentration with lateral flow tests Sci. Rep 9 1–11 [PubMed: 30626917]

[263]. Urusov AE, Zherdev AV and Dzantiev BB 2019 Towards lateral flow quantitative assays: detection approaches Biosensors 9 89

[264]. Su D, Wu K, Krishna V, Klein T, Liu J, Feng Y, Perez AM, Cheeran MC and Wang J-P 2019 Detection of influenza a virus in swine nasal swab samples with a wash-free magnetic bioassay and a handheld giant magnetoresistance sensing system Front. Microbiol 10 1077 [PubMed: 31164877]

[265]. Ravi N, Rizzi G, Chang SE, Cheung P, Utz PJ and Wang SX 2019 Quantification of CDNA on GMR biosensor array towards point-of-care gene expression analysis Biosens. Bioelectron 130 338–43 [PubMed: 30269961]

[266]. Klein T, Wang W, Yu L, Wu K, Boylan KL, Vogel RI, Skubitz AP and Wang J-P 2019 Development of a multiplexed giant magnetoresistive biosensor array prototype to quantify ovarian cancer biomarkers Biosens. Bioelectron 126 301–7 [PubMed: 30445305]

[267]. Huang C-C, Zhou X and Hall DA 2017 Giant magnetoresistive biosensors for time-domain magnetorelaxometry: a theoretical investigation and progress toward an immunoassay Sci. Rep 7 1–10 [PubMed: 28127051]

[268]. Krishna VD, Wu K, Perez AM and Wang JP 2016 Giant magnetoresistance-based biosensor for detection of influenza A virus Front. Microbiol 7 8 [PubMed: 26858697]

[269]. Wu K, Klein T, Krishna VD, Su D, Perez AM and Wang J-P 2017 Portable GMR handheld platform for the detection of influenza A virus ACS Sens. 2 1594–601 [PubMed: 29068663]

[270]. Luo H, Wang X, Huang Y, Lai K, Rasco BA and Fan Y 2018 Rapid and sensitive surface-enhanced Raman spectroscopy (SERS) method combined with gold nanoparticles for determination of paraquat in apple juice J. Sci. Food Agric 98 3892–8 [PubMed: 29364504]

[271]. Puente C, Sánchez-Domínguez M, Brosseau CL and López I 2021 Silver-chitosan and gold-chitosan substrates for surface-enhanced Raman spectroscopy (SERS): effect of nanoparticle morphology on SERS performance Mater. Chem. Phys 260 124107

[272]. Lu Z, Liu Y, Wang M, Zhang C, Li Z, Huo Y, Li Z, Xu S, Man B and Jiang S 2018 A novel natural surface-enhanced Raman spectroscopy (SERS) substrate based on graphene oxide-Ag nanoparticles-mytilus coruscus hybrid system Sens. Actuators B 261 1–10

[273]. Guo H, He L and Xing B 2017 Applications of surface-enhanced Raman spectroscopy in the analysis of nanoparticles in the environment Environ. Sci. Nano 4 2093–107

[274]. Moram SSB, Byram C, Shibu SN, Chilukamarri BM and Soma VR 2018 Ag/Au nanoparticle-loaded paper-based versatile surface-enhanced Raman spectroscopy substrates for multiple explosives detection ACS Omega 3 8190–201 [PubMed: 31458956]

[275]. Bragina VA, Orlov AV, Znoyko SL, Pushkarev AV, Novichikhin DO, Guteneva NV, Nikitin MP, Gorshkov BG and Nikitin PI 2021 Nanobiosensing based on optically selected antibodies and superparamagnetic labels for rapid and highly sensitive quantification of polyvalent hepatitis B surface antigen Anal. Methods 13 2424–33 [PubMed: 33998615]

[276]. Krishnan KM 2010 Biomedical nanomagnetics: a spin through possibilities in imaging, diagnostics, and therapy IEEE Trans. Magn 46 2523–58 [PubMed: 20930943]

[277]. Franklin TA 2003 Ferrofluid Flow Phenomena Thesis (S.M.) Massachusetts Institute of Technology

[278]. Green M, Pattrick R, Corr S, Imai H, Haigh S, Young R and Pradeep T 2012 Nanoscience: Volume 1: Nanostructures through Chemistry (London: Royal Society of Chemistry)

[279]. Debye P 1912 Zur Theorie Der Spezifischen Wärmen Ann. Phys 344 789–839

[280]. Wu K, Liu J, Su D, Saha R and Wang J-P 2019 Magnetic nanoparticle relaxation dynamics-based magnetic particle spectroscopy for rapid and wash-free molecular sensing ACS Appl. Mater. Interfaces 11 22979–86 [PubMed: 31252472]

[281]. Poller WC, Löwa N, Wiekhorst F, Taupitz M, Wagner S, Möller K, Baumann G, Stangl V, Trahms L and Ludwig A 2016 Magnetic particle spectroscopy reveals dynamic changes in the magnetic behavior of very small superparamagnetic iron oxide nanoparticles during cellular

uptake and enables determination of cell-labeling efficacy J. Biomed. Nanotechnol 12 337–46 [PubMed: 27305767]

[282]. Dinnes J, Deeks JJ, Berhane S, Taylor M, Adriano A, Davenport C, Dittrich S, Emperador D, Takwoingi Y and Cunningham J 2021 Rapid, point-of-care antigen and molecular-based tests for diagnosis of SARS-CoV-2 infection Cochrane Database Syst. Rev CD013705 [PubMed: 33760236]

[283]. Wang C, Liu M, Wang Z, Li S, Deng Y and He N 2021 Point-of-care diagnostics for infectious diseases: from methods to devices Nano Today 37 101092 [PubMed: 33584847]

[284]. Christodouleas DC, Kaur B and Chorti P 2018 From point-of-care testing to ehealth diagnostic devices (EDiagnostics) ACS Cent. Sci 4 1600–16 [PubMed: 30648144]

[285]. Kozel TR and Burnham-Marusich AR 2017 Point-of-care testing for infectious diseases: past, present, and future J. Clin. Microbiol 55 2313 [PubMed: 28539345]

[286]. Liu J, Geng Z, Fan Z, Liu J and Chen H 2019 Point-of-care testing based on smartphone: the current state-of-the-art (2017–2018) Biosens. Bioelectron 132 17–37 [PubMed: 30851493]

[287]. Chen H, Liu K, Li Z and Wang P 2019 Point of care testing for infectious diseases Clin. Chim. Acta 493 138–47 [PubMed: 30853460]

[288]. Suleman S, Shukla SK, Malhotra N, Bukkitgar SD, Shetti NP, Pilloton R, Narang J, Tan YN and Aminabhavi TM 2021 Point of care detection of COVID-19: advancement in biosensing and diagnostic methods Chem. Eng. J 414 128759 [PubMed: 33551668]

[289]. Nayak S, Blumenfeld NR, Laksanasopin T and Sia SK 2017 Point-of-care diagnostics: recent developments in a connected age Anal. Chem 89 102–23 [PubMed: 27958710]

[290]. Guteneva NV, Znoyko SL, Orlov AV, Nikitin MP and Nikitin PI 2019 Rapid lateral flow assays based on the quantification of magnetic nanoparticle labels for multiplexed immunodetection of small molecules: application to the determination of drugs of abuse Microchim. Acta 186 621

[291]. Bragina VA, Znoyko SL, Orlov AV, Pushkarev AV, Nikitin MP and Nikitin PI 2019 Analytical platform with selectable assay parameters based on three functions of magnetic nanoparticles: demonstration of highly sensitive rapid quantitation of staphylococcal enterotoxin b in food Anal. Chem 91 9852–7 [PubMed: 31298829]

[292]. Kim C-B, Lim E-G, Shin SW, Krause HJ and Hong H 2016 Magnetic immunoassay platform based on the planar frequency mixing magnetic technique Biosens. Bioelectron 83 293–9 [PubMed: 27135936]

[293]. Rabehi A, Garlan B, Achtsnicht S, Krause H-J, Offenhäusser A, Ngo K, Neveu S, Graff-Dubois S and Kokabi H 2018 Magnetic detection structure for lab-on-chip applications based on the frequency mixing technique Sensors 18 1747

[294]. Orlov AV, Bragina VA, Nikitin MP and Nikitin PI 2016 Rapid dry-reagent immunomagnetic biosensing platform based on volumetric detection of nanoparticles on 3D structures Biosens. Bioelectron 79 423–9 [PubMed: 26741530]

[295]. Wu K, Chugh VK, Krishna VD, di Girolamo A, Wang YA, Saha R, Liang S, Cheeran MC-J and Wang J-P 2021 One-step, wash-free, nanoparticle clustering-based magnetic particle spectroscopy bioassay method for detection of SARS-CoV-2 spike and nucleocapsid proteins in the liquid phase ACS Appl. Mater. Interfaces 13 44136–46 [PubMed: 34499464]

[296]. Pietschmann J, Dittmann D, Spiegel H, Krause H-J, Schröper F and Novel A 2020 Method for antibiotic detection in milk based on competitive magnetic immunodetection Foods 9 1773

[297]. Znoyko SL, Orlov AV, Pushkarev AV, Mochalova EN, Guteneva NV, Lunin AV, Nikitin MP and Nikitin PI 2018 Ultrasensitive quantitative detection of small molecules with rapid lateral-flow assay based on high-affinity bifunctional ligand and magnetic nanolabels Anal. Chim. Acta 1034 161–7 [PubMed: 30193630]

[298]. Gordon-Wylie SW, Ness DB, Shi Y, Mirza SK, Paulsen KD and Weaver JB 2020 Measuring protein biomarker concentrations using antibody tagged magnetic nanoparticles Biomed. Phys. Eng. Express 6 065025

[299]. Nikitin M, Orlov A, Znoyko S, Bragina V, Gorshkov B, Ksenevich T, Cherkasov V and Nikitin P 2018 Multiplex biosensing with highly sensitive magnetic nanoparticle quantification method J. Magn. Magn. Mater 459 260–4

[300]. Nikitin MP, Orlov A, Sokolov I, Minakov A, Nikitin P, Ding J, Bader S, Rozhkova E and Novosad V 2018 Ultrasensitive detection enabled by nonlinear magnetization of nanomagnetic labels Nanoscale 10 11642–50 [PubMed: 29896612]

[301]. Wintzheimer S, Müssig S, Wenderoth S, Prieschl J, Granath T, Fidler F, Haddad D and Mandel K 2019 Hollow superparamagnetic nanoparticle-based microballoons for mechanical force monitoring by magnetic particle spectroscopy ACS Appl. Nano Mater 2 6757–62

[302]. Müssig S, Granath T, Schembri T, Fidler F, Haddad D, Hiller K-H, Wintzheimer S and Mandel K 2019 Anisotropic magnetic supraparticles with a magnetic particle spectroscopy fingerprint as indicators for cold-chain breach ACS Appl. Nano Mater 2 4698–702

[303]. Gordon-Wylie SW, Grüttner C, Teller H and Weaver JB 2020 Using magnetic nanoparticles and protein–protein interactions to measure PH at the nanoscale IEEE Sens. Lett 4 4500303

[304]. van de Walle A, Fromain A, Sangnier AP, Curcio A, Lenglet L, Motte L, Lalatonne Y and Wilhelm C 2020 Real-time *in situ* magnetic measurement of the intracellular biodegradation of iron oxide nanoparticles in a stem cell-spheroid tissue model Nano Res. 13 467–76

[305]. Weaver JB, Ness DB, Fields J, Jyoti D, Gordon-Wylie SW, Berwin BL, Mirza S and Fiering SN 2020 Identifying *in vivo* inflammation using magnetic nanoparticle spectra Phys. Med. Biol 65 125003 [PubMed: 32311682]

[306]. Meyer MH, Stehr M, Bhuju S, Krause H-J, Hartmann M, Miethe P, Singh M and Keusgen M 2007 Magnetic biosensor for the detection of yersinia pestis J. Microbiol. Methods 68 218–24 [PubMed: 17011649]

[307]. Gloag L, Mehdipour M, Chen D, Tilley RD and Gooding JJ 2019 Advances in the application of magnetic nanoparticles for sensing Adv. Mater 31 1904385

[308]. Yue-Jian C, Juan T, Fei X, Jia-Bi Z, Ning G, Yi-Hua Z, Ye D and Liang G 2010 Synthesis, self-assembly, and characterization of PEG-coated iron oxide nanoparticles as potential MRI contrast agent Drug Dev. Ind. Pharm 36 1235–44 [PubMed: 20818962]

[309]. Biehl P, von der Luhe M, Dutz S and Schacher FH 2018 Synthesis, characterization, and applications of magnetic nanoparticles featuring polyzwitterionic coatings Polymers 10 28

[310]. Thorat ND, Khot VM, Salunkhe AB, Ningthoujam RS and Pawar SH 2013 Functionalization of $La_{0.7}Sr_{0.3}MnO_3$ nanoparticles with polymer: studies on enhanced hyperthermia and biocompatibility properties for biomedical applications Colloids Surf. B 104 40–47

[311]. Villanueva A, de la Presa P, Alonso JM, Rueda T, Martinez A, Crespo P, Morales MP, Gonzalez-Fernandez MA, Valdes J and Rivero G 2010 Hyperthermia hela cell treatment with silica-coated manganese oxide nanoparticles J. Phys. Chem. C 114 1976–81

[312]. Zhong J, Janssen K-J, Draack S, Viereck T, Schilling M and Ludwig F 2021 Dependence of biomolecule detection on magnetic nanoparticle concentration J. Magn. Magn. Mater 517 167408

[313]. Tsai M-Z, Hsiung C-T, Chen Y, Huang C-S, Hsu H-Y and Hsieh P-Y 2018 Real-time CRP detection from whole blood using micropost-embedded microfluidic chip incorporated with label-free biosensor Analyst 143 503–10 [PubMed: 29292430]

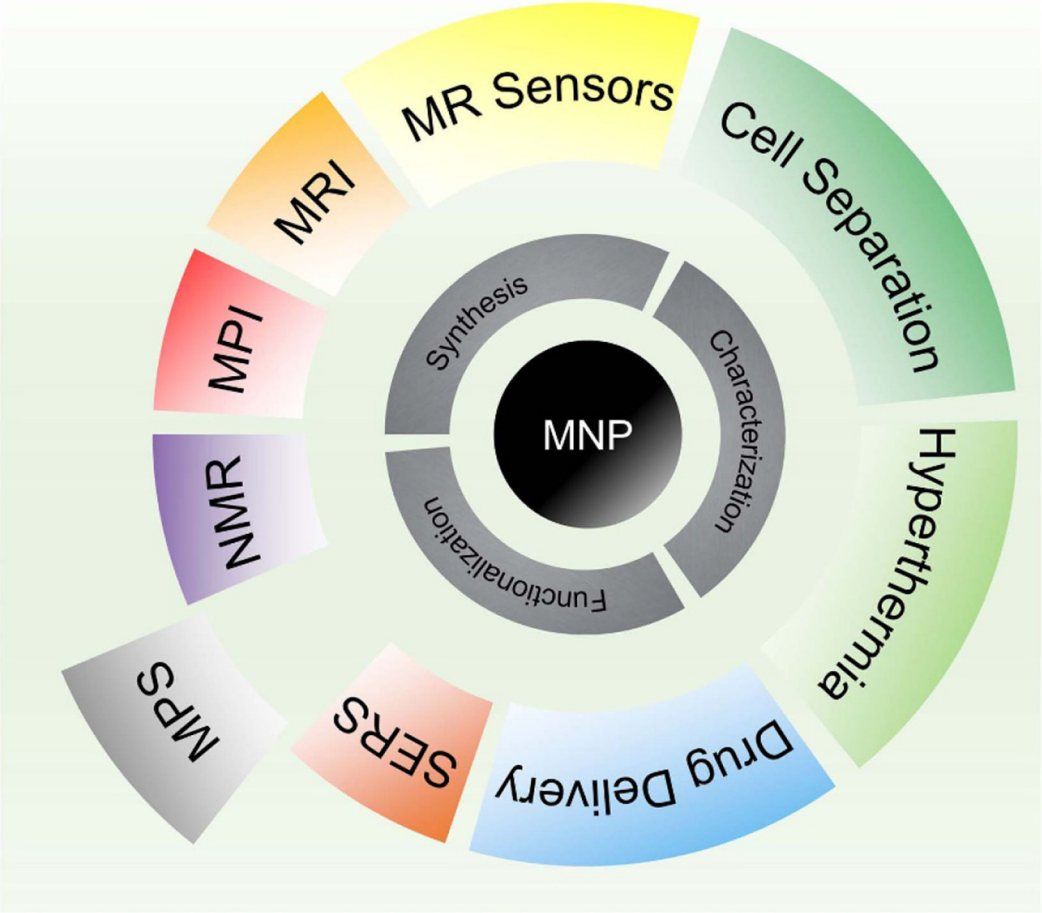


**Figure 1.**
The MNP synthesis, functionalization, and characterization lay the foundation of MNP-based biomedical applications.

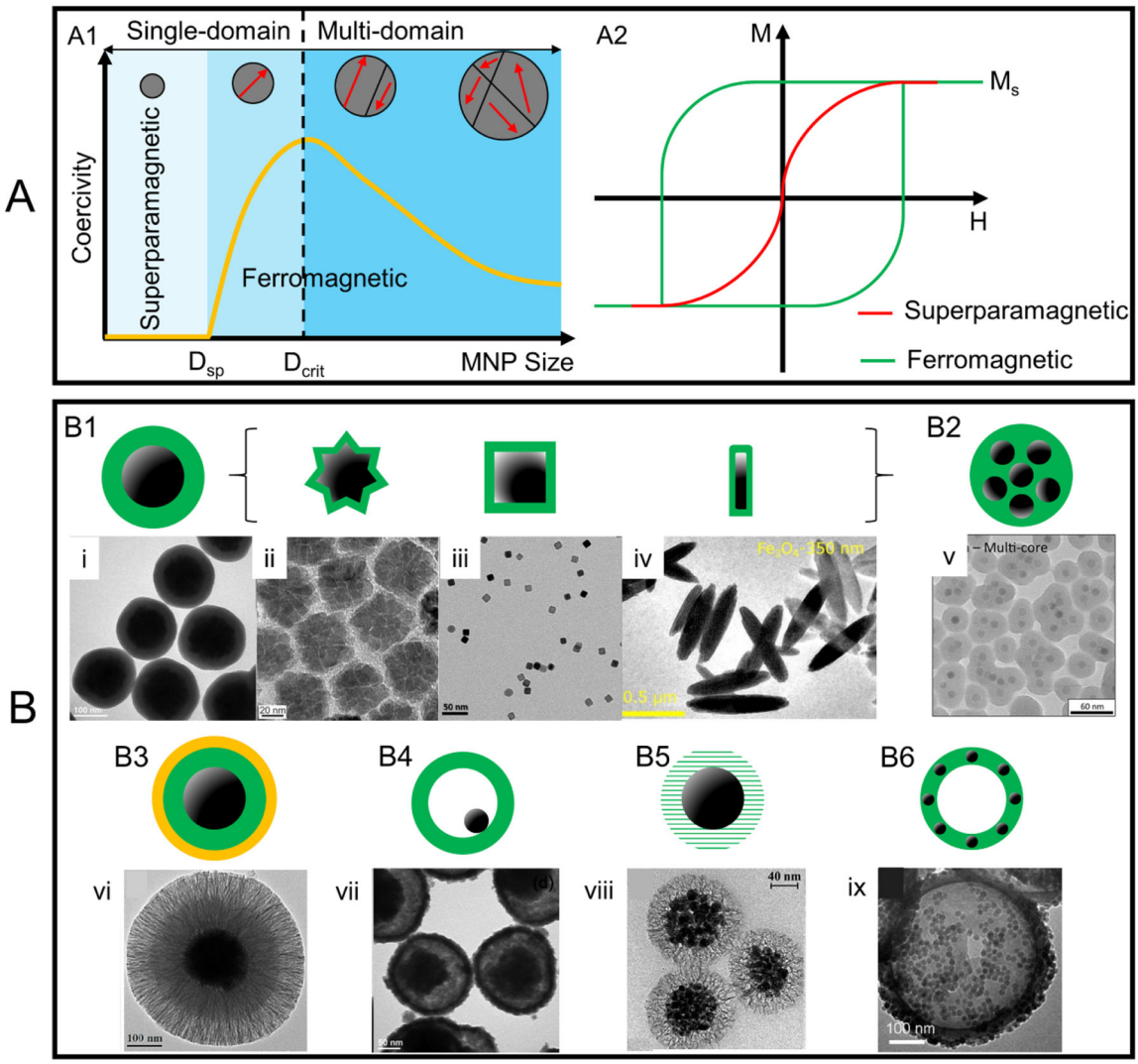


**Figure 2.**

(A) Superparamagnetic and ferromagnetic materials. (A1) Size dependence of the coercivity of magnetic materials. Larger crystallites with multi-domain states lower the coercivity. Small crystallites with a single-domain state show higher coercivity. When the size is below the superparamagnetic limit, it constantly flips the direction of magnetization to become superparamagnetic. (A2) *M–H* curves of superparamagnetic and ferromagnetic materials. (B) Schematic views and TEM images of MNPs with different structure designs. The core@shell structure including (B1) single-core and (B2) multi-core designs. (B3) Core@multi-shell structure. (B4) Hollow core@shell structure. (B5) Core@porous-shell structure. (B6) Hollow shell structure. (A1) is reproduced from [17]. © IOP Publishing Ltd. All rights reserved. (i) and (vii) are reprinted with permission from [94]. Copyright (2016) American Chemical Society. (ii) is reprinted with permission from [95]. Copyright (2018) American Chemical Society. (iii) is reproduced from [39]. CC BY 4.0. (iv) is reproduced from [96]. CC BY 4.0. (v) is reproduced from [97] with permission from the Royal Society of Chemistry. (vi) is reprinted with permission from [68]. Copyright (2015) American

Chemical Society. (viii) is reproduced from [98]. CC BY 3.0. (ix) is reproduced from [70] with permission from the Royal Society of Chemistry.

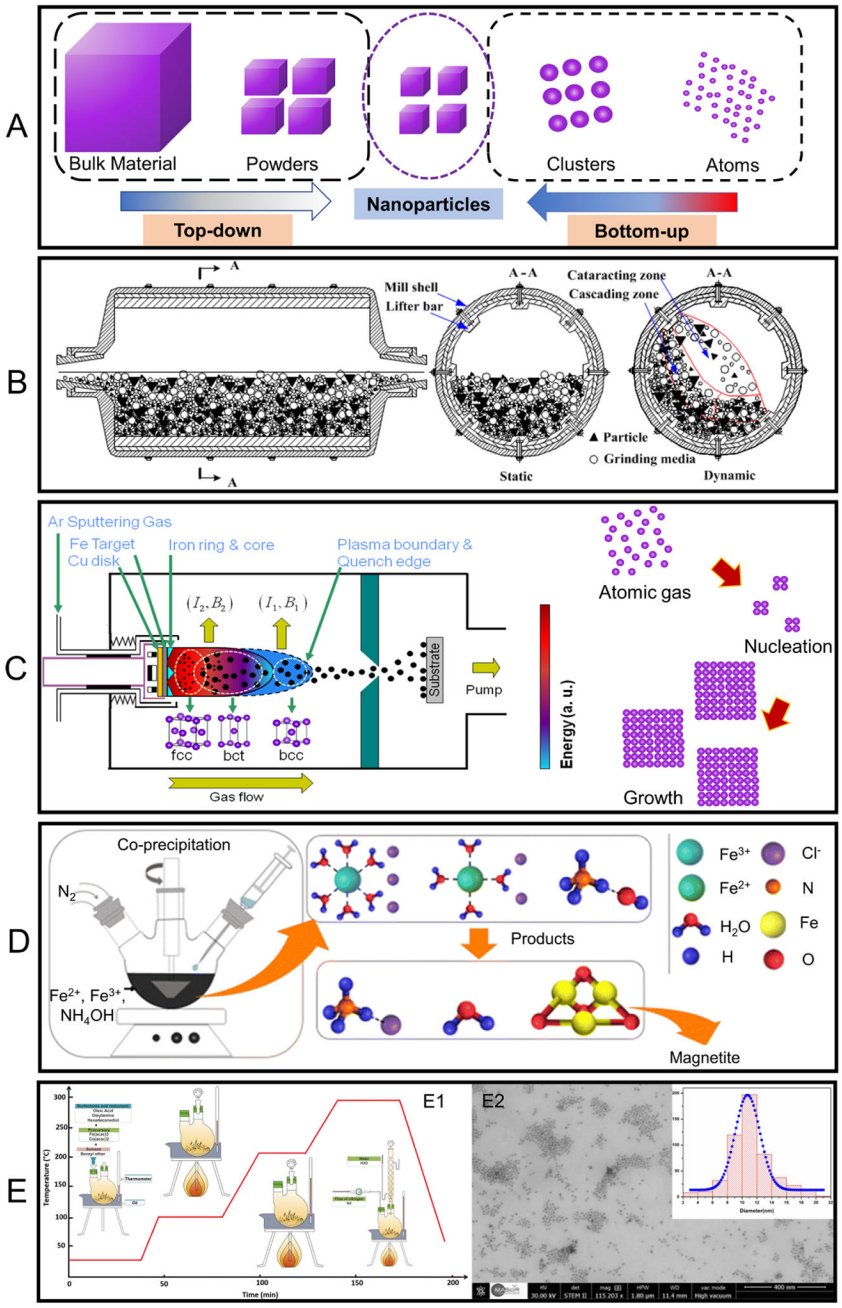


**Figure 3.**

(A) Schematic drawing of the top-down and bottom-up approaches for synthesizing MNPs. In the top-down approach, bulk materials break down in to powders and then nanoparticles. For the bottom-up approach, atoms nucleate to form small clusters and then nanoparticles. (B) Schematic drawing of a ball milling machine and the working mechanism of synthesizing nanoparticles by using a ball milling method. During the milling process, shear bands and dislocation structures are induced into bulk materials to form cell grain structures. Nanoparticles will peel off from bulk materials with the accumulation of dislocations and cell grain structures. (C) GPC system with a sputtering source for

synthesis of nanoparticles. Atoms are kicked out of the target to form atomic gas. The collisions between these atoms and sputtering gas atoms (argon) cool down the atoms to start nucleation and grow into nanoparticles. By properly control the distribution of the plasma region in the GPC system different phase and shape of nanoparticles can be synthesized. (D) The co-precipitation method. (E) The thermal decomposition method. (E1) A schematic drawing of thermal decomposition method. (E2) A SEM image shows that $CoFe_2O_4$ MNPs prepared by this method have a narrow size distribution. (B) is reproduced from [135]. CC BY 4.0. (C) is reprinted figure with permission from [40], Copyright (2018) by the American Physical Society. (D) is reproduced from [136]. CC BY 4.0. (E) is reproduced from [137], with permission from Springer Nature.

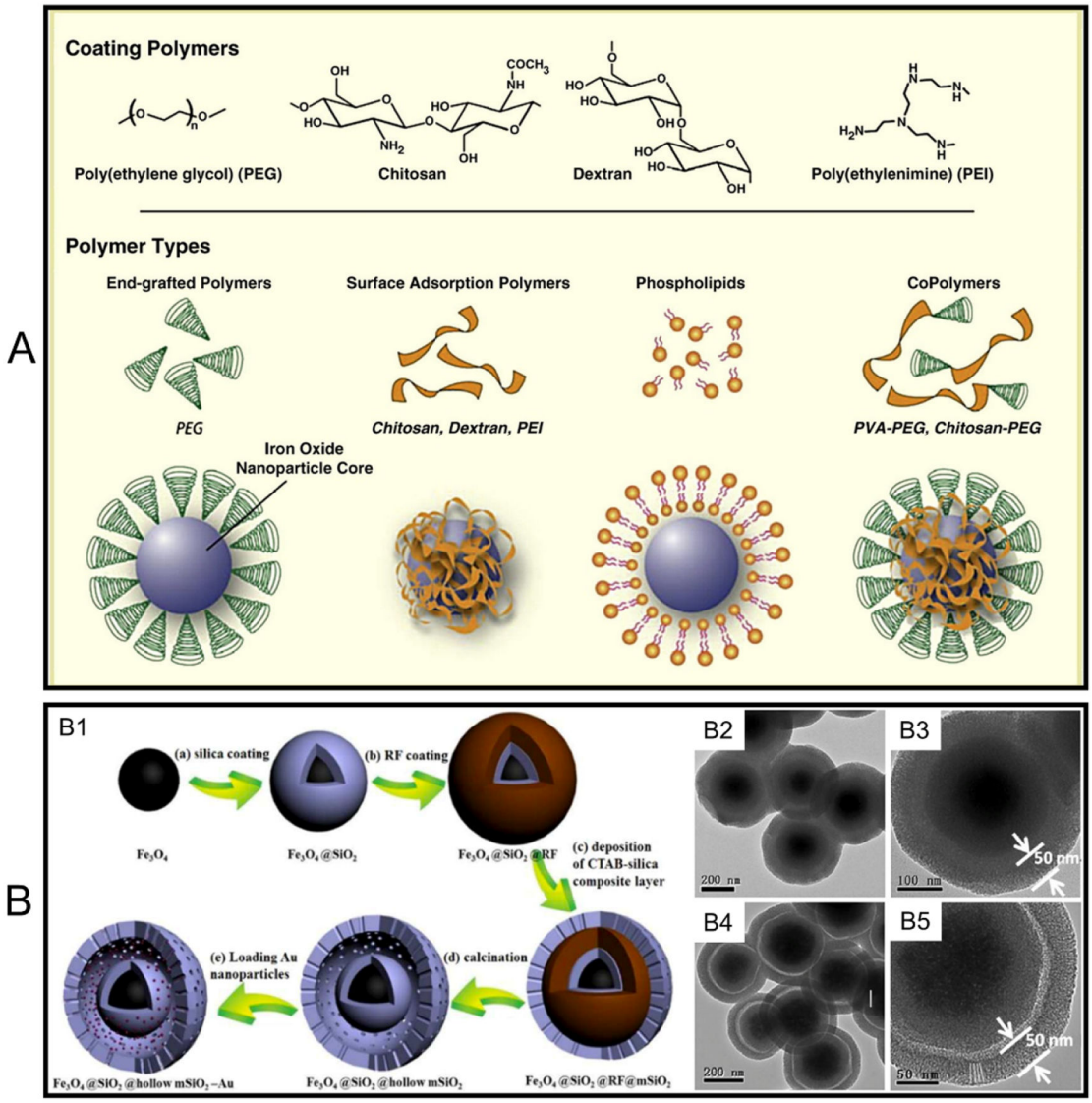


**Figure 4.**

Schematic illustration of different structures of organic (A) and inorganic coating (B). (B1) The synthetic procedure for the multifunctional yolk-shell magnetic mesoporous silica microspheres with gold nanoparticles embedded in the voids. TEM images of the multi-shelled $Fe_3O_4$@$SiO_2$@RF@CTAB/$SiO_2$ microspheres with an outer shell of ~50 nm thick CTAB/silica composite (B2), (B3) and the yolk-shell $Fe_3O_4$@$SiO_2$@hollow m$SiO_2$ microspheres (B4), (B5) with different magnifications obtained after calcination treatment. (A) is reprinted from [171], Copyright © 2009 Elsevier B.V. All rights reserved. (B) is reproduced from [185] with permission from the Royal Society of Chemistry.

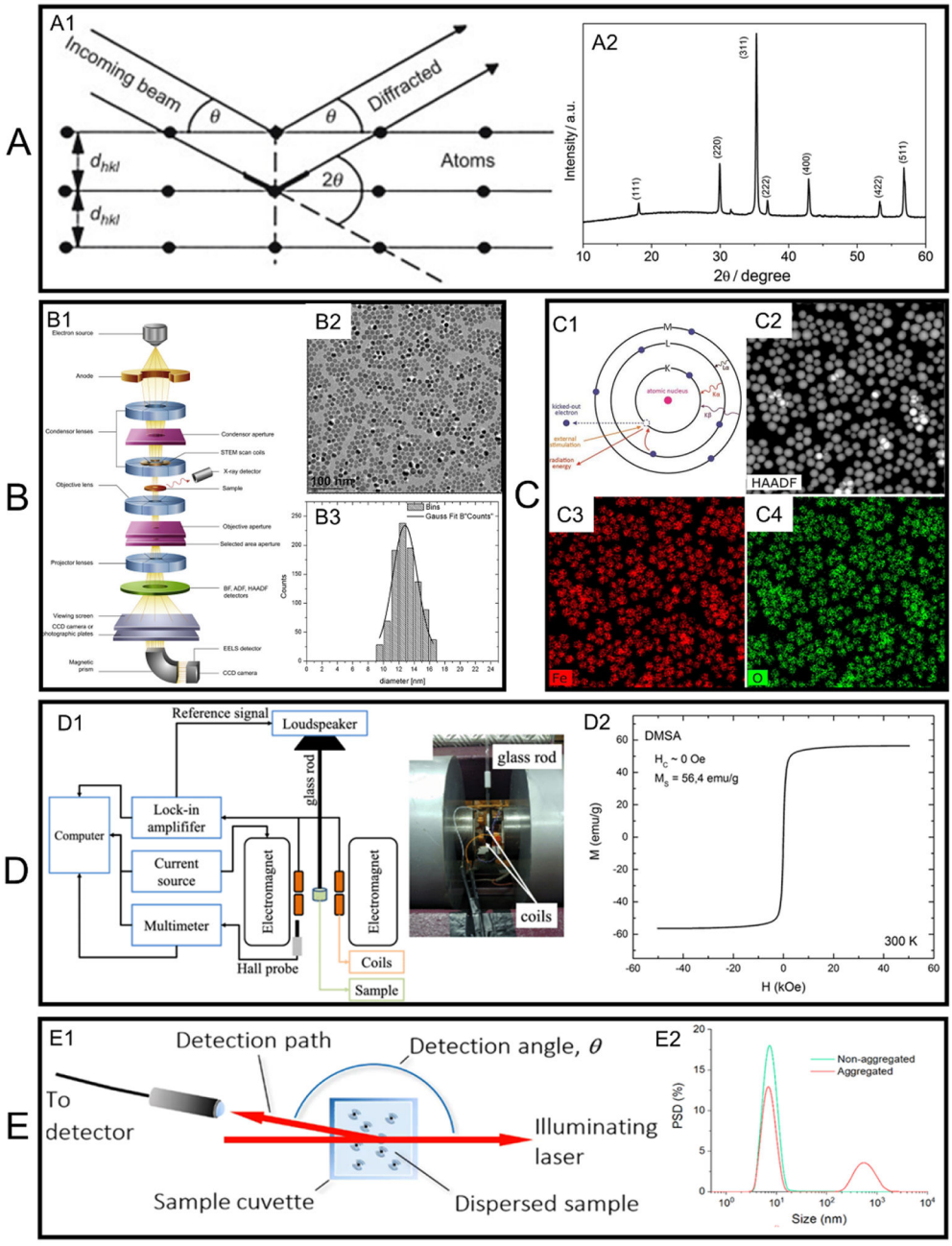


**Figure 5.**

Characterization techniques of MNPs. (A) XRD patterns for characterizing the phases information. Figure (A1) is schematic drawing of the working mechanism of XRD. The reflections of x-rays from different crystal planes form the diffraction patterns. Figure (A2) shows an example of the x-ray diffraction pattern of magnetite MNPs. Different diffraction peaks indicate different crystal planes to identify the phase information. (B) TEM for characterizing morphology of MNPs and their size and size distributions. Figure (B1) shows the working principle of a typical TEM system. Figure (B2) is a TEM image of magnetite MNPs whose size distribution is shown in (B3). (C) EDS for measuring the compositions of MNPs. Figure (C1) indicates that the EDS signal is determined by the difference of

electron energy level of the outer shell and inner shell. Different energy levels can be used to identify the elements. Figures (C2)–(C4) are a TEM image of magnetite MNPs with elemental mapping of Fe and O. (D) VSM for collecting magnetic parameters such as the saturation magnetization, remanence, coercivity, etc. Figure (D1) shows the components of a VSM and an image of a photograph of VSM system. Figure (D2) illustrates a *M*–*H* curve of magnetite MNPs measured by VSM. (E) DLS for characterizing the size distribution of MNPs dispersed in a solution. Figure (E1) shows the working principle and sizes of MNPs are determined by the detection angle of the laser beam. Figure (E2) indicates the size distribution of MNPs. (A1) is reprinted from [200], Copyright © 2016 Elsevier Ltd. All rights reserved. (A2), (C2)–(C4) are reproduced from [201], with permission from Springer Nature. (B1) is reprinted from [202], Copyright © 2016 Elsevier Ltd. All rights reserved. (B2), (B3), (D2) are reproduced from [203]. CC BY 4.0. (C1) is reproduced from [204]. CC BY-SA 3.0. (D1) is reprinted from [205], © 2018 Elsevier B.V. All rights reserved. (E) is reproduced from [206]. CC BY 4.0.

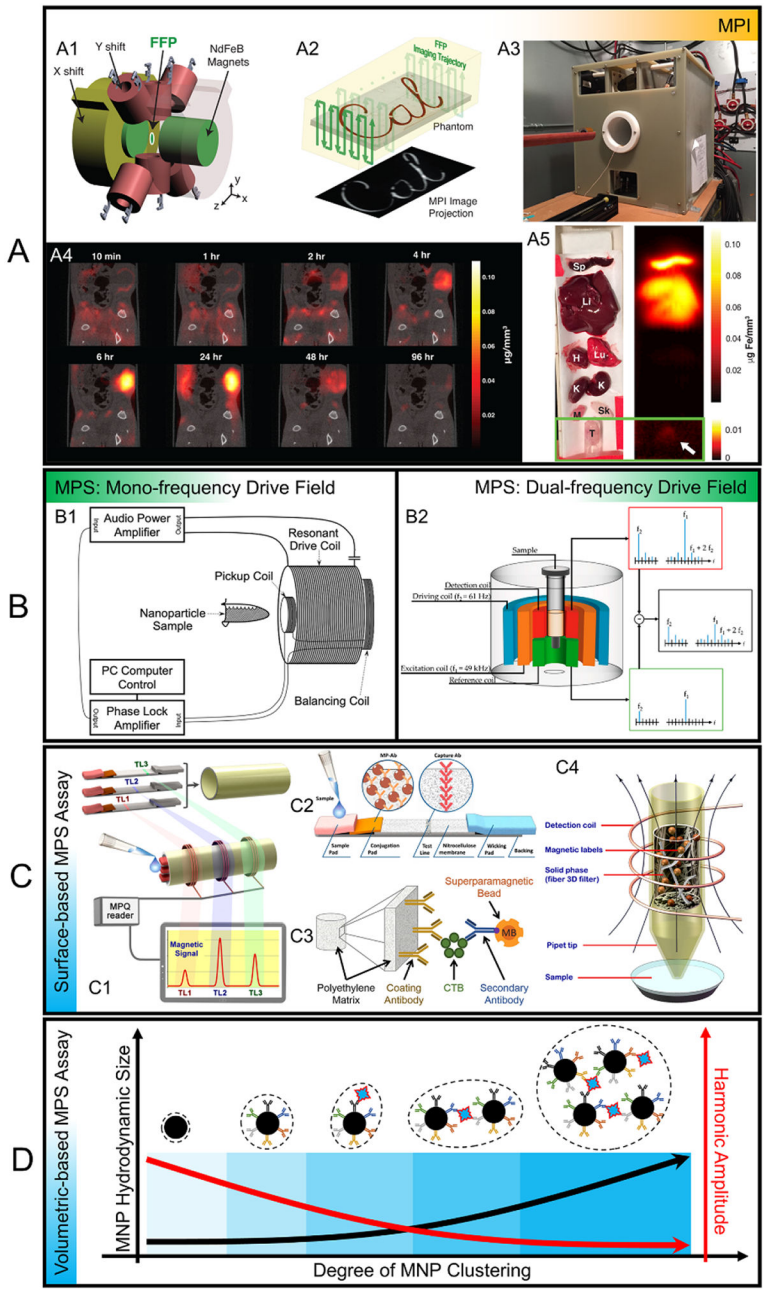


**Figure 6.**

(A) MPI technique. (A1) Schematic view of MPI platform with a magnetic field gradient created by NdFeB permanent magnets (green), the FFP is shifted in *X* and *Y* directions with electromagnets (yellow and red, respectively). (A2) The FFP follows the specified trajectory through the sample in the field of view and a 3D MPI image is acquired. A maximum intensity projection of the 3D MPI image is shown. (A3) Photograph of a custom-built FFP MPI scanner. (A4) *In vivo* MPI scan of MNP tracer biodistribution through time in rats. The MPI images with a field of view of 4 × 4 × 5.8 cm and acquisition time of 5 min were captured for these rats. The exquisite contrast of MPI allows clear visualization of the dynamics: initial rim enhancement, followed by accumulation, and then clearance. (A5) *Ex*

*vivo* MPI scan (right) and corresponding photograph (left) 2 d post MNP tracer injection. (B) Schematic views of two variations of MPS platforms. (B1) MPS with mono-frequency drive field modality. (B2) MPS with dual-frequency drive field modality. (C) Surface-based MPS bioassay scheme. Figures (C1) and (C2) show one type of surface-based MPS bioassay using test strips as reaction and binding surface. (C1) Several test strips combined in a miniature cartridge (top), the cartridge with a sample deposited onto its front end is inserted into the portable MPS reader (middle); and simultaneous readout of magnetic signals from all participating test strips (bottom). (C2) One test strip design based on sandwich-LF assay with antibody conjugated MNPs as labels. Figures (C3) and (C4) show another type of surface-based MPS bioassay using 3D fiber filters as reaction and binding surface. (C3) Schematic representation of the magnetic sandwich immune-filtration assay. (C4) Schematic view of one 3D solid phase fiber filter located inside a pipette tip. (D) Volumetric-based MPS bioassay scheme. The MNP's hydrodynamic size increases as it surface functionalized with antibodies, bounds to target analyte, and forms larger nanoparticle cluster due to inter-link with other MNPs. As a result, its dynamic magnetic responses in the form of harmonic amplitudes decrease. (A) is reprinted with permission from [214]. Copyright (2017) American Chemical Society. (B1) is reproduced with permission from [26]. (B2) is reproduced from [236]. CC BY 4.0. (C1) and (C2) are reprinted with permission from [233]. Copyright (2016) American Chemical Society. (C3) is reproduced from [237]. CC BY 4.0. (C4) is reprinted with permission from [232]. Copyright (2013) American Chemical Society. (D) is reprinted with permission from [227]. Copyright (2020) American Chemical Society.

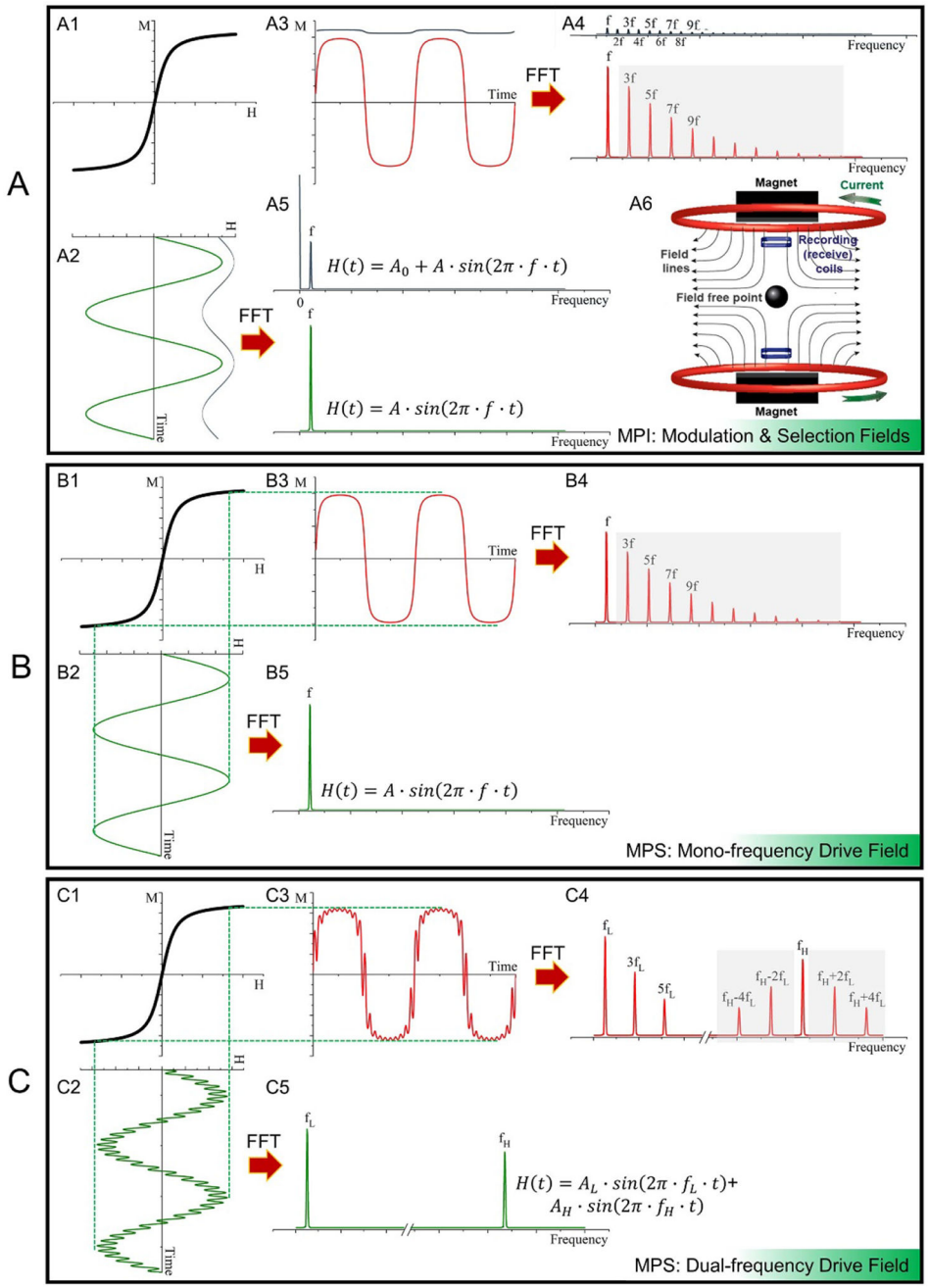


**Figure 7.**

(A) MPI technique with modulation and selection fields. (B), (C) Two types of MPS platforms classified by the magnetic drive fields. Figures (B) and (C) are the mono- and dual-frequency drive field designs, respectively. Figure (A6) is a schematic view of MPI scanner with the FFP in the center. Figures (A2)–(A5) show the magnetic fields and magnetic responses of MNP tracers in and out of FFP. (X1) are the static magnetic responses of MNPs (i.e. *MH* curves of superparamagnetic nanoparticles). (X2) are the time domain magnetic drive fields, and (X5) are their corresponding frequency domain spectra, respectively. (X3) are the dynamic magnetic responses of MNPs upon the application

of different magnetic drive fields, and (X4) are their corresponding frequency domain spectra, respectively. X = A, B, and C. (A6) is reprinted with permission from [258]. Copyright (2015) American Chemical Society. (B) and (C) are reproduced from [27]. © IOP Publishing Ltd. All rights reserved.

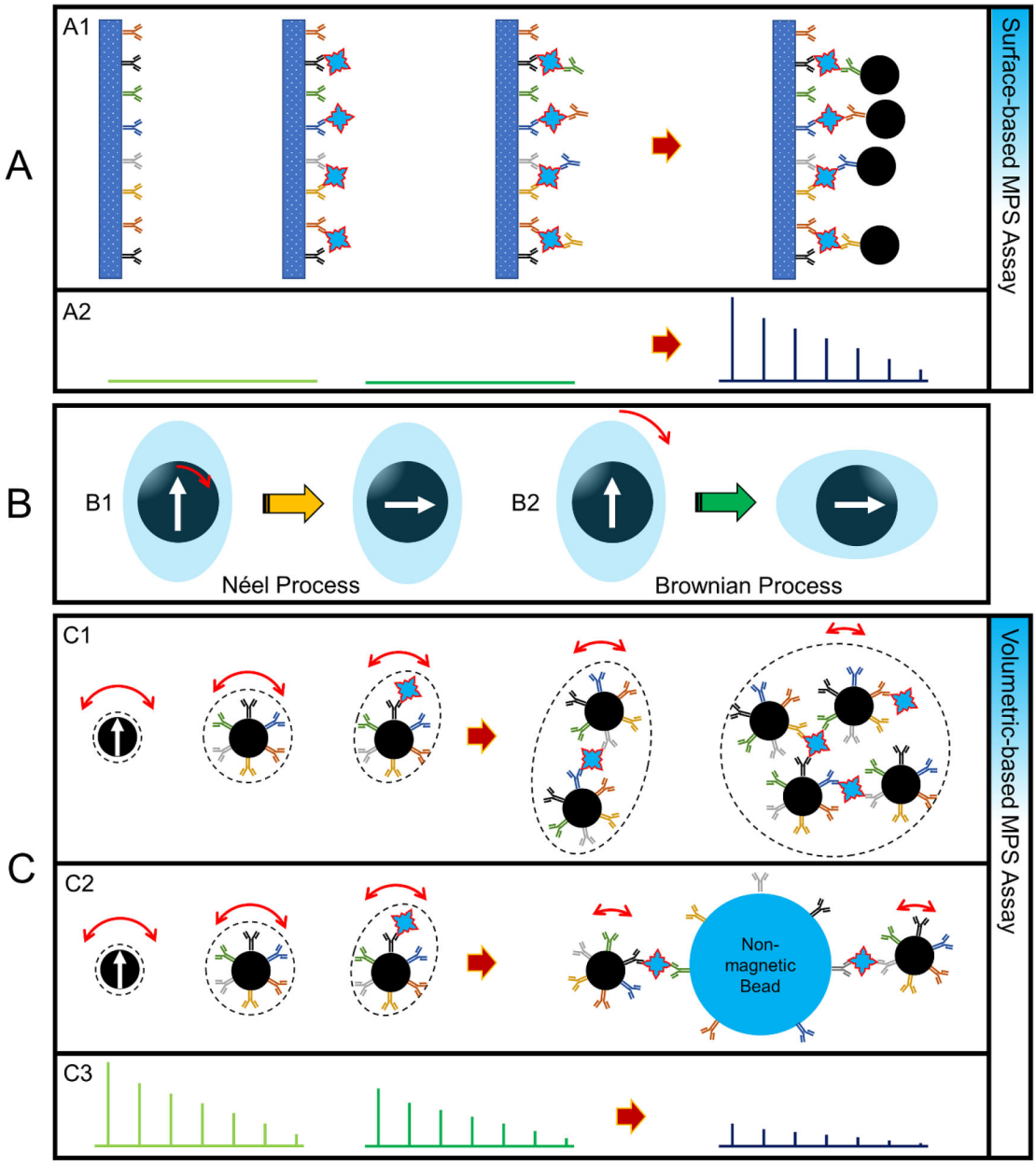


**Figure 8.**

Two types of MPS bioassay methods classified by magnetization relaxation mode. Figures (A) and (C) are schematic views of surface- and volumetric-based MPS assay methods, respectively. (A1) In a surface-based MPS bioassay method, a non-magnetic substrate functionalized with capture antibodies is applied as the reaction surface to specifically capture target analytes from biofluid sample, then one layer of detection antibody is anchored accordingly, followed by the last layer of MNPs. In this scenario, MNPs are fixed to the reaction surface and the number of MNPs left on the surface is proportional to the number of target analytes captured. Upon the application of drive fields, the fixed MNPs realign their magnetic moments through a Néel relaxation process (B1). Correspondingly, the MPS spectrum in (A2) changes in different stages of the MPS bioassay. Figure (C1)

shows a volumetric-based MPS bioassay method, MNPs are dispersed in a homogeneous liquid, which adds an additional degree of rotational freedom to their dynamic magnetic responses upon drive fields, i.e. Brownian relaxation (B2). As MNP is surface functionalized with antibodies, bound with target analytes, interlinks and forms clusters, this rotational freedom reduces, and dynamic magnetic responses become weaker. Figure (C2) is another example of volumetric-based MPS bioassay method introducing non-magnetic beads as reaction surface to further reduce the rotational freedom of MNPs. Correspondingly, the MPS spectrum in (C3) becomes weaker and weaker as Brownian relaxation is hindered by the binding and clustering events. (B) Dynamic magnetic relaxations. Figures (B1) and (B2) are the Néel and Brownian relaxation processes where Néel relaxation is the rotation of magnetic moment insides a stational MNP while, on the other hand, Brownian relaxation is the physical rotation of MNP along with its magnetic moment, following the direction of drive field. (B) is reprinted with permission from [280]. Copyright (2019) American Chemical Society.

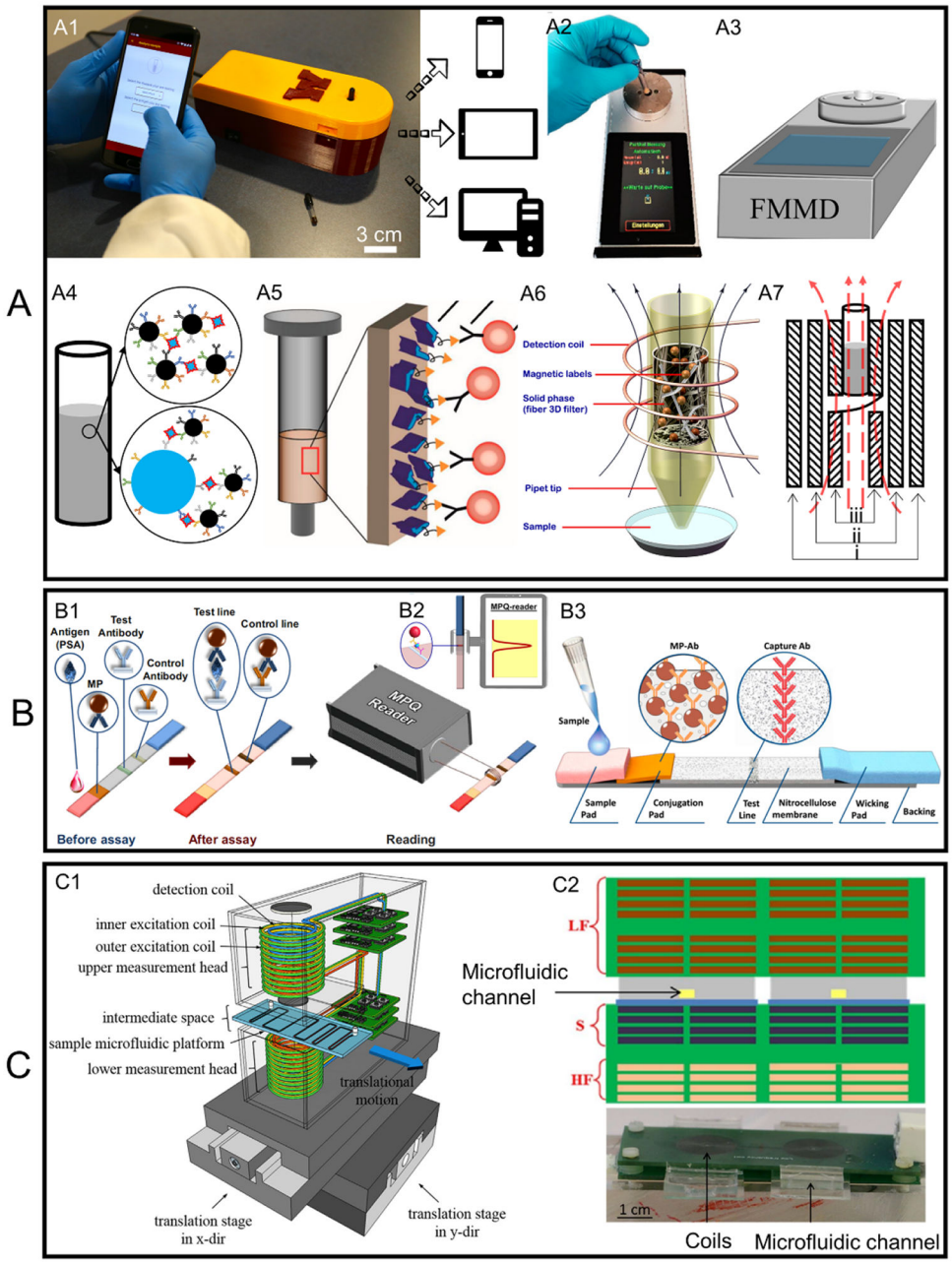


**Figure 9.**

Figures (A) and (B) are different MPS portable devices reported. (A1) MagiCoil portable device with a smartphone application reported by Wu *et al* (A2) and (A3) FMMD portable device reported by Pietschmann *et al* (A4) volumtric-based MPS bioassay in a vial. (A5), (A6) Surface-based MPS bioassay in a vial. (A7) A dual-frequency MPS signal reader consists of (i) one set of coils generating low-frequency drive field, (ii) one set of coils generating high-frequency drive field, and (iii) one pair of differentially wounded pick-up coils sensing magnetic signals from MNPs. (B) MPQ portable device reported by Orlov *et al*, Guteneva *et al*, and Bragina *et al*. Figure (C) shows different MPS portable devices combined with microfluidic channels. Figure (C1) is a p-FMMD portable device reported

by Kim *et al*. Figure (C2) is a MPS portable device with planar coils for drive fields and pick-up coils reported by Rabehi *et al*. (A1) is reprinted with permission from [239]. Copyright (2021) American Chemical Society. (A2) and (A5) are reproduced from [236]. CC BY 4.0. (A3) is reproduced from [229]. CC BY 4.0. (A6) is reprinted with permission from [232]. Copyright (2013) American Chemical Society. (B1) is reprinted from [294], Copyright © 2015 Elsevier B.V. All rights reserved. (B2) is reprinted with permission from [291]. Copyright (2019) American Chemical Society. (B3) is reprinted with permission from [233]. Copyright (2016) American Chemical Society. (C1) is reprinted from [292], © 2016 Elsevier B.V. All rights reserved. (C2) is reproduced from [293]. CC BY 4.0.

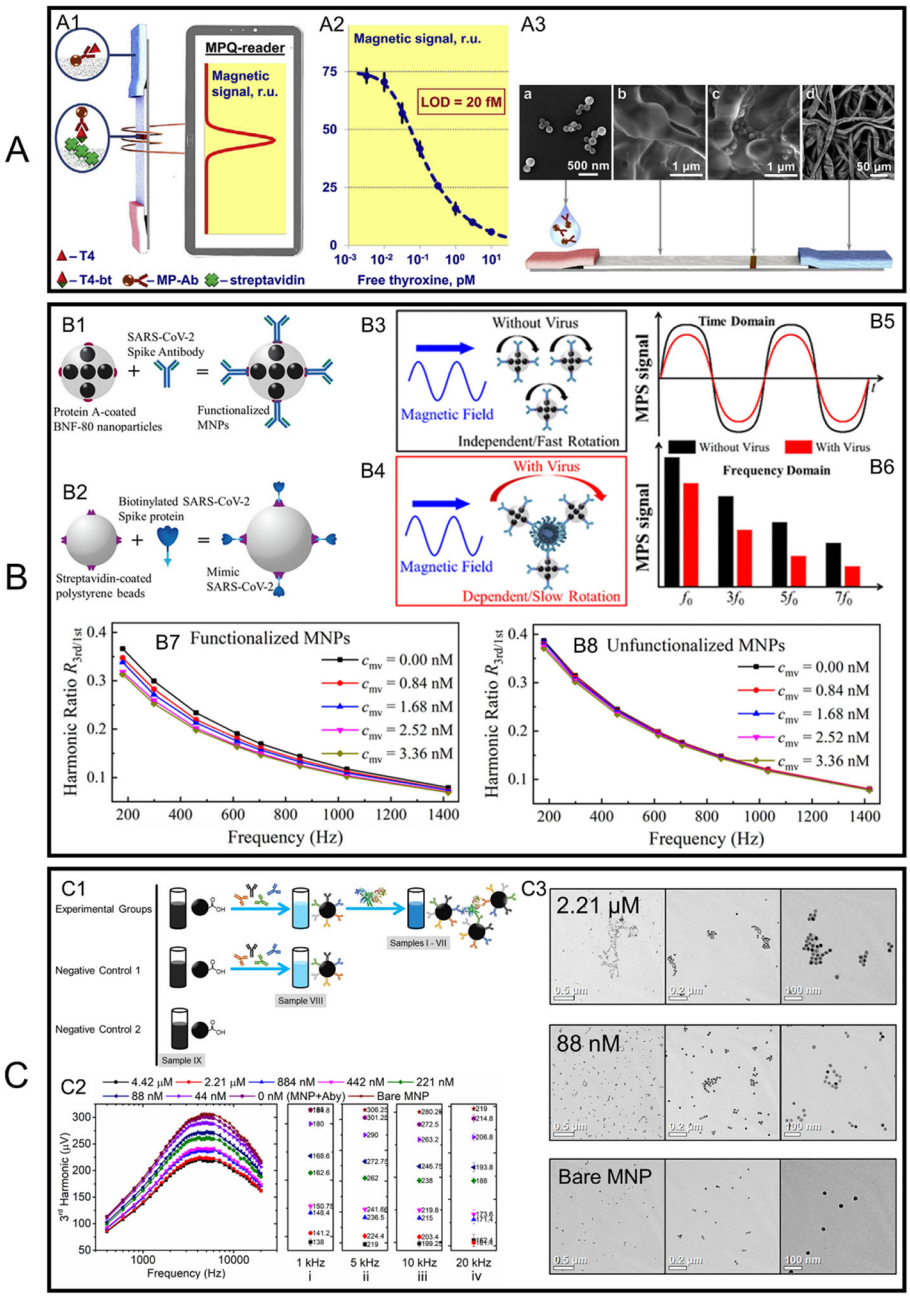


**Figure 10.**

(A) Surface-based, dual-frequency drive field MPS platform with LF strip for detection of human serum of fT4. (A1) Principle of lateral flow assay on a strip and its reading by the MPQ-reader. (A2) Dependence of magnetic signal on fT4 concentration from human serum. (A3) SEM-characterization of the lateral flow test strip assay components: MNPs conjugated with antibody to thyroxine (a) nitrocellulose membrane on the test line (c) and beyond it (b), absorbent pad (d). Volumetric-based, mono-frequency drive field MPS platform for detection of mimic SARS-CoV-2 nanoparticles. Figures (B1) and (B2) are the schematic views of functionalized MNPs and mimic SARS-CoV-2 nanoparticles. Figures (B3) and (B4) are the schematic views of rotational freedom of functionalized MNPs with

and without the presence of mimic SARS-CoV-2 nanoparticles (virus). Figures (B5) and (B6) are the corresponding time domain and frequency domain MPS signal for scenarios in (B3) and (B4), respectively. Figures (B7) and (B8) are the experimental results of measured harmonic ratio $R$ 3rd/1st vs drive field frequency of functionalized (B7) and unfunctionalized (B8) MNPs with different mimic virus concentrations. (C) Volumetric-based, dual-frequency drive field MPS platform for detection of H1N1 nucleoprotein. (C1) Experimental and negative control groups. Sample indexes I–VII are MNP-antibody complexes in the presence of different concentrations of the H1N1 nucleoprotein; sample index VIII is an MNP-antibody complex in the absence of the H1N1 nucleoprotein (denoted as '0 nM (MNP + Aby)'); sample index IX is bare MNP suspension (denoted as 'Bare MNP'). (C2) MPS measurements of the 3rd and the 5th harmonics from samples I–IX at varying magnetic drive field frequencies from 400 Hz to 20 kHz. Figures (i)–(iv) highlight the 3rd harmonic amplitudes measured at 1 kHz, 5 kHz, 10 kHz, and 20 kHz, respectively. (C3) The bright-field TEM images of MNPs highlighting the different degrees of MNP clustering in the presence of H1N1 nucleoprotein. (A) is reprinted from [297], © 2018 Elsevier B.V. All rights reserved. (B) is reprinted with permission from [228]. Copyright (2021) American Chemical Society. (C) is reprinted with permission from [227]. Copyright (2020) American Chemical Society.

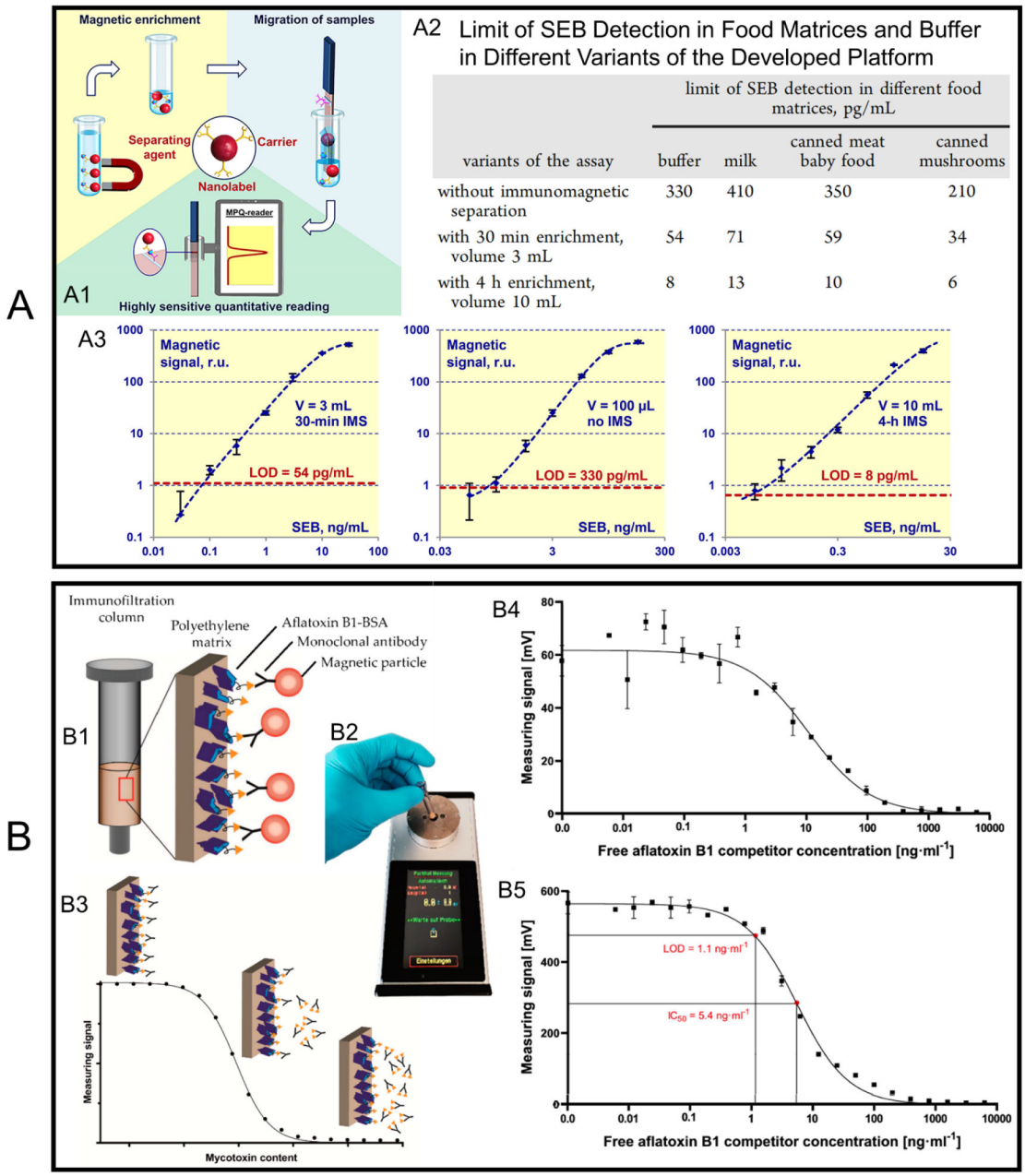


**Figure 11.**

(A) Surface-based, dual-frequency drive field MPS platform with LF strip for the detection of SEB. (A1) Steps of LF strip assay combined with MPS platform including magnetic enrichment, migration of samples, and MPS reading. (A2) LODs for SEB from different food matrices with different sample volumes and IMS time. (A3) SEB concentration vs magnetic signal from MNPs. (B) Surface-based, dual-frequency drive field MPS platform with immune-filtration columns as substrates. (B1) Schematic view of immuno-filtration column coated with aflatoxin B1-BSA, then bind with biotinylated monoclonal antibodies targeting aflatoxin B1. MNPs functionalized with streptavidin bind to antibodies and can be detected by the FMMD as shown in (B2). (B3) Schematic view of calibration curves based

on competitive bioassay method. (B4) and (B5) are the calibration curves using 700 nm and 70 nm MNP tracers, respectively. The concentration of free aflatoxin B1 is varied from 0.006 ng $ml^{-1}$ to 500 000 ng $ml^{-1}$. (A) is reprinted with permission from [291]. Copyright (2019) American Chemical Society. (B) is reproduced from [236]. CC BY 4.0.

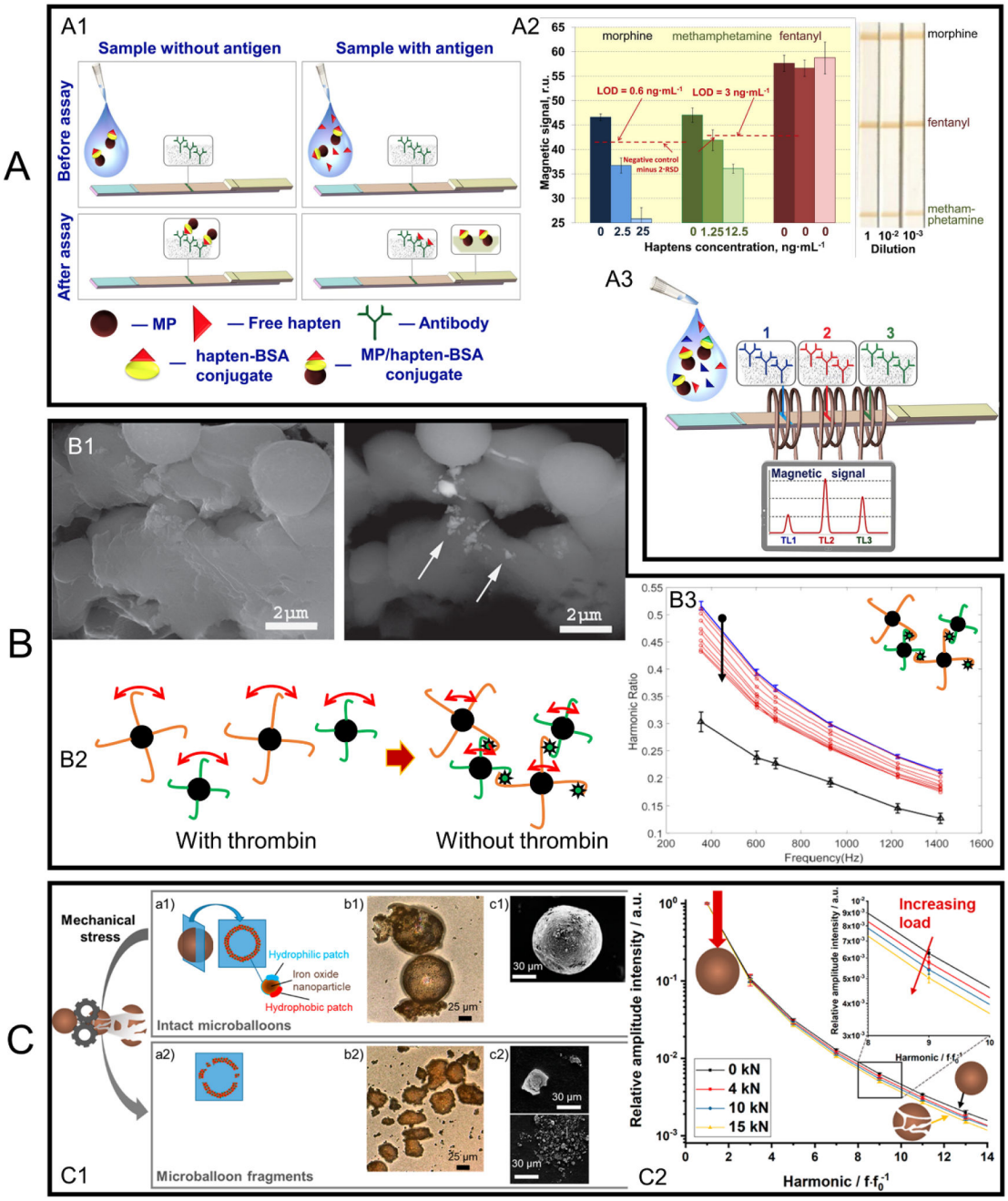


**Figure 12.**

(A) Surface-based, dual-frequency drive field MPS platform with LF strip for the detection of drugs from urine. (A1) Principle of competitive magnetic LF assay with MPS platform. MNPs functionalized with target analyte and BSA are added to 75 $\mu l$ of human urine samples containing known concentrations of a drug of abuse, incubated for 10 min at room temperature and applied onto the LF test strip. After migration of the sample along the test strip, the test strip is inserted into the MPQ reader to readout the magnetic signal. (A2) MPQ signal simultaneously measured in the MPS platform along with the photos of respective LF strips. The human urine samples contained known concentrations of morphine

and methamphetamine but no fentanyl to verify the assay specificity. (A3) Scheme of view of MPS for the multiplexed detection of morphine, fentanyl, and methamphetamine from human urine samples. (B) Volumetric-based, mono-frequency drive field MPS platform for the evaluation of blood progression. (B1) SEM image of the blood clot with MNPs in secondary electron mode (left) and in BSE mode showing MNP clusters on the blood cells, marked by arrows. (B2) Schematic view of surface functionalized MNPs forming clusters in the presence of thrombin. The rotational freedom of MNPs is blocked due to thrombin. Figure (B3) shows MPS signals of the functionalized MNPs bind to thrombin on the blood clot over time (30 min). The blue curve marks MNPs before adding clot and the red curves mark signal from MNPs with blood clot over time. The signal from blood clot in PBS is shown in black curve. (C) Hollow superparamagnetic nanoparticle-based microballoons for mechanical force monitoring by MPS. (C1) The as-prepared hollow spherical balloon-like shape is observed as depicted in schematic (a1) as well as LSM (b1) and SEM (c1) images. After application of mechanical forces, the microballoons are fragmented due to their hollow structure, which is also shown in the schematic, LSM and SEM images ((a2), (b2), and (c2), respectively). (C2) Drop of the MPS signal curves of microballoons during the application of quasi-static compression increases significantly with increasing load. (A) is reproduced from [290], with permission from Springer Nature. (B1) is reproduced with permission from [225]. (B3) is reproduced from [224]. CC BY 4.0. (C) is reprinted with permission from [301]. Copyright (2019) American Chemical Society.

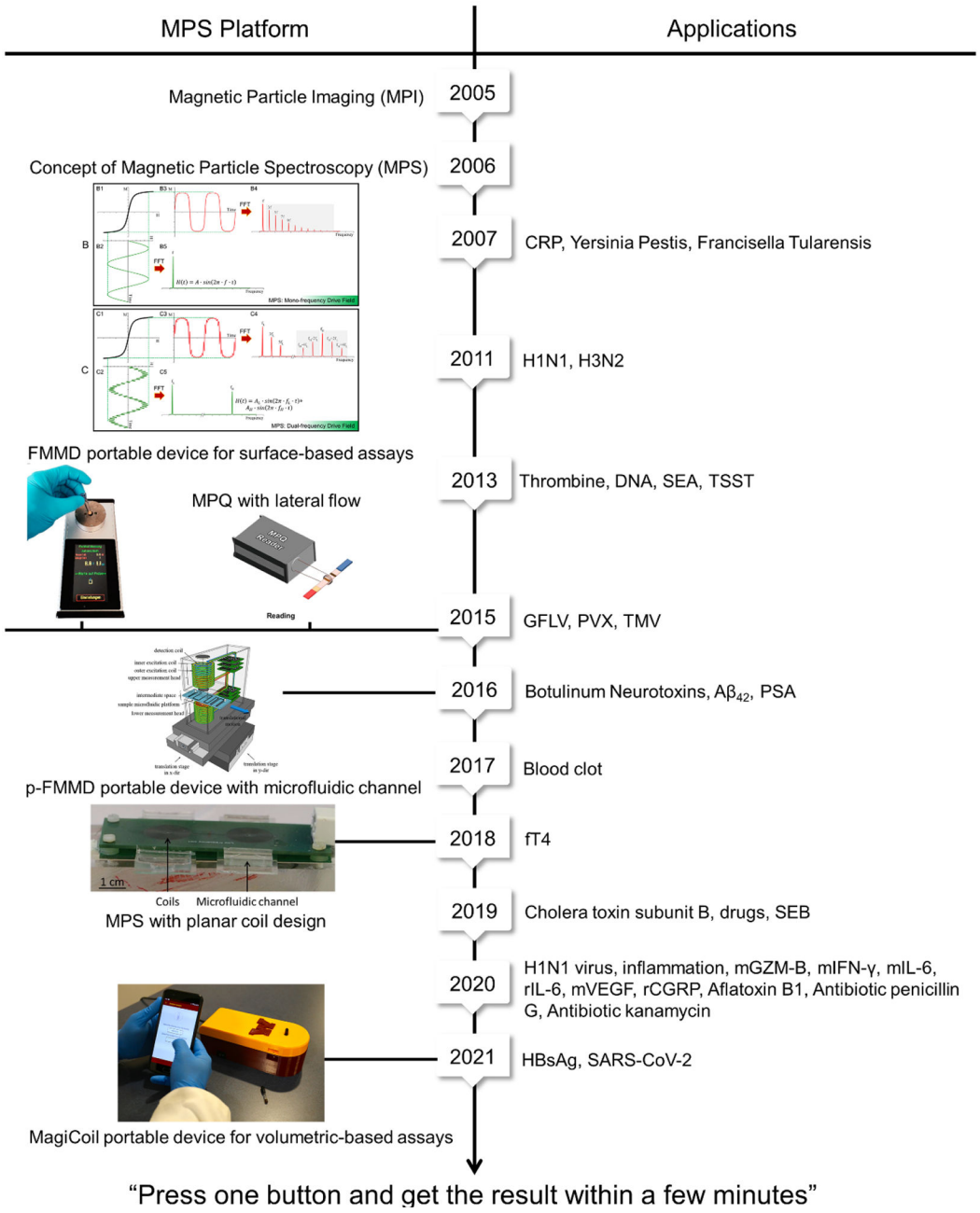


**Figure 13.**
The 15 year roadmap of MPS platform and MPS-based applications.

**Table 1.**

Some popular magnetic materials and their magnetic properties.

| Material | $\sigma_s$ (emu g$^{-1}$)[a] | $\sigma$ (emu g$^{-1}$)[b] | $K$ (erg cm$^{-3}$) | $D_{sp}$ (nm)[c] | References |
|---|---|---|---|---|---|
| $Fe_3O_4$ | 90–98 (bulk) | 50 (80 nm MNP at 1 kOe) | $-1.1 \times 10^5$ | 26 | [45-47] |
| | 60 (80 nm MNP) | 30–60 (10–300 nm MNP at 1 kOe) | | | |
| | 55–85 (10–300 nm MNP) | — | | | |
| $\gamma$ | 76–82 (bulk) | 40 (20 nm MNP at 1 kOe) | $-4.6 \times 10^4$ | 35 | [45, 48, 49] |
| | 51 (20 nm MNP) | 50 (30 nm MNP at 1 kOe) | | | |
| | 74 (30 nm MNP) | — | | | |
| FeCo | 270 (bulk) | ~60 (40 nm MNP at 1 kOe) | $10^5$ | 27 | [50-52] |
| | 200 (20 nm MNP) | 50–100 (8–20 nm MNP at 1 kOe) | | | |
| | 175 (12 nm MNP) | — | | | |
| | 125 (8 nm MNP) | | | | |
| Fe | 217 (bulk) | <40 (20 nm Fe@oxide MNP at 1 kOe) | $K_1 = 4.8 \times 10^5$ | 16 | [53, 54] |
| | 26–113 (8–20 nm Fe@oxide MNP)[d] | | $K_2 = \pm 0.5 \times 10^5$ | | |
| $Fe_5Si_3$ | 80 (20 nm MNP) | 66 (20 nm MNP at 1 kOe) | $3 \times 10^5$ | 19 | [42] |
| $\gamma'$-$Fe_4N$ | 184 (bulk)<br>117–182 (80 nm MNP) | 100 (40 nm MNP at 1 kOe) | $2.9 \times 10^5$ | 19 | [55-57] |
| $\alpha''$-$Fe_{16}N_2$ | 226–290 (bulk) | 170 (100 nm MNP at 5 kOe) | $9.6 \times 10^6$ | 5.9 | [54, 58-60] |
| $Fe^{16}CN$ | 258 (bulk) | — | $2.4 \times 10^6$ | 9.4 | [61, 62] |

[a] Specific saturation magnetization.

[b] Specific magnetization.

[c] $D_{sp}$ is the size limit below which MNPs show superparamagnetic property at 300 K.

[d] Fe MNP can easily oxide so a shell layer will be covered on its surface, which decreases its magnetization tremendously.

**Table 2.**

Advantages and disadvantages of different MNP synthesis techniques.

| Method | Advantages | Disadvantages |
|---|---|---|
| Ball milling | Easy process<br>High yield | Contaminations of MNPs<br>Large size distributions |
| Gas-phase condensation | Phase and size control<br>Contamination-free | Low yield<br>Requires high vacuum environment<br>Expensive systems |
| Co-precipitation | Simple and effective | Precise stoichiometric and size control |
| Thermal decomposition | Narrow size distribution<br>Good structural properties | Toxic organic solvents chemically bonded to surfaces of MNPs |

**Table 3.**

Summary of different MPS portable devices reported so far.

| MPS portable device | Platform | Bioassay method | Detected target analytes | References |
|---|---|---|---|---|
| MagiCoil | Dual-frequency | Volumetric-based | SARS-CoV-2 spike and nucleocapsid proteins | [295] |
| FMMD[a] | Dual-frequency | Surface-based | SARS-CoV-2-specific antibody | [229] |
| | | | Grapevine fanleaf virus (GFLV), Potato virus X (PVX), and Tobacco mosaic virus (TMV). | [230] |
| | | | Aflatoxin B1 | [236] |
| | | | Antibiotic including penicillin G and kanamycin | [296] |
| MPQ | Dual-frequency | Surface-based | Botulinum neurotoxins A, B, and E | [233] |
| | | | Hepatitis B surface antigen (HBsAg) | [275] |
| | | | Staphylococcal enterotoxin B | [291] |
| | | | Drugs including morphine, fentanyl and methamphetamine | [290] |
| | | | Prostate specific antigen (PSA) | [294] |
| | | | Free thyroxine (fT4) | [297] |
| p-FMMD[a] | Dual-frequency | Surface-based | Amyloid beta 42 ($A\beta_{42}$) | [292] |

[a]FMMD and p-FMMD are two different devices independently developed by different groups.

**Table 4.**

Summary of MPS-based bioassays classified by platforms and drive fields (year 2006–2021).

| MPS platform | Magnetic drive field | MNP | Target analyte | Matrice | Dynamic range | Detection limit | Assay time | References |
|---|---|---|---|---|---|---|---|---|
| Volumetric-based | Mono-frequency | 50 nm multi-core | Thrombin | Buffer | 4–20 nM | 4 nM | 10 s | [226] |
| | | | DNA | Buffer | 200–2000 pM | 100 pM | | |
| | | | | Serum | — | 400 pM | | |
| | | 100 nm multi-core | Blood clot | — | — | — | — | [224] |
| | | 50 nm multi-core | Blood clot | — | — | — | — | [225] |
| | | 100 nm multi-core | Inflammation and infection | — | — | — | — | [305] |
| | | 100 nm multi-core | Mouse granzyme B (mGZM-B) | Buffer | — | 10 pM | — | [298] |
| | | | Mouse interferon-gamma (mIFN-$\gamma$) | | | 40 pM | | |
| | | | Mouse interleukin-6 (mIL-6) | | | 7 pM | | |
| | | | Rat interleukin-6 (rIL-6) | | | 40 pM | | |
| | | | Mouse vascular endothelial growth factor (mVEGF) | | | 40 pM | | |
| | | | Rat calcitonin gene related peptide (rCGRP) | | | 250 pM | | |
| | | 80 nm multi-core | SARS-CoV-2 spike protein | Buffer | — | 0.084 nM for mimic SARS-CoV-2 beads | — | [228] |
| | Dual-frequency | 30 nm single-core | H1N1 nucleoprotein | Buffer | — | 44 nM | — | [227] |
| | | 30 nm single-core | SARS-CoV-2 spike protein | Buffer | — | 1.56 nM (125 fmole) | — | [295] |
| | | | SARS-CoV-2 nucleocapsid protein | | | 12.5 nM (1 pmole) | | |
| | | 70 nm multi-core | SARS-CoV-2-specific antibody | Serum | — | — | 21 min | [229] |
| Surface-based | Dual-frequency | 0.5–1 $\mu$m multi-core | C-reactive protein (CRP) | Saliva, urine and blood serum | 25 ng ml$^{-1}$ −2.5 $\mu$g ml$^{-1}$ | | 11.5 min | [238] |
| | | 0.5–1 $\mu$m multi-core | *Yersinia pestis* antigen F1 | Buffer and blood serum | 25–300 ng ml$^{-1}$ | 2.5 ng ml$^{-1}$ | — | [306] |
| | | 0.5–1 $\mu$m multi-core | *Francisella tularensis lipopolysaccharide* | Buffer and rabbit serum | $10^4$–$10^6$ cfu ml$^{-1}$ | — | — | [235] |
| | | 198 nm multi-core | Botulinum neurotoxins A, B, and E | Buffer | — | 185, 140, 350 pg ml$^{-1}$ | — | [233] |
| | | | | Milk | — | 197, 143, 254 pg ml$^{-1}$ | | |
| | | | | Apple juice | — | 307, 142, 465 pg ml$^{-1}$ | | |
| | | | | Orange juice | — | 287, 139, 410 pg ml$^{-1}$ | | |

| MPS platform | Magnetic drive field | MNP | Target analyte | Matrice | Dynamic range | Detection limit | Assay time | References |
|---|---|---|---|---|---|---|---|---|
| | | 70 nm multi-core | Antibiotic penicillin G | Milk | 1.33–35.29 ng $ml^{-1}$ | 1.33 ng $ml^{-1}$ | — | [296] |
| | | | Antibiotic kanamycin | | 1–53.41 ng $ml^{-1}$ | 1 ng $ml^{-1}$ | | |